Investigation of the Interaction of Particulate Matter with the Gas Diffusion Layer

by

AMIR PANAHI

A thesis
presented to the University of Waterloo
in fulfillment of the
thesis requirement for the degree of
Master of Applied Science
in
Mechanical and Mechatronics Engineering

Waterloo, Ontario, Canada, 2017

Author’s Declaration

I hereby declare that I am the sole author of this thesis. This is a true copy of the thesis, including any required final revisions, as accepted by my examiners.

I understand that my thesis may be made electronically available to the public.

Abstract

Rapid global industrialization has resulted in an unprecedented level of energy consumption. Transportation comprises a significant portion of the demand for energy, and special attention has recently been paid to green energy sources. Proton exchange membrane fuel cells (PEMFCs) are a promising zero-emission candidate: they use hydrogen and oxygen to produce electricity, with water as a byproduct. PEMFC is susceptible to performance degradation due to impurities in the hydrogen (anode) or oxygen (cathode) streams. While the effect of impurities in the anode side has been extensively investigated in the past, the impurities in the cathode, especially particulate matter, have not been studied extensively. Particulate matter contamination in cathode is a potential risk to optimal performance of PEMFCs in vehicular applications and the interaction is investigated numerically in this work.

The most critical component of a PEMFC that can be affected by particulate matter, is the gas diffusion layer (GDL) due to its fibrous structure. Due to the random structure of fibrous media, a systematic approach is implemented where a single-fiber model is used as the most fundamental element of the GDL. The single fiber model is used for validation of flow and particle characteristics, paving the way for increasing the number of fibers. The multi-fiber model is challenged with particles of varying size confirming the dominance of the Brownian diffusion particle capture mechanism over other mechanisms for the target particle diameter of 0.1 μm.

The operation of PEMFC requires high humidity levels in the cathode which must be accounted for in the particle capture model. The humidity in the cathode stream results in an increase in particle size, decrease in particle bounce, decrease in particle density, and decrease in air density compared to an otherwise dry cathode stream. Upon addition of the humidity model to the multi-fiber model of the GDL it is observed that of the abovementioned humidity effects, only the increase in particle size is significant. For the target particle diameter of 0.1 μm as the humidity level increases, the particles become larger, and the particle capture efficiency drops. This is due to the transition from the Brownian diffusion to the inertial impaction and interception particle capture mechanisms. Large enough particles whose capture is dominated by inertial impaction and interception, i.e. particles larger than 1.3 μm, have an opposite pattern: as the relative humidity level increases, particle capture efficiency for such particles increases.

Given the high cathode humidity requirements for operation of PEMFC, it is critical to ensure the size of the particles at the GDL are below the threshold for capture mechanism transition. By implementing a fibrous filter upstream of the GDL, as the relative humidity increases, the particle capture efficiency of the filter, which is exposed to larger particles, increases, and the particle capture efficiency of the GDL decreases, meeting the optimal performance requirement.

Acknowledgement

I would like to express my profound gratitude to my supervisor *Dr. Xianguo Li*. The door to Professor Li's office was always open whenever I ran into a trouble or had a question about my research or writing. He consistently allowed this thesis to be my own work, but steered me in the right direction whenever he thought I needed it.

I would also like to thank my colleague *Abbas Ghasemi* for his expert advice on technical obstacles along the way and for sharing his vast experience of the field with me.

Finally, I would like to thank my family and my friends *Mani Mirabzadeh*, *Utej Sohal*, and *Miriam Meurer* for providing me with unfailing support and continuous encouragement throughout my years of study and through the process of researching and writing this thesis. This accomplishment would not have been possible without them.

Amir Panahi

Table of Contents

List of Figures

List of Tables

Nomenclature

A	ratio of nitrate to sulfate in dry particle
C_c	Cunningham correction factor
C_{fil}	number of particles collecting on filter downstream of substrate
C_r	humidity model constant
C_{sub}	number of particles collecting on substrate
d_f	diameter of fiber
d_p	diameter of the particle
D	wet particle diameter
D_0	dry particle diameter
D_p	particle Diffusion Coefficient
F	drag force
F^*	non-dimensional drag force
F_D	drag force on particle
F_{ext}	external force
F_g	gravity force
F_w	horizontal force acti ng on the surface of the circle
g	gravity vector
h	vertical distance between two adjacent fibers
k	Boltzmann Coefficient
Kn	Knudsen number based on radius of fiber
l	horizontal distance between two adjacent fibers
m_p	mass of particle
P	pressure
Pe	Peclet number

Pe_m modified Peclet number

r, θ cylindrical coordinates with origin at the center of the cylinder

r^* dimensionless distance from the center of the fiber

R interception parameter

R_a gas constant for dry air with value of $287\ J\ kg^{-1}K^{-1}$

Re Reynolds number calculated based on fiber diameter

RH relative humidity

R_w gas constant for water vapor with value of $462 J\ kg^{-1}K^{-1}$

Stk Stokes number

Stk_m modified Stokes number

T temperature

u, U velocity in the x direction

u_{slip} slip velocity

W humidity ratio

Y dimensionless hydrodynamic factor

Z thickness of filter

Greek Letters

α fiber volume fraction of the filter

β ratio of non-water-soluble to water-soluble species in dry particle

ΔP actual pressure drop

Δt time step taken by solver

ζ a normally distributed random number with a mean of zero and a unit standard deviation

η_D efficiency due to diffusion

η_{it} efficiency due to interception

λ mean free path of the gas with value of $66\ nm$ for air at $1\ atm$ and room temperature

μ dynamic viscosity

ρ density of the surrounding fluid

ρ_p density of particle

σ tangential momentum accommodation coefficient

τ_i tangential momentum of incoming molecules

τ_p particle velocity response time

τ_r tangential momentum of the reflected molecules

τ_w tangential momentum of the remitted molecules ($\tau_w = 0$ for stationary surfaces)

Ψ dimensionless stream function

1 Introduction

Consumption of energy has become a daily necessity in the modern world where it is essential for the functioning of the contemporary society, the prosperity of the nations and most importantly the survival of human civilization. After the industrial revolution, the constant improvements to the quality of life, the industrialization of developing countries and the increase of world population have steadily increased the need for reliable energy sources [1]. At present, the majority of the energy is supplied by combustion of fossil fuels including coal, oil and gas, as shown in Figure 1. With the steady increase in energy consumption in the recent years, the share of fossil sources has remained dominant. This is partially due to the improved technology and infrastructure for fossil sources [2]. Heat engines such as steam turbine have become an essential part of the energy supply network being increasingly relied upon since the industrial revolution. The adverse effects of excessive use of fossil fuel energy sources have been long known to result in increased health risks to all life forms and irreversible change in the environment. Besides, the limited fossil fuel reserve has transformed international relations and national security of each country. Fuel cell technology has the potential to meet the needs of our modern civilization and reduce the undesirable effects of energy consumption in the modern world.

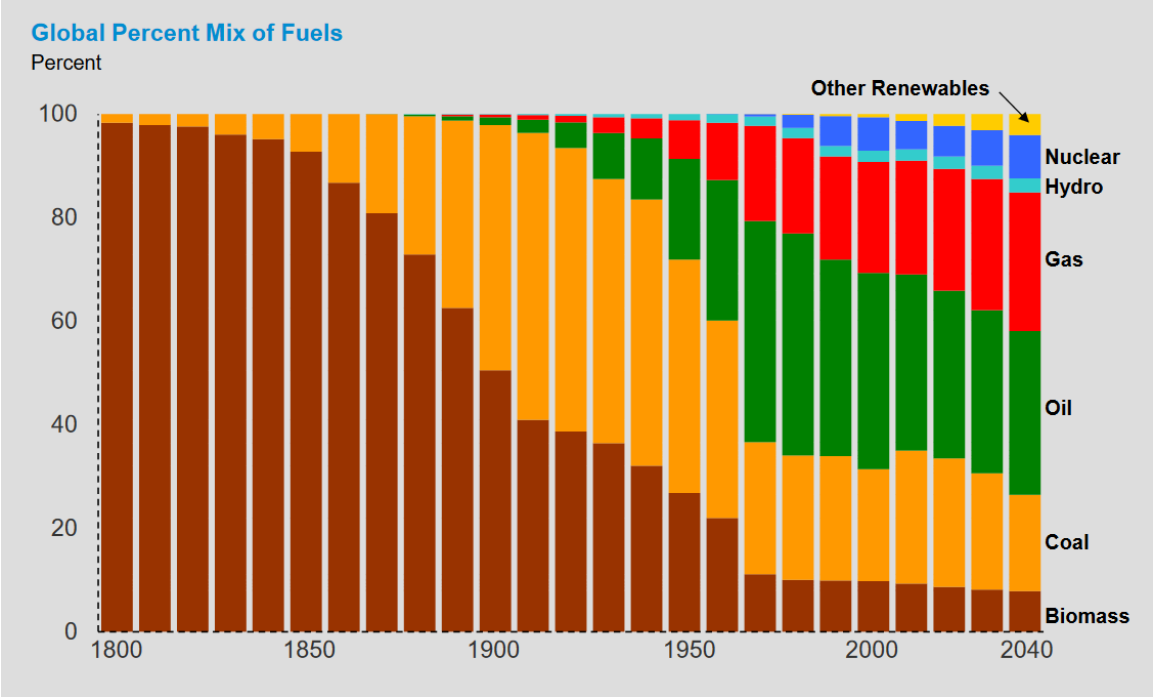

Figure 1 : Global percent mix of fuels [3]

The exclusive reliance on the combustion of fossil fuels has resulted in unprecedented air pollution due to the emission of gases such as SO_x, NO_x, CO, and particulates which particularly impose health risks to residents of urban areas [4]. While the effect is immediately visible in urban areas, the resulting air pollution has an even larger effect on the climate of the earth. The climate change due to air pollution has reached alarming levels, hence driving research and development to cleaner

and more efficient energy sources. The need for a more efficient and cleaner energy source is two pronged. Firstly, such an energy source will lessen the pollutant emissions and improve the climate conditions. Secondly, given the limited supply of fossil fuels, a more efficient and cleaner energy source will ensure uninterrupted supply of energy for daily needs of the modern world as well as sustainable development. Fuel cells are efficient zero-emission devices that meet the requirements for energy security, economic growth, and environmental sustainability [5].

A variety of alternative energy sources are proposed for power generation such as hydroelectric power, wind, wave, solar, bioenergy, geothermal energy and so on. Renewable energy sources can be used relatively easily however, these sources are subject to seasonal and irregular fluctuations and are especially impractical for direct utilization for transportation applications, which account for a significant portion of the pollutant emissions. The intermittent nature of power generation from renewable energy sources requires storage of energy. Batteries, flywheels, and super-capacitors are examples of energy storage methods that have not been shown to be an ideal option, especially for transportation applications. It is proposed to use hydrogen as a promising energy carrier and to adopt fuel cells as the clean and efficient means of power generation from hydrogen for mobile applications. The paramount advantage of this option lies in the fact that when combined with oxygen for generating power, hydrogen forms water making it an emission-free energy source. Major automotive manufacturers have development and testing projects on fuel cell vehicles. Fuel cells are also being used in buses, airplanes, scooters and golf carts [6].

Research and development in the field of fuel cells has overcome many obstacles and has reached a point very close to large scale commercialization. Nonetheless, there is still substantial room for innovation in the fast growing fuel cell field. Most of the work done in the field is related to development and characterization of fuel cells in a lab environment with limited attention to practical applications such as transportation, where the effect of real-life environmental conditions on the performance of fuel cells becomes important. There is also a huge opportunity for researchers to engage in the research of issues that arise from the interfacing of fuel cells with current vehicular subsystems. Research in such fields fosters innovation and paves the way for large scale commercialization of fuel cells.

Fuel cells is a multi-disciplinary field which has been studied by researchers with backgrounds from mechanical, chemical, and electrical engineering. The extensive research on different components of fuel cells has helped pave the way for implementation of fuel cells in many commercial applications. Large scale applications such as applications in transportation require specific testing of fuel cells based on the operating conditions of the vehicle. Such tests would assess the performance of the fuel cells in real-life conditions that are not necessarily taken into account in the development of laboratory grade fuel cells. With fuel cells being far closer to commercial large scale implementation than ever before, investment in researching the effect of real-life conditions on the performance of the fuel cell and consequent development of solutions to address any deficiencies, is essential for keeping a leading position in this field.

The consequences of pollutant emission from combustion of fossil fuels have become evident recently in highly populated metropolitan areas such as Beijing and New Delhi. Severe air pollution in these areas has occluded economic activities and imposed serious risk to the health of the

residents. In December 2016, Beijing issued its first red alert for air pollution of 2016, the most severe alert of a four-tier system. The air-quality index in many regions in Beijing was above 300. The United States considers index levels above 200 very unhealthy and levels above 300 hazardous. The officials of Beijing shut down schools and restricted industrial activity to mitigate the conditions [7]. Such air pollution problems are common in developing countries which rely on combustion of fossil fuels as a source of power generation. According to India's National Health Profile 2015, there has been a 30% increase in cases of acute respiratory infection (ARI) since 2010 [8].One study found that half of the 4.4 million schoolchildren in Delhi would never recover full lung capacity [9]. Phenomena like what happens in Beijing and Delhi are not random incidents but rather the predictable aftermath of excessive consumption of fossil fuels in an uncontrolled manner.

The phenomenon of climate change due to air pollution is not location-bound and the consequences are omnipresent. International efforts have been made to unite nations to develop programs for controlling climate change. Kyoto Protocol was adopted in Kyoto, Japan, in 1997 and enforced in 2006 [10].The protocol had the objective of reducing greenhouse gas emissions to avoid dangerous interference with the climate system. However, the protocol did not succeed as US pulled out and others failed to comply. More recently, the historical COP 21 agreement was reached in Paris which involves nearly 200 countries pledging to cut greenhouse gas emissions. The agreement is a clear indication of general consensus in international level towards mitigating the climate change problem.

The international tendency towards reduction of emission of air pollutants calls for leadership in research and development of clean power generation technologies. Canada has made significant contributions to the research and development of clean energy sources especially in the field of fuel cells. Development of solutions to address the current issues and the future objectives in climate change requires investment in research areas that can substantiate practical methods and products. US introduced a $35 million fund for advanced hydrogen fuel cell technologies that help cut harmful carbon emissions [11]. The European Union continues to support research on fuel cells and hydrogen projects. It is of utmost importance for Canada to strengthen its leadership position by acting upon the opportunity that has arisen at this critical stage in the history of climate change.

In the light of recent release of public information regarding air pollution, some historically deemed insignificant, and the worldwide responsibilities enforced by international agreements, countries such as China and India are actively seeking clean technologies for supplying energy to their fast growing economies. On the one hand, the issue of air pollution damages the image of such countries in the global community. On the other hand, severe air pollution can hinder economic activity and impose costs at such competitive global conditions. In November 2015, the Canadian government signed a trade deal worth as much as $2.5 billion with China including articles about green technologies [12]. Furthermore, Canada is actively seeking free trade agreements with both China and India in order to foster economic growth and introduce new markets for Canadian products. Such markets are ideal for green technologies such as fuel cells as it can have significant impact on reduction of pollutant emission in these countries.

1.1 Fuel Cell Fundamentals

Fuel cells are a very flexible technology with potential to be used in applications ranging from automotive industry to space. There are many types of fuel cells including Solid Oxide Fuel Cell (SOFC), Alkaline Fuel Cells (AFC), Phosphoric Acid Fuel Cell (PAFC), Proton Exchange Membrane Fuel Cell (PEMFC), Molten Carbonate Fuel Cell (MCFC), and Direct Methanol Fuel Cell (DMFC). Of all the various types, the low temperature fuel cells PEMFC are the most widely applicable type and are expected to lead the majority of technological advancement [13]. Fundamentals of PEMFC is described in this section.

PEM fuel cells, also known as ion exchange membrane fuel cells (IEMFC), solid polymer fuel cells (SPFC), and polymer electrolyte fuel cells (PEFC) use a proton exchange porous membrane as electrolyte. They have received much attention in the recent years due to their simplicity, viability and quick start-up and have become the most promising candidate as the zero emission power source for transportation [5].

The membrane at the heart of a PEM fuel cell has a unique characteristic: it is impermeable to gas molecules but it conducts protons. The membrane is sandwiched between two porous and electrically conductive electrodes usually made of carbon fiber paper. At the interface of the porous carbon paper and the membrane exists a layer of platinum supported on carbon, which acts as catalyst. This catalyst layer is critical to the operation of the fuel cell in low temperatures.

The electrochemical reactions in the fuel cell happen simultaneously in the cathode and anode of the cell, as shown in Figure 2. At the anode, hydrogen atoms are split into two hydrogen ions producing two electrons that transfer through an outside circuit to the cathode where oxygen atoms react with the hydrogen ions to produce water based on the following equations:

$$H_2 \rightarrow 2H^+ + 2e^- \tag{1}$$

$$\frac{1}{2}O_2 + 2H^+ + 2e^- \rightarrow H_2O + waste\ heat \tag{2}$$

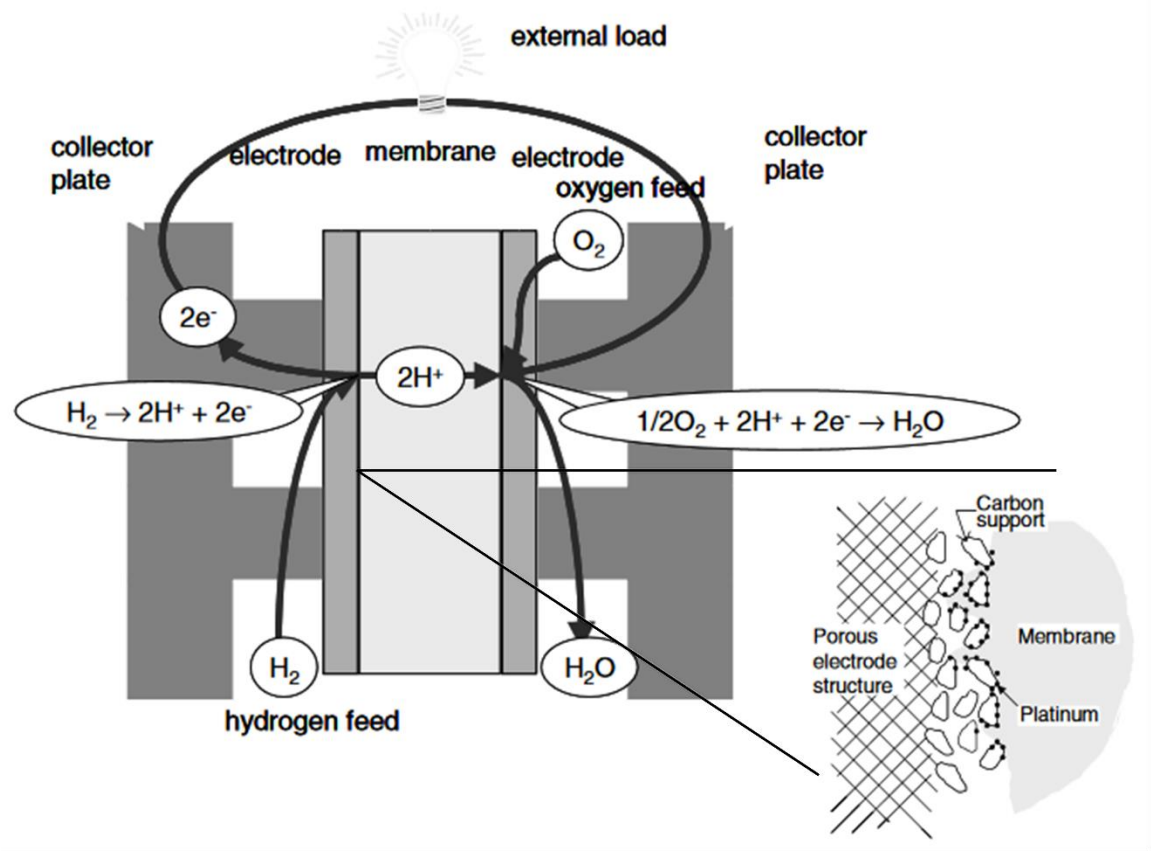

Figure 2 : Basic principle of operation of PEM fuel cell [14]

Water produced in this reaction is collected at the membrane-catalyst interface in liquid form and needs to be removed hence making water control one of the major issues in PEM fuel cells. Furthermore, waste heat is generated in the water formation reaction as a byproduct which is removed from the fuel cell using cooling plates that sandwich the entire cell. With pure hydrogen and air used for the cell operation, optimal stoichiometry is around 1.1~ 1.2 for hydrogen and 2 for oxygen. However, since 20% of air is oxygen, high airflow is required for the cell reaction. The operating cell voltage is usually between 0.6 and 0.7 V for better efficiency and power density. At the current level of technology, operating current densities from 300 to 500 mA/cm^2 are feasible when the cell is operating with pure hydrogen and air, and as high as over 1 A/cm^2 when running on pure hydrogen and oxygen [5].

One of the common methods for visualizing the performance of a fuel cell is through a potential vs. current density plot. Figure 3 shows the potential vs. current density curves for leading types of fuel cells. Cell potential refers to the electric potential difference between the anode and cathode of cell. In practice, a fuel cell experiences energy losses in terms of voltage loss. The phenomenon giving rise to voltage loss is known as polarization, therefore, the plot of cell potential versus current density is also known as polarization curve [5].

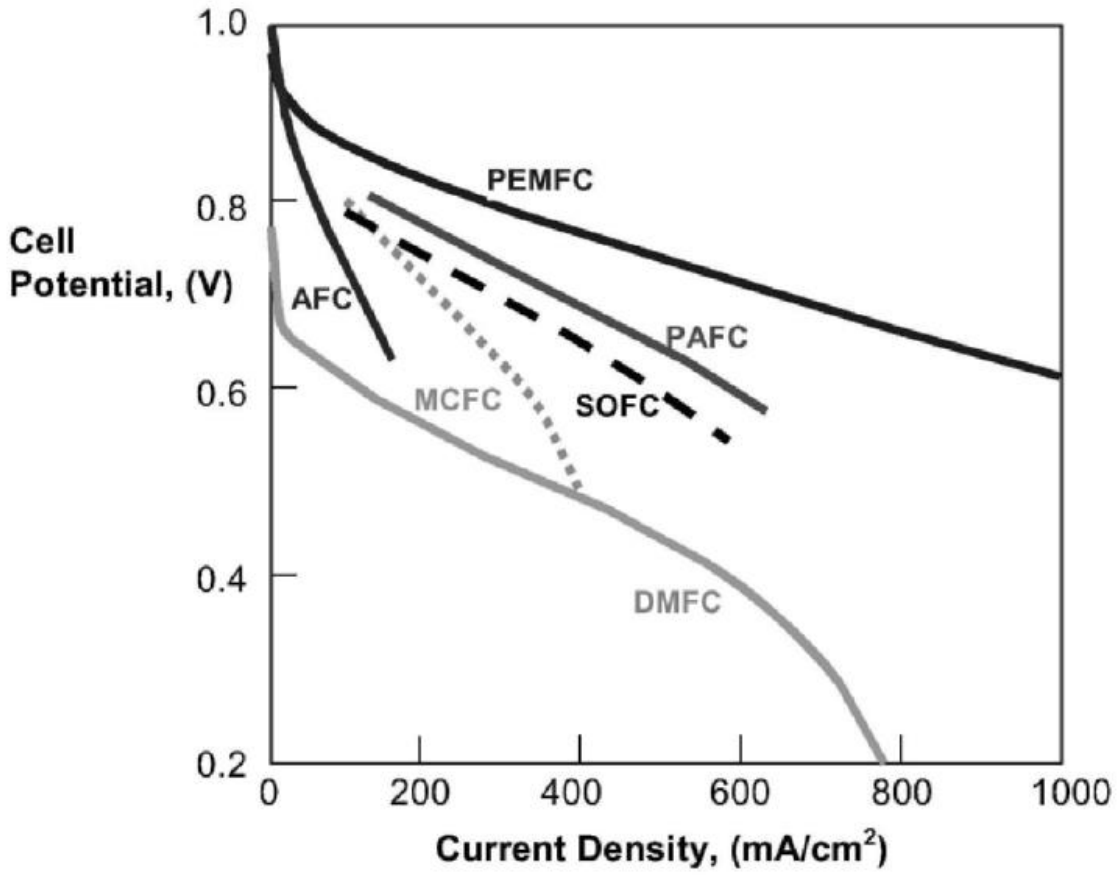

Figure 3 : Plot of cell potential vs. current density for Oxide Fuel Cell (SOFC), Alkaline Fuel Cells (AFC), Phosphoric Acid Fuel Cell (PAFC), Proton Exchange Membrane Fuel Cell (PEMFC), Molten Carbonate Fuel Cell (MCFC), and Direct Methanol Fuel Cell (DMFC) [15]

1.2 PEM Fuel Cells Components and Configurations

Figure 4 illustrates components in a single PEM fuel cell. The cell usually consists of membrane electrolyte, two catalyzed electrodes, gaskets, and end plates [5]. In the assembly, MEA refers to the membrane electrode assembly which is fabricated by hot pressing two electrodes onto the porous membrane with the catalyst layer deposited onto the membrane. The catalyst is usually platinum particles supported on carbon layer on the membrane electrolyte. The end plates can be designed to accommodate coolant flow channels for removing the excess heat generated in the fuel cell.

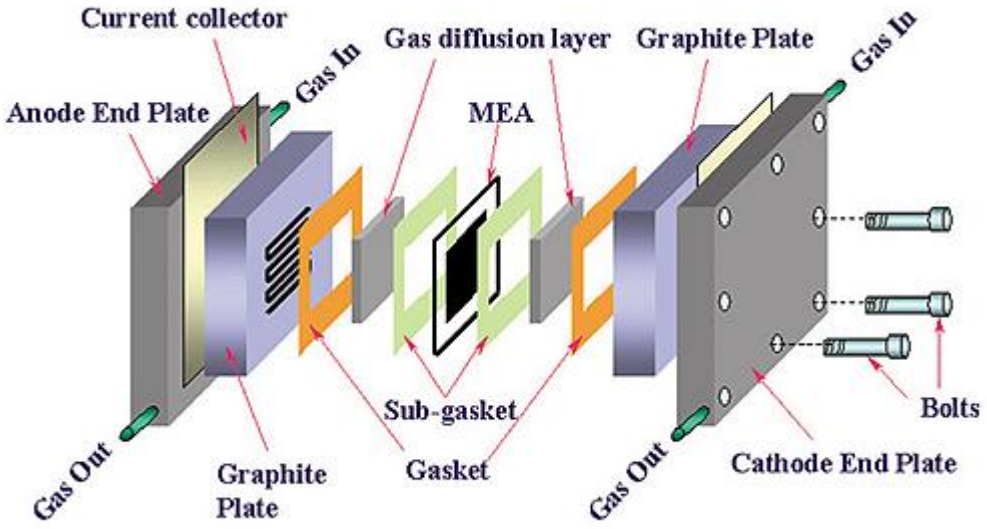

Figure 4 : Configuration of components of single fuel cell [16]

Single fuel cells produce less than 1V of electricity, which is very small for operation of small electric devices, let alone a vehicle. Therefore, multiple fuel cells are usually stacked together into a fuel cell stack. A stack can be configured in parallel or series : In parallel stack, all cells are individually fed from a common hydrogen/air inlet whereas in a series configuration, the gas from the outlet of the first cell is fed to the inlet of the second cell and so on [17]. Figure 5 shows a PEM fuel cell series stack where individual cells are electrically connected with interconnects.

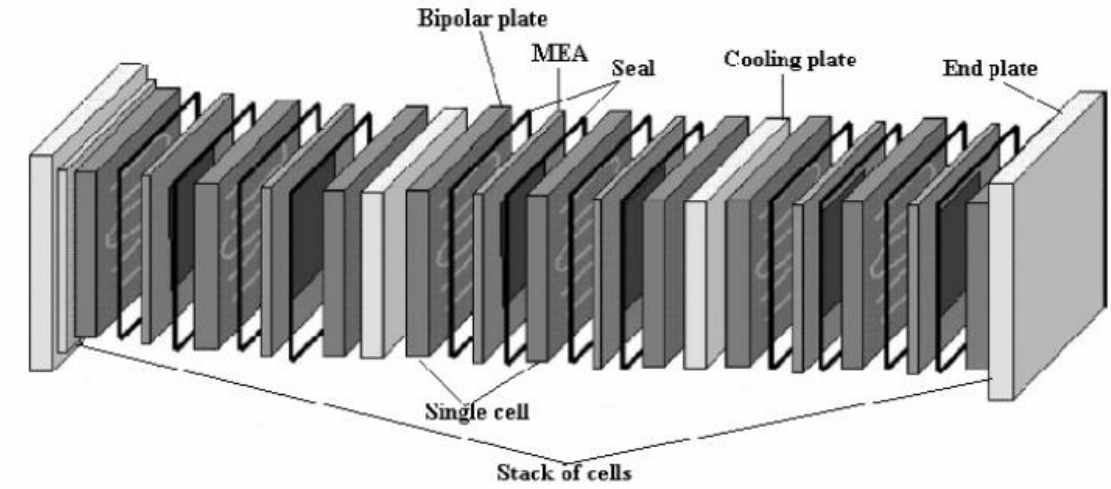

Figure 5 : Series configuration of a stack of fuel cells [17]

Air intake of fuel cells is a critical component in transportation applications functioning similar to air intake of internal combustion engines. In laboratory setup, operation of a fuel cell can be tested by varying parameters such as the intake air pressure or the temperature of the intake air, or more importantly, the humidity level of the intake air. For instance, the pressure of the air intake could range from atmospheric to about 8 atm pressure. The humidity of the incoming air is also very

important. When the humidity level in the air is low, the membrane inside the cell dehydrates, and when it is too high flooding occurs. Both lead to suboptimal conditions for the membrane. It is also very important to ensure the temperature of the intake air does not exceed 130 ℃ as it could irreversibly damage the membrane [15]. While certain combinations of these parameters are essential to the characterization process of fuel cells, one must consider the feasibility of such combinations in the real world scenarios such as fuel cell powered vehicles. For example, in lab testing, the hydrogen fed to the fuel cell is usually of the highest purity, which is considered research grade hydrogen, not practical for large scale usage due to high cost. In addition, building the air pressure of the intake of a fuel cell to 8 atm in a fuel cell powered vehicle, is impractical.

Another issue that is usually ignored in laboratory conditions is the presence of particulate matter in the air stream used for the intake of fuel cells. Usually, the compressed air used in laboratories passes through multiple filters where particulate matter is removed. Furthermore, there is usually no major source of fine particles in the vicinity of the testing apparatus in laboratories and even if there is, the effect usually goes unnoticed. However, fuel cells in vehicles are exposed to a variety of particles based on the environment they operate in. The surrounding air that is used to oxidize hydrogen inside a fuel cell passes through the gas diffusion layer (GDL) that has pore size in the range of micro to nanometers. Therefore, common atmospheric particles in the micrometers range could potentially obstruct the pores of the GDL and prevent passage of air through the pores hence deteriorating the performance of the fuel cell. With the large-scale commercialization of fuel cells gaining more momentum than ever before, a better understanding of the effect of outside-laboratory operating conditions on the performance of fuel cells requires special attention.

1.3 Objectives

An understanding of the effect of particulate matter on the performance of fuel cell is imperative in paving the way for large-scale commercialization. Upon utilization of fuel cells in vehicular transportation, particle matter is expected to interact with various fuel cell components including the gas diffusion layer (GDL). The objective of this thesis is to numerically study the entrapment of particulate matter in the GDL under various humidity conditions. The work aims to provide a systematic approach towards modeling of the physical phenomena and characterize the interaction of particles and GDL as well as developing a model for effect of humidity on particle-GDL interaction. The thesis uses a purely numerical approach and aims to provide information which can be validated with future experimental results.

1.4 Organization of Thesis

The overall organization of this thesis is based on developing and validating a base model of a multi-fiber GDL model followed by applying a humidity model. First, a single fiber model without particles will be considered. Then particles will be added to the single fiber model followed by increasing the number of the fibers in the model. A humidity model will be presented based on the effect of humidity on the particles and the results of the humidity model are analyzed in the context of an actual GDL. Recommendations will be made about the operating conditions of a GDL at the end.

2 Literature Review

All energy producing systems are prone to performance degradation if the quality of the input of the system diminishes. The inputs of a PEM fuel cell are hydrogen and oxygen, the latter commonly supplied in the form of air with 20% oxygen content. The purity of the hydrogen and oxygen play a major role in the operation of the fuel cell. There are two major forms of contamination that can be introduced to these inputs: chemical and physical. Chemical contamination refers to the mixing of gases such as carbon monoxide, while the physical contamination refers to presence of non-gaseous components such as particulate matter. The following sections review literature pertaining to chemical and physical contamination and their significance in PEM fuel cell operation. The section proceeds by drawing a connection between particle capture and fuel cells and concludes by highlighting the gaps in literature with regards to interaction of particles and fuel cell components, namely the gas diffusion layer. The focus and approach of the thesis is outlined at the end.

2.1 Impurities in Fuel Cell Input Gases and their Impact

2.1.1 Hydrogen Contamination

Impurities in the hydrogen stream of fuel cells are due to the hydrogen production process. Hydrogen is produced by reformation of oxygenated hydrocarbons such as methane from natural gases [18], electrolysis [19], and partial oxidation of small organics [20]. The reformation process results in unavoidable impurities in hydrogen such as carbon monoxide, CO, carbon dioxide, CO_2, and sulfur compounds [21]. Hydrogen produced by reformation could contain 0.5 up to 1 vol% CO and it must be reduced to below 0.1 vol% for extended operation of fuel cells [22]. Takenaka et al. suggests a maximum CO concentration of 20 ppm in hydrogen for polymer electrolyte fuel cells [23]. Figure 6 shows the effect of carbon monoxide poisoning of a single PEM fuel cell as reported by Oetjen et al. [24]; CO concentrations as low as 25 ppm have adversely affected the performance of the cell.

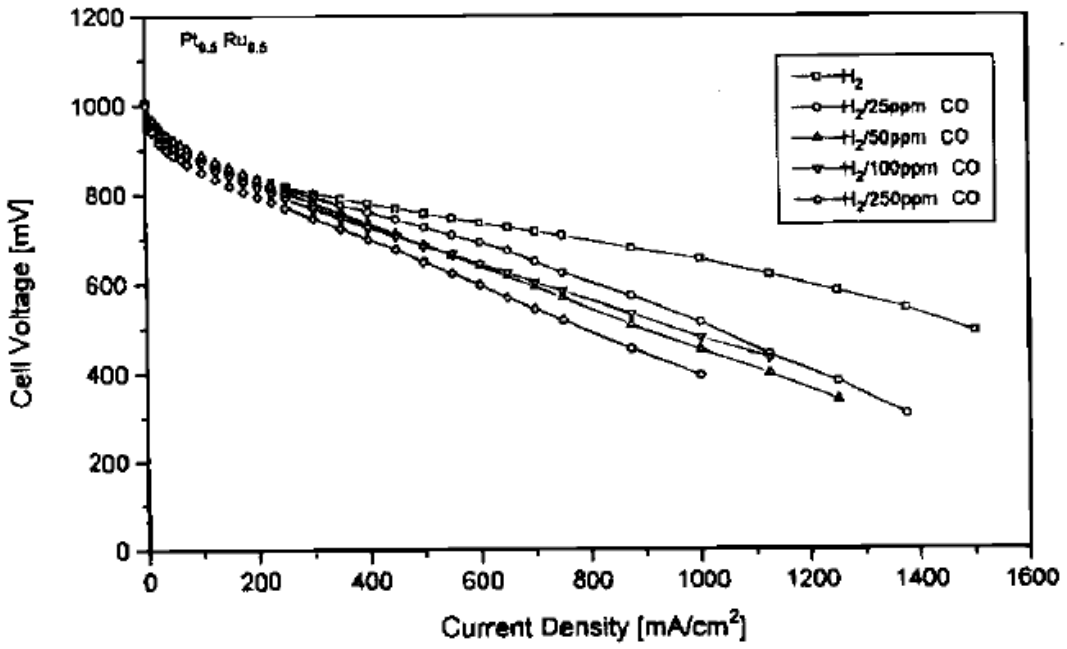

Figure 6 : Polarization curve for steady state performance of a single PEM fuel cell showing the effect of CO [24]

Several methods have been suggested for mitigation of anode contamination: CO-tolerant catalyst, Pt alloy catalyst, air/oxygen bleeding, high operation temperature, and pre-treatment of the reformate, with the latter being the most suitable for removing other contaminates such as ammonia and hydrogen sulfide [17].

Other sources of contamination in the hydrogen stream include impurity ions, investigated by Okada et al. [25], battlefield contaminants , studied by Moore et al. [26], hydrogen sulfide, studied by Mohtadi et al. [27], and ammonia, examined by Uribe et al. [28].

2.1.2 Air Contamination

Contamination in the anode side, hydrogen stream, has received much attention over the years. However, the cathode side, air stream, is also prone to contamination. The major sources of pollution in air stream of a fuel cell are nitrogen oxides (NO, NO_2), sulfur oxides (SO_2, SO_3), and carbon oxides (CO, CO_2) and particulate matter. In 1979, Contractor and Lal report adsorption of hydrogen sulfide, H_2S, and sulfur dioxide, SO_2, on the platinum catalyst reducing the active area of the catalyst [29]. In 2004, Mohtadi et al. experimentally studied the effect of NO_2 and SO_2 on the performance of PEM fuel cells, concluding that contamination due to sulfur compounds has a stronger effect than NO_2 [30]. The authors also observe complete recovery of cell performance after exposure to NO_2 while the cell only partially recovered from SO_2 exposure. This phenomenon is shown by plotting the polarization curve for a PEM fuel cell exposed to 2.5 ppm of NO_2 and 5 ppm of SO_2 as shown in Figure 7 and Figure 8. Similar results are reported by Yang et al. [31], and Angelo et al. [32].

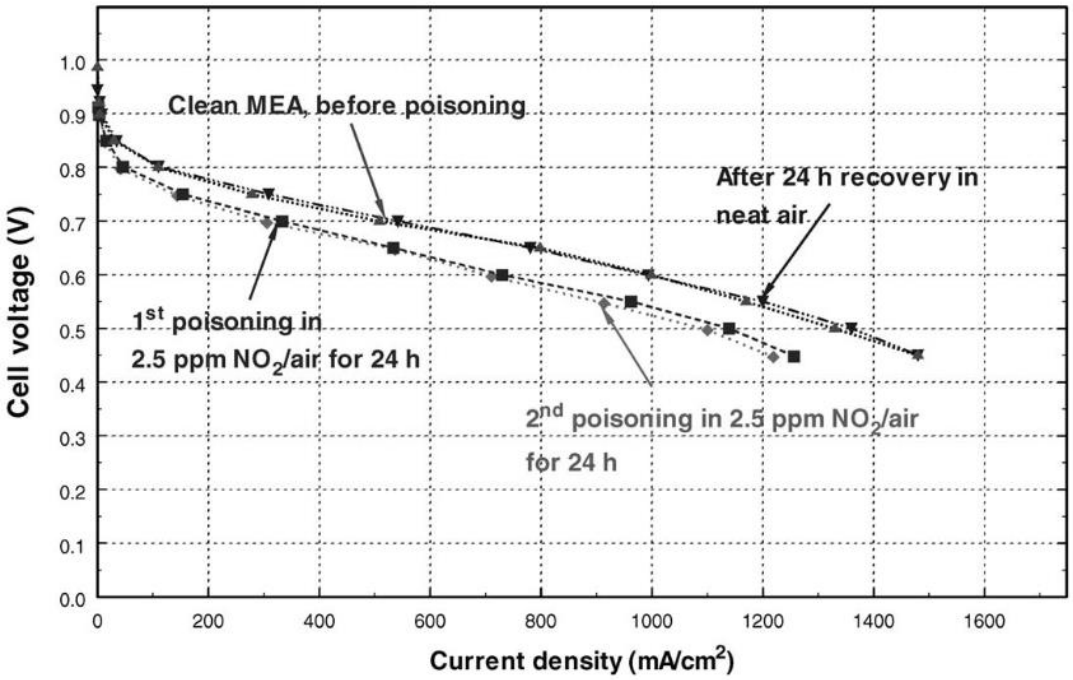

Figure 7 : Polarization curve for steady state performance of a single PEM fuel cell showing the effect of NO_2 [30]

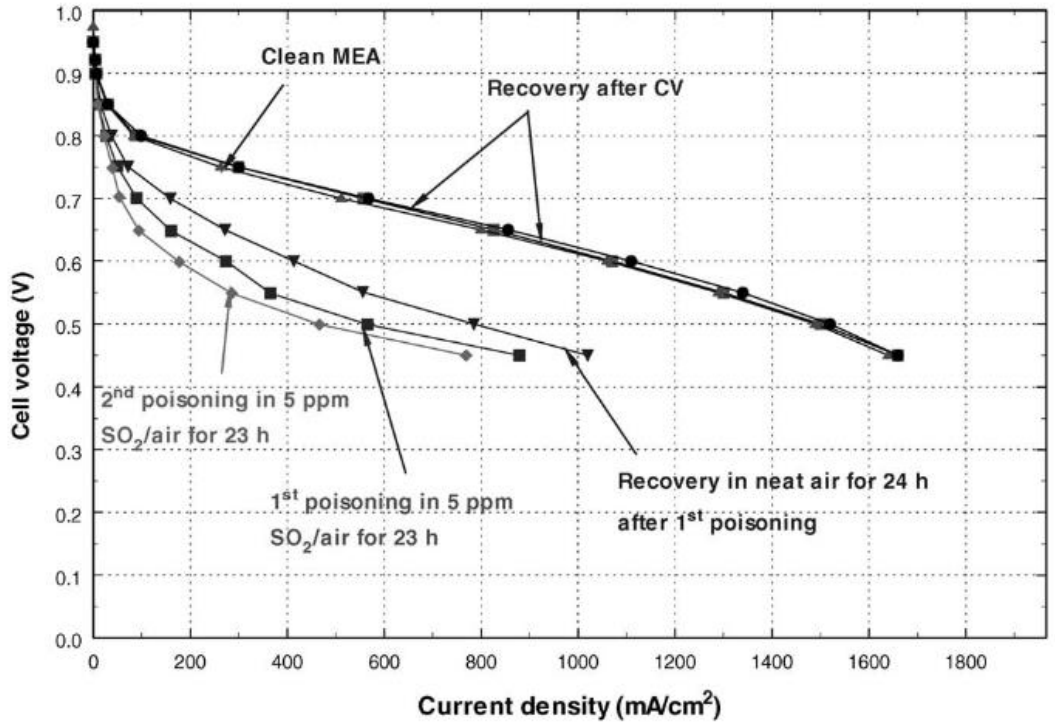

Figure 8 : Polarization curve for steady state performance of a single PEM fuel cell showing the effect of SO_2 [30]

Ammonia has traditionally been considered a contaminant only in the anode side, where its concentration can reach 150 ppm [33] as opposed to a concentration of around 1 ppm in air. In 2012 Yuan et al. studied the effect of ammonia at the cathode side and speculated membrane conductivity reduction as the source of performance degradation, shown in Figure 9 [34].

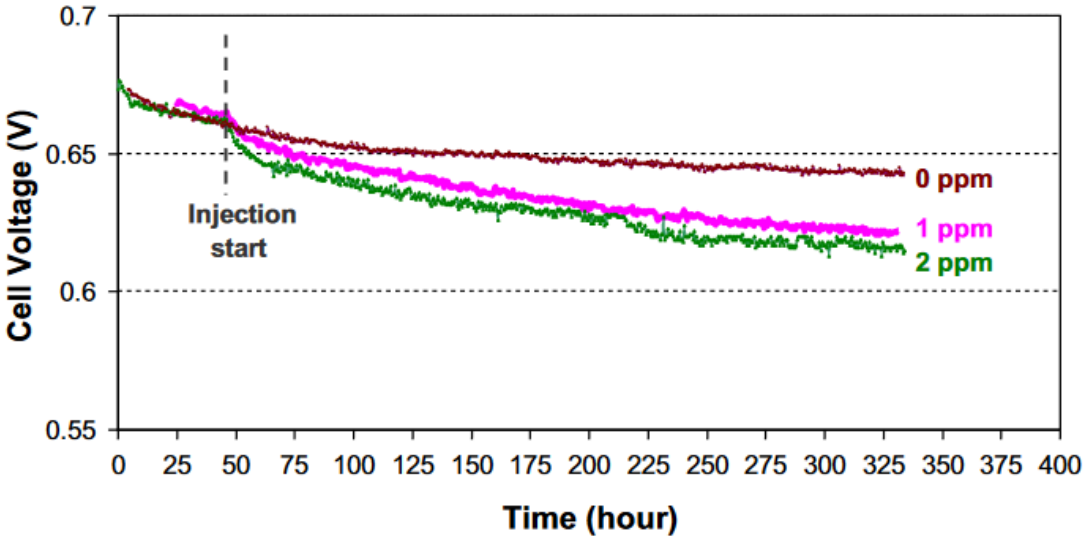

Figure 9 : Effect of ammonia contamination on single PEM fuel cell at current density of 1 A cm^{-2} [34]

St-Pierre et al. developed a list of 260 airborne contaminants originating from various sources which could potentially affect the performance of fuel cells [35]. The authors proceed with shortlisting of 21 first tier contaminants and characterizing their effect on the performance of PEM fuel cell. They categorized the effect of the contaminants into 5 categories: no effect, recoverable effect, partly recoverable effect, irrecoverable effect and supra-recoverable effect [36]. St-Pierre et al. conclude by emphasizing the need for intense resources in order to study the effect of the many potential contaminants thoroughly.

Faber et al. [37] investigate the effect of different airborne particulate contaminants such as oxalic acid, soot, ammonium sulfate, and sodium chloride on the performance of a passive air-breathing PEM fuel cell experimentally. Faber et. al finds the degradation of cell performance due to aerosol particles much less severe than degradation due to NO_x exposure. The authors report an insignificant low performance degradation due to aerosol particles. It is noteworthy that the cell used in Faber et al.'s experiment was an air-breathing one which has a much lower performance compared to air-forced cells.

There are many different species in air and one needs significant resources to study the effect of each species in isolation. It is also important to consider that even though certain species might be extremely detrimental to the performance of PEM fuel cells, one needs to take into account whether said species are available in the air in high enough concentrations. The next section discusses the significance of select number of contaminants.

2.1.3 Contamination Significance Test

A sound engineering design takes into account the worst case scenario, and the topic of this thesis is no exception to the rule. A reliable fuel cell for transportation purposes needs to withstand various operating conditions especially the quality of the intake air. New Delhi, as one of the potential cities for implementation of fuel cell powered transportation systems, is known to have sub-optimal air quality. The data collected from various areas in Delhi, India are used as a representative of highly polluted conditions and the results are used to test common contaminants such as carbon monoxide, sulfur dioxide, nitrogen dioxide, and ammonia for which data is available. The air quality of Ottawa is used for comparison.

2.1.3.1 Sulfur Dioxide

Table 1 shows the concentration of sulfur dioxide (SO_2) in 6 regions in Delhi, India as well as concentration in Ottawa, Canada measured daily starting January of 2012 ending December of 2015. Measurements are obtained from Central Pollution Control Board [38] and Environment and Climate Change Canada [39] for the Indian and Canadian data respectively. The relatively high average sulfur dioxide concentration in Delhi regions as opposed to Ottawa, can be observed by comparing the mean values in Table 1.

Table 1 : SO_2 concentration in various regions of Delhi, India and Ottawa, Canada

SO_2 Concentration [µg/m^3]					
	Min	Max	Mean	Standard deviation	Number of observations
Delhi ITO	1.04	309.98	8.85	12.62	819
Delhi Shadipur	1.11	139.88	13.87	11.43	1111
Delhi DCE	1.36	63.06	11.95	8.64	554
Delhi Mandir	1.75	49.14	16.74	9.28	113
Delhi Puram	0	50.7	16.70	8.81	453
Delhi PunjBagh	0.14	150.59	17.64	13.64	446
Ottawa	0	42.54	2.76	4.00	1096

Sulfur dioxide concentrations below 80 µg/m^3, equivalent to 0.03 ppm, are considered environmentally safe, according to U.S. National Ambient Air quality Standards NAAQS [40]. Figure 10 shows the frequency distribution of the regions in Delhi with the highest sulfur dioxide. While the levels are below the hazardous threshold, the distribution shows two important facts. First, in all four regions, the distributions are positively skewed suggesting very few number of days with sulfur dioxide concentration more than the hazardous threshold. Secondly, there is high number of days with sulfur dioxide concentration in the range of 5-20 µg/m^3 in all four regions. The later observation bears much significance because it means that a fuel cell operating in these regions would be consistently exposed to sulfur dioxide concentration levels between 5-20 µg/m^3; a condition which is absent in the operation of the same fuel cell in Ottawa.

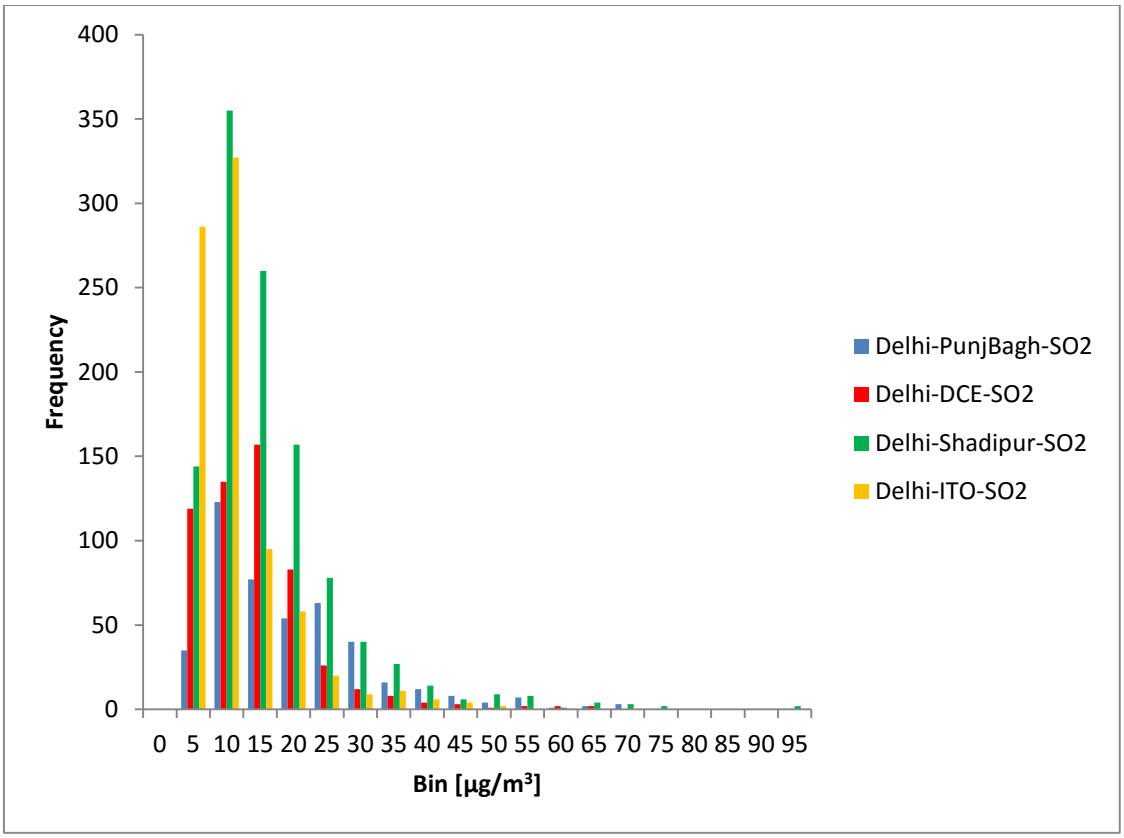

Figure 10 : Histogram of four highest sulfur dioxide concentrations in Delhi, India

Shadipur SO_2 concentration is determined to be between 11.74 µg/m^3 and 16 µg/m^3 with 95 percent confidence. This range is about 50 times smaller than the minimum sulfur dioxide required in the cathode stream to substantially affect the performance of a PEM fuel cell which is 1 ppm. This means that the current level of sulfur dioxide in these regions is not expected to have a material effect on the performance of PEM fuel cells.

Table 2 shows the concentration of carbon monoxide, CO, in three regions in Delhi and in Ottawa. The hazardous threshold level for carbon monoxide is 14.17 mg/m^3, equivalent to 9 ppm [41]. It must be noted that the variation in the number of observations is due to absence of reliable data hence making it difficult to compare Ottawa and Delhi CO levels. Based on the average value of all observations, carbon monoxide concentrations seem to show a much higher average in Delhi than in Ottawa.

Table 2 : CO concentration in various regions of Delhi, India and Ottawa, Canada

CO Concentration [mg/m^3]					
	Min	Max	Mean	Standard deviation	Number of observations
Delhi Mandir	0	4.84	1.06	1.08	397
Delhi Puram	0.52	19.9	1.94	1.29	400
Delhi PunjBagh	0.34	10.36	2.02	1.60	427
Ottawa	0.152	1.162	0.38	0.16	1067

Takenaka et al. suggests a maximum CO concentration of 20 ppm, or 23 mg/m^3 for operation of PEM fuel cell which is about 10 times larger than the mean CO concentration measured in Punjbagh and Puram and 20 times the mean concentration in Mandir as indicated in Table 2 hence, rendering CO levels insignificant in the said regions.

2.1.3.2 Nitrogen Dioxide

Similar observations are made about the concentrations of nitrogen dioxide, NO_2, as shown in Table 3. The environmental standard for nitrogen dioxide is 70 µg/m^3, equivalent to 54 ppb [40].

Table 3 : NO_2 concentration in various regions of Delhi, India and Ottawa, Canada

NO_2 Concentration [µg/m^3]					
	Min	Max	Mean	Standard deviation	Number of observations
Delhi ITO	0.00	437.77	80.59	63.42	771
Delhi Shadipur	0.00	684.35	49.91	50.32	880
Delhi DCE	0.00	169.58	23.59	14.39	676
Delhi Mandir	2.23	212.58	67.44	37.25	471
Delhi Puram	0.00	184.44	73.17	37.77	499
Delhi PunjBagh	0.65	579.75	103.96	75.84	435
Ottawa	3.67	95.00	32.31	20.13	1089

Moore et al. suggests a minimum NO_2 concentration of 400 ppb, or 762 µg/m^3, in order to substantially affect the performance of a PEM fuel cell [26]. The maximum mean value from Table 3 belongs to Punjbagh with a value about 7 times smaller than the threshold suggested by Moore et al.. This means that the nitrogen dioxide concentration levels are insignificant.

2.1.3.3 Ammonia

Table 4 shows ammonia, NH_3, levels in three regions of Delhi, India. The environmental standard for ammonia is 100 µg/m^3, equivalent to 141 ppb [40]. There is no data from Environment and Climate Change Canada for ammonia levels in Ottawa.

Table 4 : NH_3 concentration in various regions of Delhi, India

NH_3 [µg/m^3]					
	Min	Max	Mean	Standard Deviation	Number of observations
Delhi Mandir	9.57	61.18	34.60	11.05	135
Delhi Puram	0.37	139.28	46.93	29.59	481
Delhi PunjBagh	1	192.67	54.59	29.10	468

Delhi Punjbagh has the highest average of all three with value of about 55 µg/m^3 which is about 13 times smaller than the threshold suggested by Yuan et al., 1 ppm equivalent to 700 µg/m^3. Therefore, the ammonia levels are considered insignificant.

2.1.3.4 Particulate Matter

Table 5 summarizes particulate matter measurements in various regions of Delhi and Ottawa. The concentrations reported correspond to the mass of particles with diameter smaller than 2.5 µm per cubic meter of air. The short term (24-hour) standard is 35 µg/m^3 and the long-term standard is 15 µg/m^3 [40]. All the Delhi regions presented in Table 5 have average concentrations above the standard.

Table 5 : PM2.5 concentration in various regions of Delhi, India and Ottawa, Canada

PM2.5 [µg/m^3]					
	Min	Max	Mean	Standard Deviation	Number of observations
Delhi ITO	10.87	378.64	132.45	66.58	568
Delhi Shadipur	14.6	657.85	97.83	121.18	110
Delhi Mandir	12.92	149.64	59.23	28.04	135
Delhi Puram	16.93	239.55	73.67	38.38	115
Delhi PunjBagh	18.33	236.96	84.25	39.73	138
Ottawa	1	95.00	11.99	7.96	1096

A threshold for particulate matter concentration in the cathode stream of PEM fuel cells is not currently available which makes it difficult to determine the significance of the concentration levels in the said regions.

2.2 Particulate Matter

Particulate matter could affect the performance of fuel cells through two major mechanisms. Firstly, particles could obstruct the passage of air through the porous layers of fuel cells, especially the GDL. Secondly, particles could release gaseous contaminants such as sulfur dioxide or carbon monoxide upon passage through the cathode of the fuel cell if they were exposed to such gases prior to entry into the fuel cell. The second mechanism is important when the concentration levels of contaminating gases are high outside the fuel cell, which was determined not to be the case in the previous section. Therefore, the first mechanism is considered only.

The interaction of particles with porous media in fuel cells is similar to the operation of fibrous filters. For instance, the GDL in fuel cells is made up of several layers of carbon fibers or woven carbon cloth stacked on top of each other [42], similar to how a fibrous filter is fabricated. Filtration using fibrous filters is one of the largest and relatively inexpensive means for removing submicron particles from gas streams. Fiber filtration is used in coal-fired plants, chemical processes, hospitals and indoor air purification to recover valuable products. Usually made of matted glass or quartz fibers, fibrous filters offer various performances depending on the type of aerosol that is targeted. The principles of operation of fibrous filters can be used in understanding the interaction of particulate matter and the GDL in fuel cells under different humidity conditions. The following sections review the literature pertaining to fibrous media.

2.2.1 Particulate Matter and Fibrous Media

In the field of air filtration, the model developed by Kuwabara in 1959 [43] and the consequent slip flow modification by Brown in 1993 [44] have been broadly used as benchmarks. Many researchers have used numerical simulations to study the gas-solid flow in various arrangements of fibrous media. In 2003, Karadimos and Once presented a simple single fiber model for loading process of aerosol particles on fibrous filters [45]. They developed a CFD code and used particle trajectory simulation to study the change in the shape of fiber in each stage of loading. They have used Kuwabara's staggered fiber arrangement. Dunnett and Clement studied the deposition of particles on fibers using a numerical flow field around a single fiber based on Kuwabara's model in 2006 [46]. They used the assumption that the particles form a smooth solid layer around the fiber. Similar studies are done by Kanaoka et al. in 2001 [47], Tanthapanichakoon et al. in 2003 [48], Przekop et al. in 2004 [49], and Hui et al. in 2009 [50]. All these studies used two-dimensional staggered arrangement for the fibrous media without taking into account the actual structure of fibers. In 2010, Hosseini and Tafreshi addressed this issue by developing a two-dimensional model of randomly placed fibers for a filter application [51]. They also implemented slip boundary conditions and concluded that aerodynamic slip improves the collection efficiency of filter medium. Figure 11 shows the single fiber efficiency results of Hosseini's disordered 2D model compared with existing semi-analytical correlations.

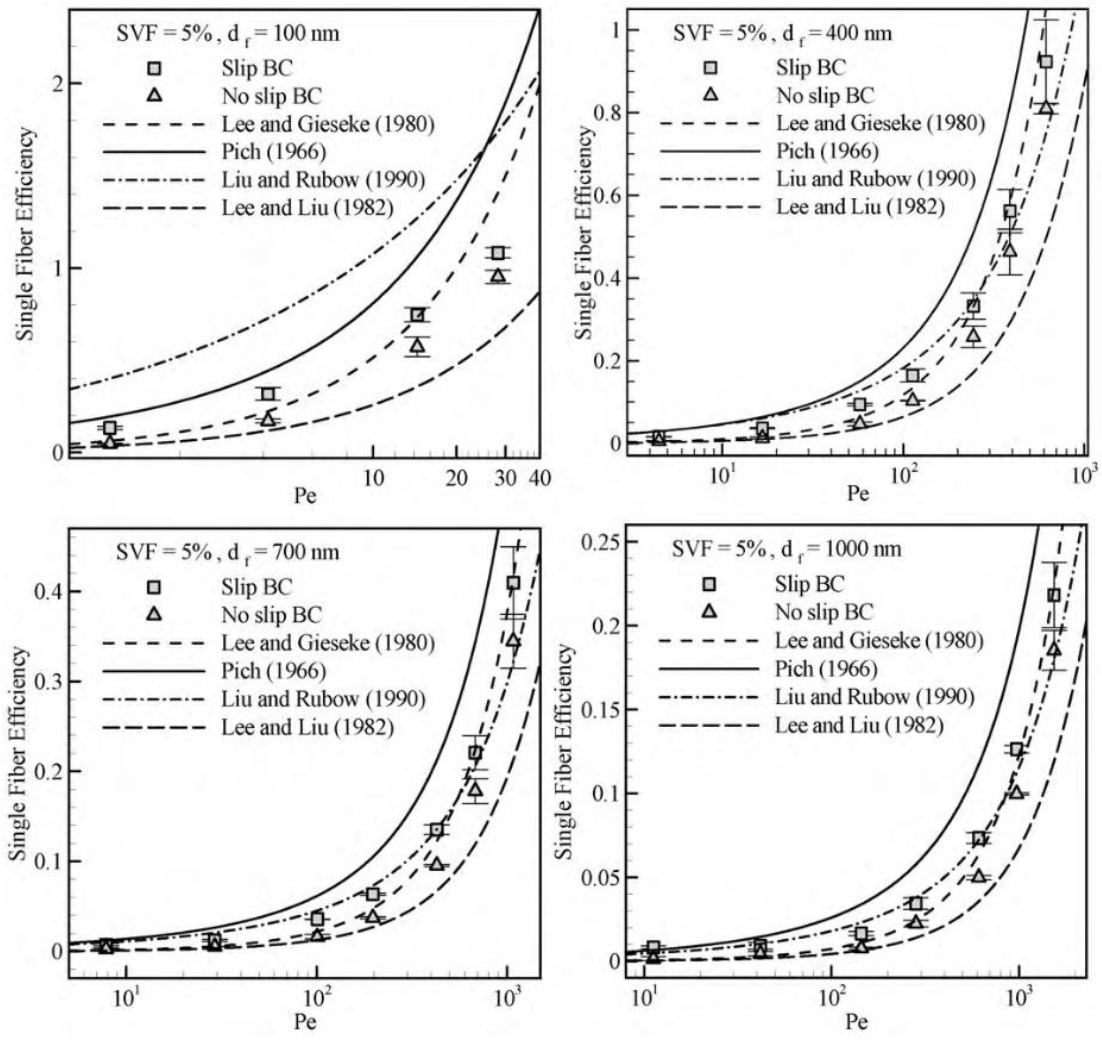

Figure 11 : Interception single fiber efficiency compared with existing semi-analytical correlations for media with fiber volume fraction of 5% but different fiber diameters of 100, 400, 700, and 1000 nm [51]

Three-dimensional imaging methods including X-ray microscopy and Magnetic Resonance Imaging (MRI) are used by several researchers to develop 3D models of fibrous media. In 2005, Faessel et al. use X-ray tomography to develop a 3D model of fibrous networks in low density wood-based fiberboards [52]. Similar attempt is made by Lehmann et al. in 2005 [53] and Hoferer et al. in 2007 [54] using MRI.

In 2006, Wang et al. developed a virtual three-dimensional model of fibrous media using microscopic images of lightweight spun-bonded filter media [55]. They used this model to predict the initial pressure drop downstream of the fibrous media for different solid volume fractions ,as shown in Figure 12. Their 3D model pressure drop shows better agreement with the experimental results compared to the traditional 2D models.

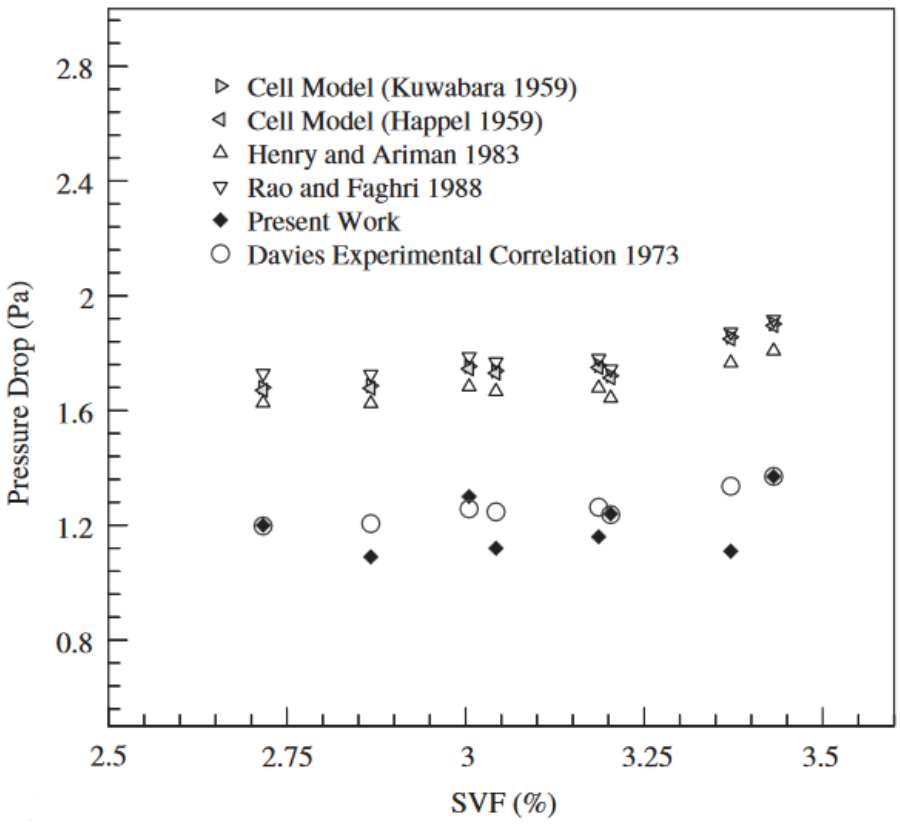

Figure 12 : Pressure drop calculation from CFD simulations compared with Kuwabara's cell model and empirical results [55]

In 2010, Hosseini and Tafreshi developed a 3D model of the internal microstructures of electrospun fibrous materials in order to study particle collection efficiency [56]. They used random number generation for creating the fibrous media and challenged the model with aerosols in size range of 25 to 1000 nm. The comparison of their 3D and 2D models are shown in Figure 13.

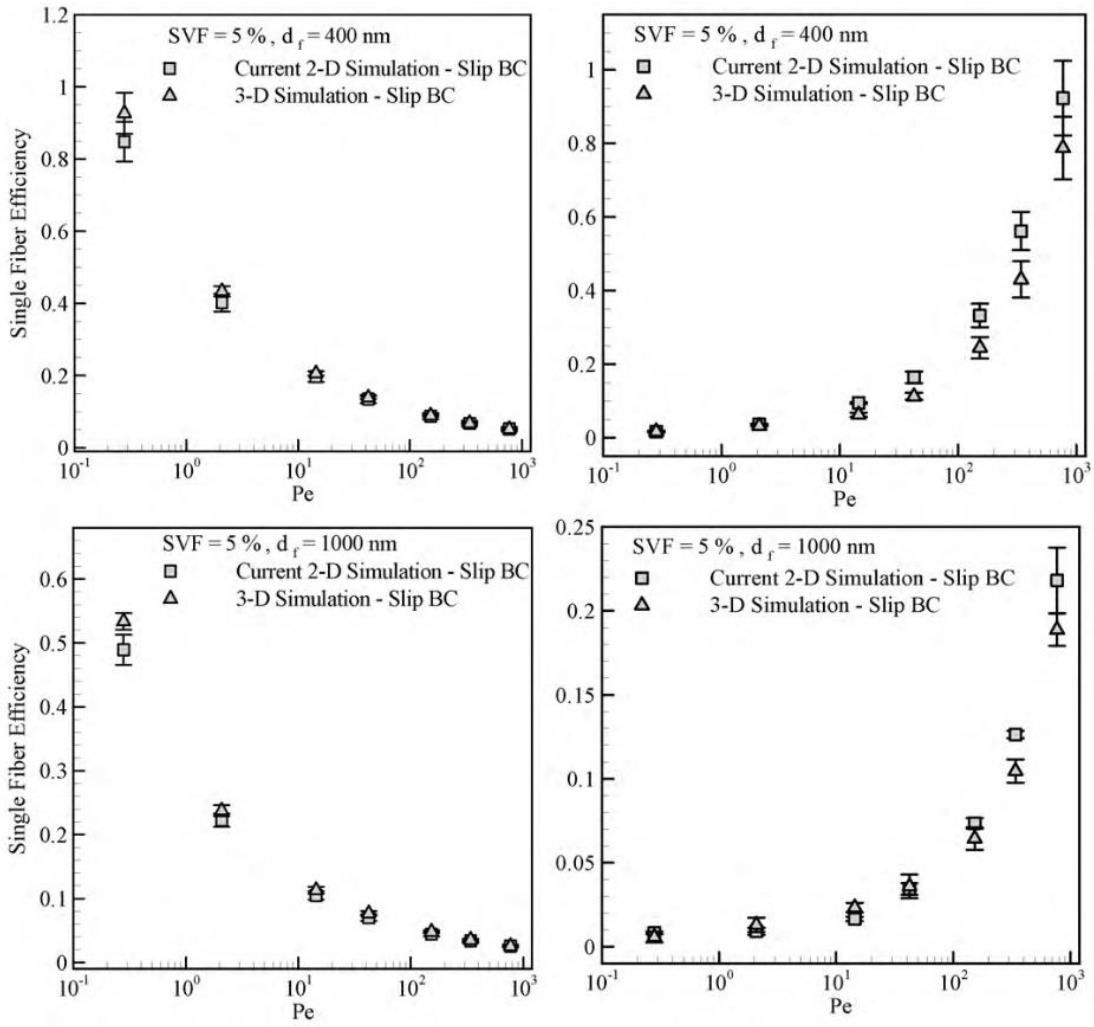

Figure 13 : Comparison between particle collection efficiency of aerosol filters modeled using disordered 2D and fibrous 3D geometries [51]

The authors argue that while the 3D simulation technique does not need any empirical correction factors, it is much more computationally expensive to calculate and given the close agreement between the two models, a 2D model can be just as useful.

2.2.2 Particulate Matter and Humidity

Most of the research pertaining to the interaction of particles and fibrous media focus on filtration applications and a lot of attention has been paid to the operating conditions of filters. The GDL in fuel cells is very similar to filters however, it serves an entirely different function: The GDL is not meant to remove particles from the incoming flow, but instead, it is meant to accommodate diffusion of incoming gas. The unique feature about the gas stream of a PEM fuel cell is its high humidity. The presence of humidity in the stream differentiates particle-fiber interaction from the traditional models developed for filtration purposes. The previous studies on the effect of humidity on particle filtration are limited and inter-disciplinary connections need to be made in order to extend the findings to fuel cells.

In 2014, Xu et al. investigated the effect of humidity on filtration efficiency and pressure drop of vehicle cabin air filters [57]. They studied effect of humidity of commercially available cabin air filters by characterizing the efficiency and pressure drop under various humidity levels. Xu et al. found significant increase in filtration, up to 15%, as the humidity level increased. They also observed that the pressure drop across the filter increased as the water content of the flow was absorbed by initially deposited dust particles hence impeding the flow.

Miguel attempts to explain the effect of humidity on the pressure drop of fibrous filters by focusing on the effect of humidity on the density of the cake of hygroscopic and non-hygroscopic particles [58]. Miguel's investigation involves curve-fitting of the density of cake of particles at different humidity levels and establishing empirical constants to adjust for hygroscopicity of the particles. Miguel's proposed model is a transient model that requires duration of filtration, characteristics of aerosol particles and mass loading of particles and empirical constants as inputs. However, Miguel's model does not account for effects of humidity on the particles and rather, focuses on the change in density of the cake of particles. The model predicts higher efficiency when at elevated humidity levels except for hygroscopic particles at humidity levels above the deliquescent point.

In 2010, Joubert et al. investigated the influence of humidity on the pressure drop of flat and pleated HEPA filters clogged by polydisperse hygroscopic and non-hygroscopic aerosols [59]. Joubert et al. report that for hygroscopic aerosols at humidity level below deliquescent point or for non-hygroscopic aerosols, the specific cake resistance of the aerosol decreases as relative humidity increases.

Mullins et al. conducted experiments on bounce behavior of solid and liquid particles upon impact on dry filters and filters coated with water [60]. Mullins et al. used three different types of filters with various efficiency ratings to filter monodisperse stream of solid and fluid particles. The difference in efficiency of similarly-sized fluid and solid particles is then attributed to the fraction of particles that have bounced off the filter fibers. In their work, Mullins et al. have observed that the liquid particles dissipate the energy involved in the impaction process better than the solid counterparts. They have also shown that this effect is significantly reduced when the filter fibers are coated with water, concluding that increased humidity levels, directly reduces the fraction of particles that would bounce off the fiber otherwise.

In 2011, Chen et al. quantified the effect of humidity on the impaction of nanoparticles on coated and uncoated substrates [61]. They observed that decreasing relative humidity increased particle bounce from uncoated surfaces. Chen et al. used silicone-grease-coated aluminum foil, uncoated aluminum foil, and uncoated Teflon as substrates with relative humidity levels ranging from 10% to 90%. They concluded that the bounce behavior of $PM_{0.1}$ and $PM_{2.5}$ does not change significantly at relative humidity levels of 65%-80% and 75%-80% when uncoated Teflon and uncoated aluminum foil were used respectively.

Winkler performed a thorough study of the effect of relative humidity on particle bounce [62]. Through his research on polydisperse atmospheric aerosols, he concluded that if the relative humidity is higher than 75% atmospheric aerosols can be collected on a substrate surface upon impaction. He further observed that at relative humidties lower than 75% water-soluble aerosols were collected at much higher efficiencies than their non-soluble counterparts.

Stein et al. researched the effect of relative humidity on particle bounce using an inertial impactor [63]. They sampled atmospheric particles in Meadview, AZ and Minneapolis, MN. Focusing their study on 0.25 μm atmospheric aerosols, Stein et al. measured particle bounce using an uncoated aluminum substrate under controlled relative humidity conditions. They discovered that particle bounce increased significantly when relative humidity decreased below 60%-70% and little bounce took place at relative humidity levels above 70% -80%. Stein divided the effect of humidity on particle bounce into three categories: effect of humidity on the size of the particle, effect of humidity on the density of the particle, and effect of humidity on particle bounce. They used the model proposed by Zhang et al. for determining the change in the size of particles and change in the particle density under different relative humidity levels based on their constituents [64]. Stein et al. measured the fraction of particle bounce for the abovementioned particles under various relative humidity levels. Figure 14 and Figure 15 show Stein et al.'s measurements of particle bounce in Meadview and Minneapolis.

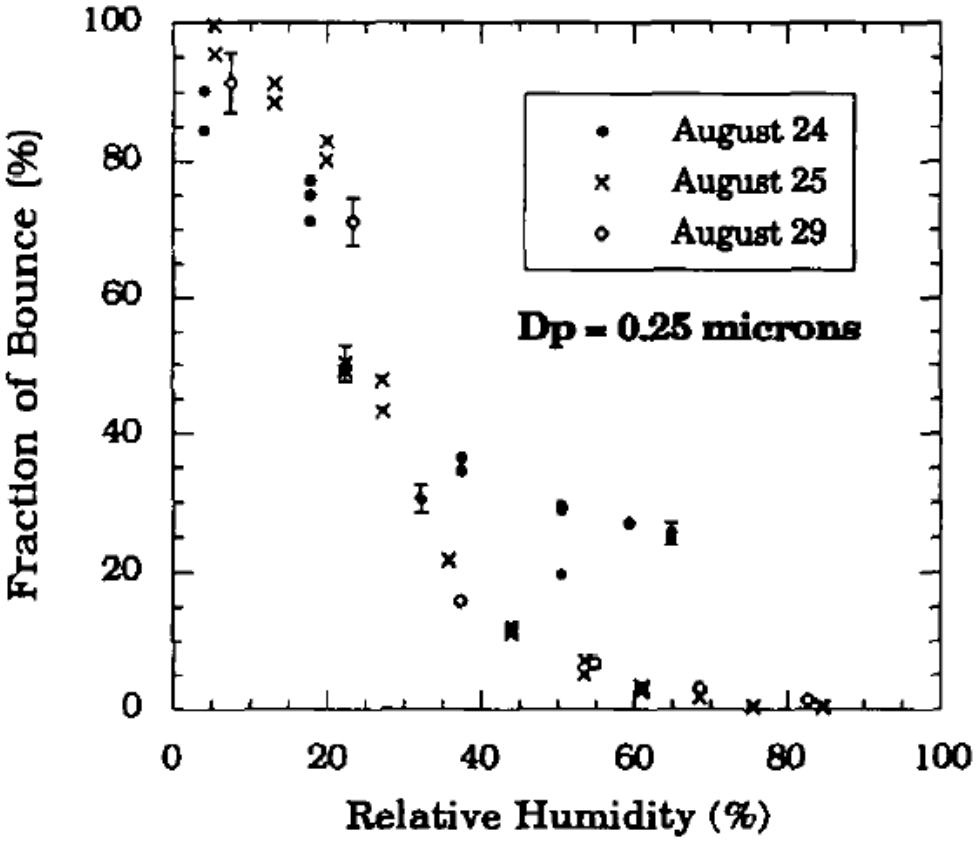

Figure 14 : Measurement of particle bounce vs relative humidity for atmospheric particles in Meadview, AZ [63]

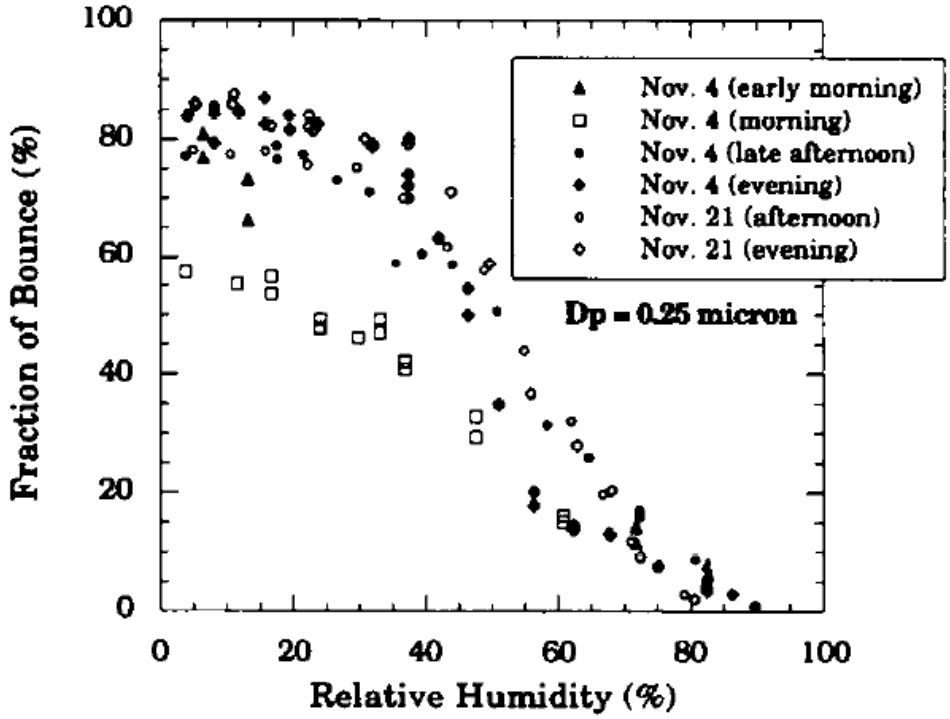

Figure 15 : Measurement of particle bounce vs relative humidity foe atmospheric particles in Minneapolis, MN [63]

Stein et al. observed that as the relative humidity increases, there is significantly less particle bounce off the surface of the aluminum impactor. They also observed that the fraction of bounce does not significantly change as the surface of the impactor is loaded with atmospheric particles.

2.3 Gap in Literature

The significance tests have revealed that sulfur dioxide, carbon monoxide, nitrogen dioxide, and ammonia levels in the studied regions do not have substantial effect on the performance of a PEM fuel cell. However, particulate matter in the air potentially imposes a risk to the operation of fuel cells, and their effect has not been studied in the past nor has a benchmark been established. The effect of particulate matter is expected to be intertwined with the relative humidity levels in fuel cell cathode gas stream due to effect of relative humidity on particle size, density and bounce behavior, a phenomenon that is yet to be studied. Having identified this gap in the literature, this thesis undertakes a numerical approach to understand the interaction of particulate matter and the GDL in PEM fuel cells better. The focus of this thesis, is to model the interaction of particles and the porous media in the fuel cell, namely the GDL, using principles of particle filtration while also taking into account the effect of humidity.

2.4 Outline of Approach

This study is divided into five sections, each progressively enhancing the model to arrive at a comprehensive model of flow of particles through the gas diffusion layer. Section 3 explains development of a single fiber model without particles. Section 4 introduces particles into the flow. Section 5 extends the single-fiber model with particles to a multi-fiber model with particles and discusses validation of results. Section 6 shows the development of a humidity model for flow of particles through fibers and draws conclusions about the validity of the model. The last section applies the humidity model to the model of a gas diffusion layer and provides an analysis of the effect of humidity on particle capture in the gas diffusion layer.

3 Single Fiber Without Particles

3.1 Background

It is of utmost importance to have a sound model of the flow around the fibers for reliability of the solution as more features are added to the model. The goal in this section is to first identify a simple representation of the fiber upon which more complicated aspects of the problem could be constructed. Then, the solution of the simple model can be validated with previously published results and used as a foundation for the rest of the model

Many researchers have investigated filtration process through theoretical and experimental analysis. In 1959, Happel investigated a system of regular staggered array of cylinders, shown in Figure 16, and derived the following equation for dimensionless drag [65]:

$$F^* = \frac{F}{U_0}\mu = 4\pi\left[-\frac{1}{2}\ln\alpha - 0.5 + \frac{\alpha^2}{2}(1+\alpha^2)\right]^{-1} \tag{3}$$

In 1959, Kuwabara derived a similar dimensionless drag force using slightly different boundary conditions [43]:

$$F^* = \frac{F}{U_0}\mu = 4\pi\left[-\frac{1}{2}\ln\alpha - 0.75 + \alpha - \frac{\alpha^2}{4}\right]^{-1} \tag{4}$$

α is the fiber volume fraction, F is the drag force, F^* is the non-dimensional drag force, U_0 is the fluid velocity in horizontal direction, and μ is the dynamic viscosity.

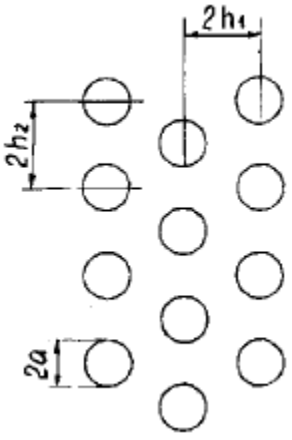

Figure 16 : Staggered arrangement of cylinders [66]

In the same year, Hasimoto derived the following equation for drag force for a regular square arrangement of cylinders as shown in Figure 17 [67]:

$$F^* = \frac{F}{U_0}\mu = 4\pi\left[-\ln\frac{\alpha}{2h} - 1.3105 + \pi\left(\frac{\alpha}{2h}\right)^2 + O\left(\frac{\alpha}{2h}\right)^4\right]^{-1} \tag{5}$$

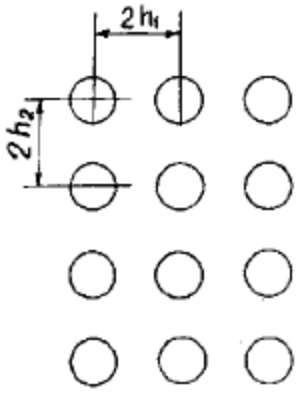

Figure 17 : Rectangular arrangement of cylinders [66]

In 1957, Tamada and Fujikawa determined the drag force for an isolated row of parallel cylinders to be [68]:

$$F^* = \frac{F}{U_0}\mu = 4\pi\left[-\ln\frac{\alpha}{2h} - 1.33 + \frac{\pi^2}{3}\left(\frac{\alpha}{2h}\right)^2\right]^{-1} \tag{6}$$

In 1967, Kirsch and Fuchs adapted an experimental approach to validate the theoretical relations and determine their applicability [66]. They experimentally validated the good agreement of Kuwabara's cell model in low Reynolds numbers [69] thus promoting it as a benchmark. Kuwabara's cell model is based on the arrangement shown in Figure 18 and results in streamlines around fibers defined by Equations 7 and 8 [43].

$$\Psi = \frac{sin\theta}{2Y}\left(\frac{1}{r^*} - r^* + 2r^* lnr^*\right) \tag{7}$$

$$Y = -\frac{1}{2}ln\alpha - \frac{3}{4} + \alpha - \frac{\alpha^2}{4} \tag{8}$$

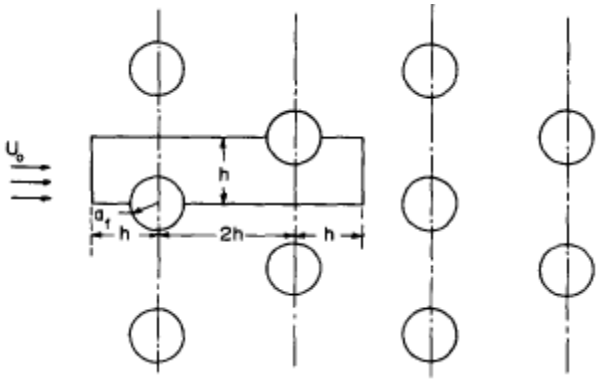

Figure 18 : Kuwabara's staggered cell model [70]

Kuwabara approached the flow field around the fibers by assuming a low Reynolds number and perfectly circular cylinders [43]. Furthermore, Kuwabara assumed that all fibers are perpendicular to the main flow direction and parallel to each other and they all have the same radius. The

underlying continuum assumption in the Navier Stokes equations used in Kuwabara's model is valid provided the mean free path of the molecules is less than the characteristic dimension of the flow domain. The validity of the continuum assumption is determined by the value of the Knudsen number shown in Equation 14. Using Kuwabara's cell model, Yeh and Liu [70] modified Kuwabra's assumptions to incorporate the effect of slip at the surface of the fibers and derived Equations 9 to 14.

$$\Psi = \frac{sin\theta}{2Y}\left(\frac{A}{r^*} + Br^* + 2r^* lnr^* - \frac{\alpha}{2}(r^*)^3\right) \tag{9}$$

$$A = \frac{\left(1 - \frac{1}{2}\alpha\right)\left(1 - Kn_f\right) + Kn_f\,\alpha}{1 + Kn_f} \tag{10}$$

$$B = \frac{(1-\alpha)\left(Kn_f - 1\right)}{(1 + Kn_f)} \tag{11}$$

$$r^* = \frac{2r}{d_f} \tag{12}$$

$$Y = -\frac{1}{2} ln\alpha - \frac{3}{4(1+Kn)} + \frac{\alpha}{1+Kn} + \frac{Kn(2\alpha - 1)^2}{4(1+Kn)} - \frac{\alpha^2}{4} \tag{13}$$

$$Kn_f = \frac{2\lambda}{d_f} \tag{14}$$

Despite the simplicity of the approach used by Yeh and Liu, their model is widely used as a benchmark for validation of more detailed models. The credibility of the model comes from its ability in predicting collection efficiency of filters.

The following will describe the approach towards creating a model of fibrous media based on Yeh and Liu's model by first looking at the flow field in the absence of particles.

3.2 Validation of No-Slip Flow in COMSOL

The numerical software chosen for this study is COMSOL 5.1. The reliability of the chosen software package is verified by simulating a relevant problem and comparing the results to well-established published results. The problem of no-slip flow over a two dimensional circular cylinder is deemed sufficient for validation purposes.

The phenomenon of flow past circular objects is one that has been studied extensively both experimentally [71] [72] [73] and numerically [74] [75] [76]. Flow of interest in this study is flow over a two dimensional circular cylinder which is a two dimensional case of flow over a sphere. However, there is no steady solution for the stokes equations for this two dimensional case, which is known as the Stokes paradox [77]. Oseen has approximated the solution for this particular flow by proposing addition of an ad hoc linearized convective acceleration to the momentum equation [78]. Nieuwstadt and Keller have presented a numerical solution to the Oseen approximation for Reynolds numbers from 1 to 40 [79]. Their results as well as experimental results from Coutanceau and Bouard [80] are used for validation of COMSOL.

3.2.1 Model Setup

The model setup in COMSOL is a simple case of flow over a circle. The model properties such as circle diameter, flow velocity, and fluid properties are obtained from the experimental work by Coutanceau and Bouard [80]. The experimental setup involves a small cylinder of diameter 10 mm moving vertically through a viscous oil with viscosity of 0.0269 $kg\,m^{-1}s^{-1}$ and density of 847 $kg\,m^{-3}$. The cylinder, with a camera attached to it as shown in Figure 19, is moved through a tank of oil with a constant speed using a hydraulic jack with measurements presented for when the flow is fully developed.

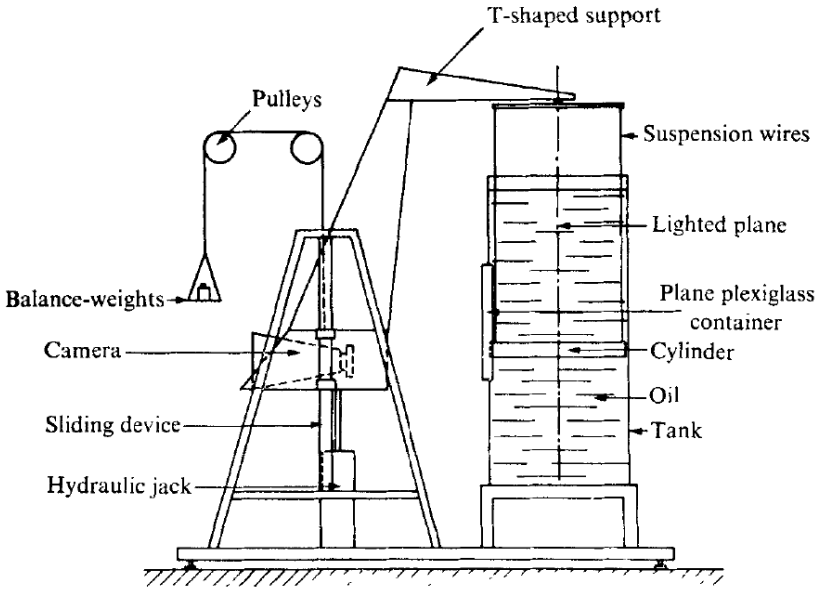

Figure 19 : Experimental setup of flow over cylinder [80]

The Reynolds number for this experiment is 20 and the result of interest is the horizontal velocity profile downstream of the cylinder up to a distance of 5 radii away from the cylinder. The model setup is shown in Figure 20, the diameter of the circle is 0.01 m with fluid properties similar to the one used in the experiment. Reynolds number is 20 for this scenario resulting in an inlet fluid velocity of 0.0635 m/s calculated based on the diameter of the circle.

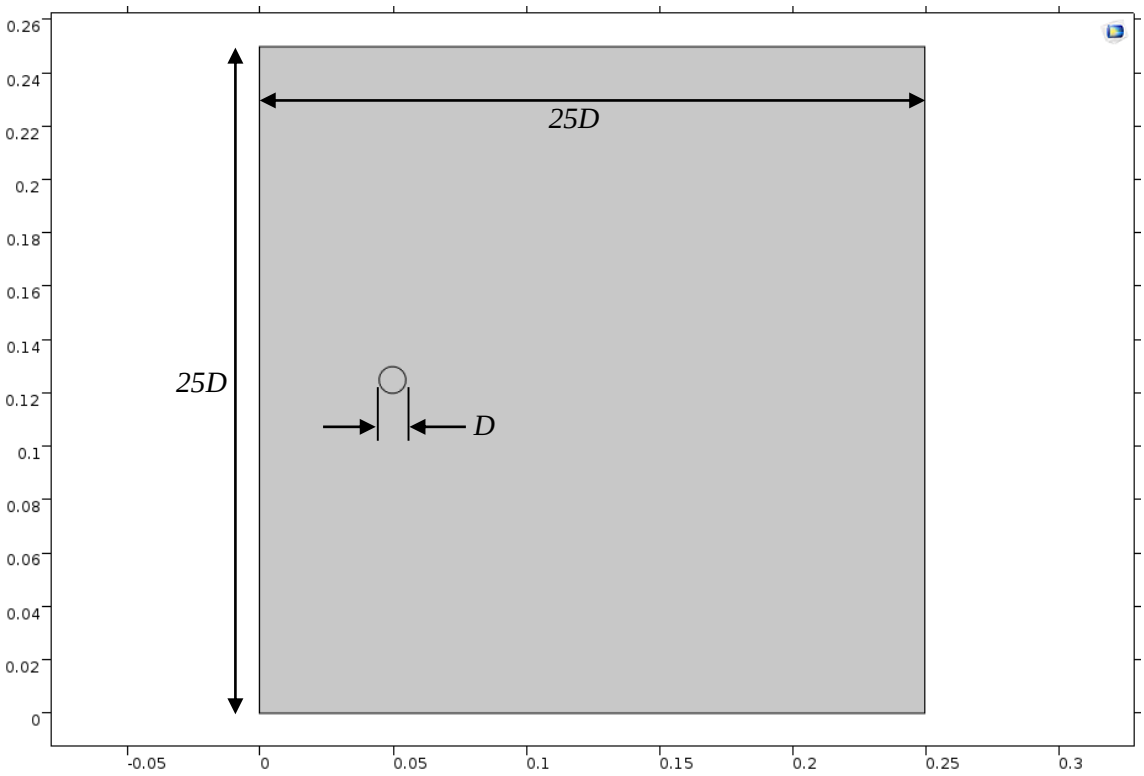

Figure 20 : Setup of the model of flow over circle (axes in m)

COMSOL utilizes an automatic mesh feature where a suitable mesh is applied to the model based on the physics of the model, in this case a steady state study of laminar flow over a circle. The mesh is shown in Figure 21. As shown in this figure, the mesh has much smaller elements in the vicinity of the circle which is the area of interest with progressively larger mesh elements away from the cylinder. Furthermore, thin boundary layer mesh is applied to the top and bottom walls as well as the surface of the circle to resolve the interactions due to no-slip boundary condition. The minimum and maximum element size in this mesh are 0.002 m and 6e-5 m respectively.

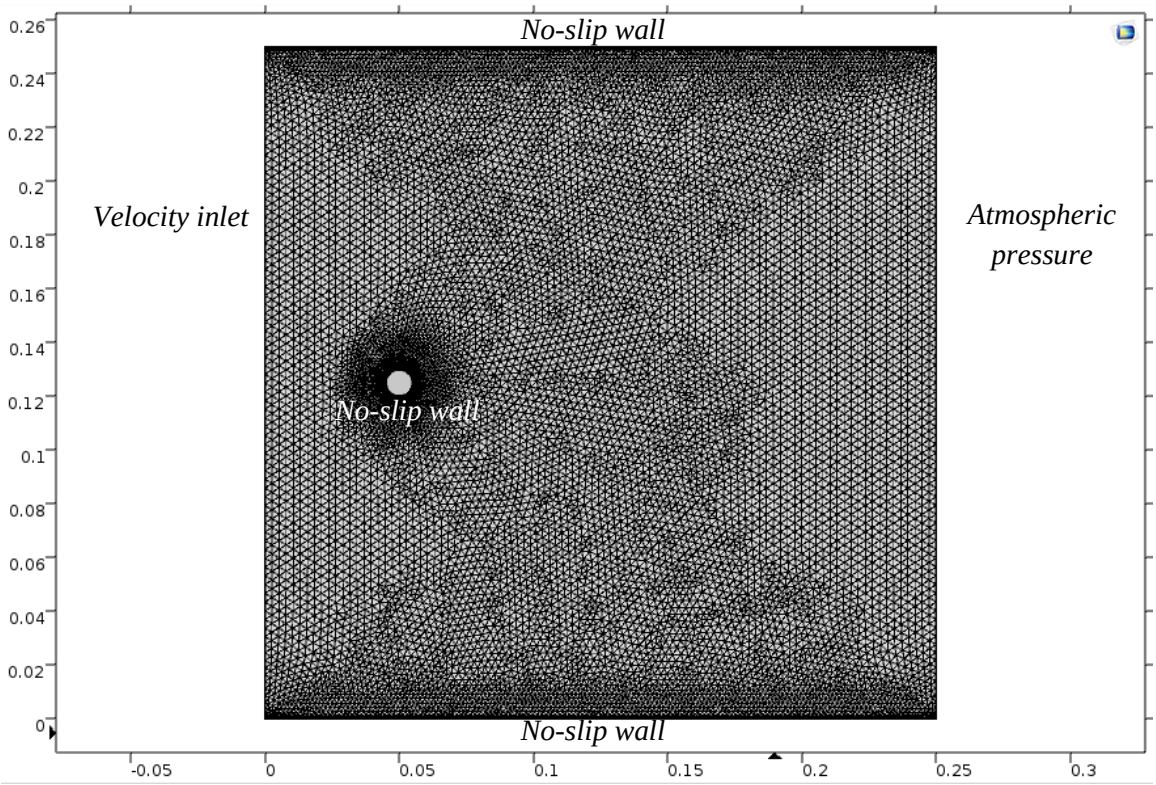

Figure 21 : Mesh for the model of flow over cylinder (axes in m)

The flow close to the surface of the circle is resolved using layers of rectangular mesh, also known as boundary layer mesh, as shown in Figure 22. Boundary layer mesh consists of layers of rectangular elements laid on top of each other, a practice in place for quite some time for fluid mechanics problems [81]. The triangular mesh elements are laid on top of the boundary layer mesh with smaller elements adjacent to the boundary layer mesh.

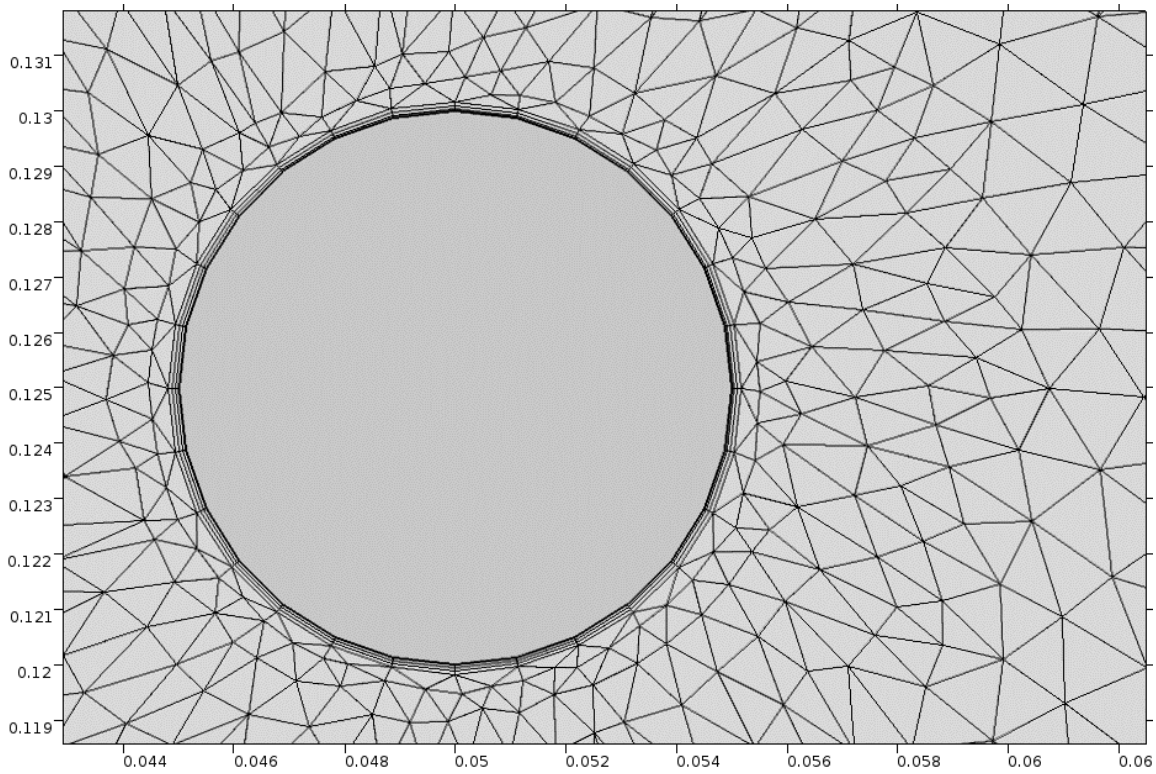

Figure 22 : Close-up view of the mesh near the 2D circle (axes in m)

The next section describes the governing equations and the formulation of the governing equations and the solver used for this problem.

3.2.2 Governing Equations

The model is solved assuming laminar, incompressible, steady and two-dimensional fluid model with uniform temperature. Navier Stokes continuity, x-momentum and y-momentum equations have been solved numerically to yield results as shown in Equations 15 to 17. The energy equation is not solved since temperature is assumed to be uniform in the entire domain.

$$\frac{\partial u}{\partial x} + \frac{\partial v}{\partial y} = 0 \tag{15}$$

$$\rho\left(u\frac{\partial u}{\partial x} + v\frac{\partial u}{\partial y}\right) = -\frac{\partial p}{\partial x} + \mu\left(\frac{\partial^2 u}{\partial x^2} + \frac{\partial^2 u}{\partial y^2}\right) \tag{16}$$

$$\rho(u\frac{\partial v}{\partial x} + v\frac{\partial v}{\partial y}) = -\frac{\partial p}{\partial x} + \mu(\frac{\partial^2 v}{\partial x^2} + \frac{\partial^2 v}{\partial y^2}) \tag{17}$$

Equation 15 is continuity equation and represents the conservation of mass and Equations 16 and 17 represent the conservation of momentum in x and y direction respectively. u and v are the velocity components in the x and y direction respectively. The flow is also assumed to be single-

phase and have a Reynolds number less that one, making it reasonable to assume creeping flow [82]. This means that the inertial terms on the left hand side of Equations 16 and 17 can be neglected and the viscous terms on the right hand side become dominant.

3.2.3 Boundary Conditions

The boundary conditions for the model are shown in Figure 21. Flow enters from the velocity inlet at a uniform velocity and exits through the pressure outlet with atmospheric pressure. The walls at the top and bottom as well as the surface of the circle are no-slip walls.

3.2.4 Solver Type and Termination Criteria

The following discusses the type of solver used for solving the model and the criteria used for terminating the numerical solution.

3.2.4.1 Solver Type

The solver for this problem is referred to as a stationary solver and it uses a damped Newton method for solving laminar flow. This nonlinear solver uses the discrete form $f(U) = 0$, where $f(U)$ is the residual vector and U is the solution vector. The solver starts with an initial guess U_0 and then solves the discretized form of the linearized model $f(U_0)\delta U = -f(U_0)$ for the Newton step δU using the selected linear system solver, where $f(U_0)$ is the Jacobian Matrix. The linear system solvers available for the damped Newton method are: multi-frontal massively parallel sparse direct solver (MUMPS), parallel sparse direct solver (PARDISO), sparse object oriented linear equations solver (SPOOLES), and dense matrix. Using MUMPS as the default solver, the solver then computes the new iteration $U_1 = U_0 + \lambda\delta U$, where λ is the damping factor between 0 and 1. Upon calculation of the new iteration, the error, E, for the new iteration is estimated by solving $f(U_0)E = -f(U_1)$. If the error is larger than the error in the previous iteration, the solver reduces the damping factor, λ and recalculates U_1. The damping factor reduction is repeated until the error for the current iteration is less than the error in the previous iteration. When a successful step is taken, the algorithm starts the next Newton iteration [83].

3.2.4.2 Termination Criterion

There are three types of termination criterion for the stationary solver: termination by solution, termination by residual, and termination by solution or residual. Each one is discussed in the following section.

3.2.4.2.1 Termination by Solution

For this criterion, the nonlinear iterations terminate when the relative tolerance is larger than the error for the current iteration computed as the weighted Euclidean norm, err, :

$$err = \sqrt{\frac{1}{M}}\sqrt{\sum_{j=1}^{M}\frac{1}{N_j}\sum_{i=1}^{N_j}\left(\frac{|E_{i,j}|}{W_{i,j}}\right)^2} \tag{18}$$

In this equation, M is the number of fields, N_j is the number of degrees of freedom in the field j, and $E_{i,j}$ refers to the error in the current iteration at degree of freedom i and field component j. The

field components in this study are pressure, horizontal velocity, and vertical velocity. $W_{i,j}$ is defined as

$$W_{i,j} = \max(|U_{i,j}|, S_j) \tag{19}$$

where S_j is a scale factor which is set to zero in this study and $U_{i,j}$ is the solution at degree of freedom i and field j.

3.2.4.2.2 Termination by Residual

The criterion for termination by residual is as follows : the solver stops the iterations when the error calculated as the weighted Euclidean norm, err, is less than the relative tolerance.

$$err = \sqrt{\frac{1}{M}} \sqrt{\sum_{j=1}^{M} \frac{1}{N_j \widetilde{W}_j^2} \sum_{i=1}^{N_j} \left(|F_{i,j}|\right)^2} \tag{20}$$

F is the current residual and $\widetilde{W}$ are the weights determined by the first and, if applicable, the second residual. The subscript i refers to the degree of freedom index and subscript j refers to the field component.

3.2.4.2.3 Termination by solution or residual

For this termination criterion, the solver stops when the relative tolerance is larger than relative error calculated as the minimum of the solution based error and the error given by the residual factor multiplied by the residual-based error.

The termination criterion used for this study is termination by solution with scaling of error set to none in order to observe the absolute error. Furthermore, the convergence criterion is based on a user-defined tolerance which is set to 1e-7 for this study, meaning that once the absolute error falls below the tolerance, the model is assumed to have converged. The tolerance value of 1e-7 is sufficiently stringent to ensure convergence and yet not too small therefore avoiding long simulation time.

3.2.5 Results and Discussion

Figure 23 shows the velocity field and streamlines of the solution. The straight line immediately downstream of the circle is where horizontal velocity measurements are made in order to be compared to experimental and theoretical results. As expected, the flow is stationary near the top and bottom walls and at the walls of the circle. The maximum and minimum horizontal velocity values are 0.0798 $m\,s^{-1}$ and -2.20e-3 $m\,s^{-1}$ respectively. The negative sign for the minimum velocity value is indicative of reverse flow which happens downstream of the circle as revealed in the results shown in Figure 24.

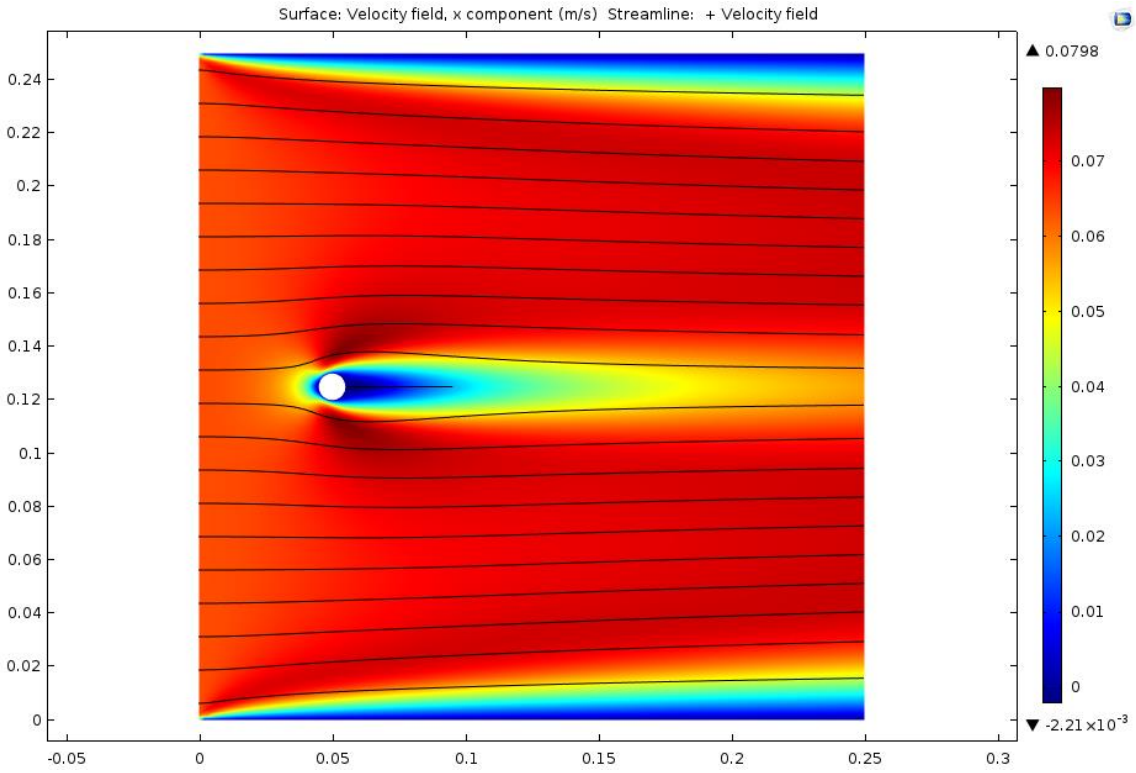

Figure 23 : Velocity field and streamlines for the model of flow over cylinder (axes in m)

Figure 24 shows the results of the numerical simulation model compared to the theoretical and experimental work of Nieuwstadt [79] and Coutanceau [80]. There is a very good agreement between the numerical and both the experimental and theoretical results. Immediately downstream of the circle, there is adverse flow, indicated by horizontal velocity with negative value, followed by horozintal velocity in the direction of the flow upstream of the circle.

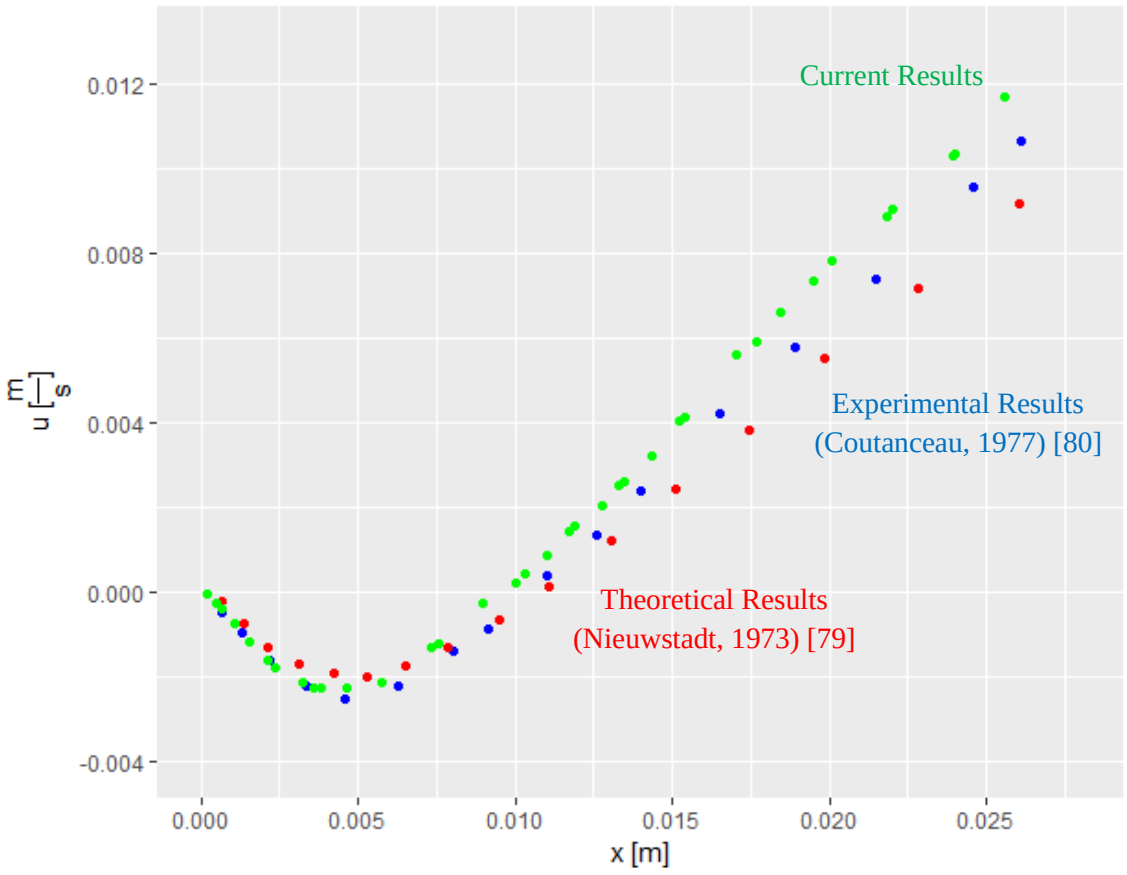

Figure 24 : Comparison of theoretical, experimental, and numerical results of flow over circle

In addition to the velocity profile, the drag coefficient of the circle from the simulation is also compared to other published work as shown in Table 6. The drag coefficient is calculated based on Equation 21.

$$C_D = \frac{2F_w}{\rho U^2 D} \tag{21}$$

F_w is the horizontal force acting on the surface of the circle, ρ is the density of the fluid, U is the velocity of the fluid, and D is the diameter of the circle.

Table 6 : Drag coefficient for the model of flow over circle

Researcher	**Drag Coefficient Reported**
Jayaweera (1965) [84]	2.16
Tritton (1959) [85]	2.03
Nishioka (1974) [86]	1.95
Present work	2.14

It is observed that the drag coefficint calcualted by COMSOL is within the range of drag coefficients cited in benchmark papers with a tendency towards the higher end of the range. The results of this simulation are used as a sanity check to validate the performance of the solver. Had the software failed in this stage, it would not have been suitable for carrying on to the next stages of the study. The next section discusses slip flow boundary condition in COMSOL.

3.3 Validation of Slip Flow in COMSOL

3.3.1 Flow around a 2D Cylinder

The first stage in modeling the GDL is solving the flow field through fibrous. One of the complexities in doing so is modeling the random structure of fibers in the media. The randomness is due to the manufacturing process of fibrous media where layers of fibers are laid on top of each other without any particular pattern. While the fiber configuration is random, the diameter of the fibers can be controlled. Therefore, flow around a two dimensional circular cylinder is considered first.

It is decided to develop a model with low Reynolds number in order to simplify the Navier Stokes equation and also to avoid complexities associated with analysis of turbulence. This is especially important in the early stages of the study as these results are compared with results from the literature which mainly focus on flows with low Reynolds number. This is due to the fact that fibrous media studies fin the literature mostly focus on filtration applications and when it comes to filters, performance is found to be independent of Reynolds number at low Reynolds numbers.

Figure 25, shows the effect of Reynolds number on the dimensionless drag force, F by Wang et al. [87]. The dimensionless drag force is defined as:

$$F = \frac{\Delta P \pi d_f^2}{4 \alpha \mu u Z} \tag{22}$$

Similar to the equations developed by Kuwabara, Happel, and Hasimoto, Equations 3, 4, and 5, Wang's equation is also independent of Reynolds number. This is illustrated graphically in Figure 25 by the straight line corresponding to the models from Kuwabara and Hasimoto. Later on, Liu and Wang found that the drag force on multi-fiber filters remains almost unchanged for Re<1.0 and increases with Re when Re>1.0 as shown in Figure 25 [88]. Liu and Wang's finding has been validated by Wang et al. using a Lattice-Boltzman two-phase flow model [87]. It is decided to use a flow with Reynolds number of 0.1 in this study.

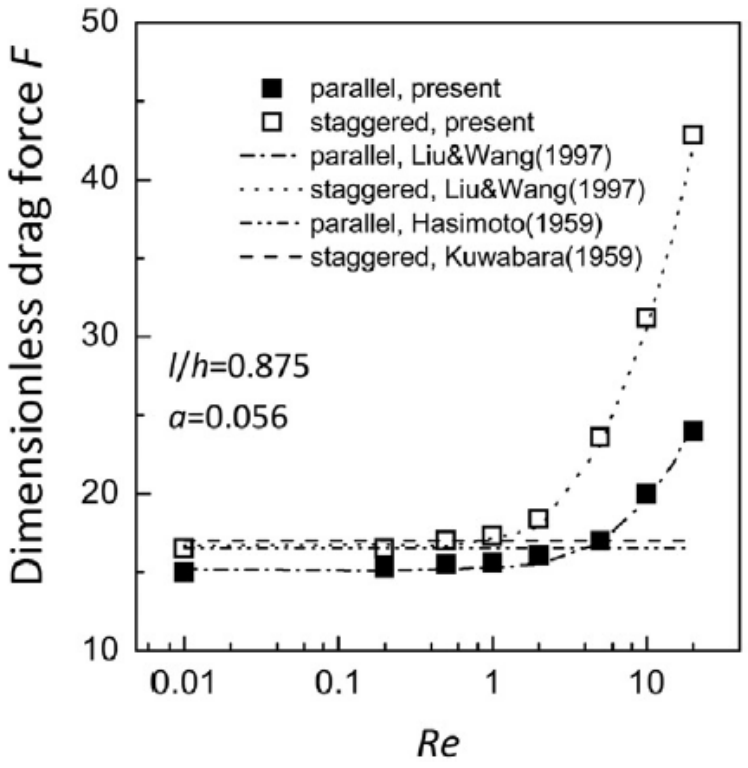

Figure 25 : Dimensionless drag force versus Re [87]

Before discussing the model further, it is important to take into account the phenomenon of slip. Slip becomes important when the characteristic length of the model becomes relatively small hence comparable to the free mean path of the fluid. Measured by the Knudsen number, shown in Equation 14, importance of slip can be shown by determining the degree of rarefaction within the fluid. Flow is considered to be in the continuum regime when Kn <<1 and as Kn approaches 1 the flow becomes slip flow. When Kn>>1 the flow is called free molecule or kinetic regime [89]. Given the continuous nature of this transition, it is challenging to set exact thresholds however the following is suggested [90] :

Navier Stokes equations with no-slip boundary conditions:	$\mathrm{Kn} \leq 10^{-3}$
Navier Stokes equations with slip boundary conditions:	$10^{-3} \leq \mathrm{Kn} \leq 10^{-1}$
Transition regime	$10^{-1} \leq \mathrm{Kn} \leq 10$
Free Molecule Flow	$Kn > 10$

With the thresholds for different flow regimes established, the most important geometrical property of the fiber, namely the diameter of the fiber, is determined next. The diameter of the fiber is the geometrical length the free mean path of the fluid is compared to by means of calculating the Knudsen number. Based on the value for this number, the flow regime and the appropriate boundary condition on the surface of the fiber is determined.

The diameter of fiber used in manufacturing various types of fibrous media varies based on application and manufacturing process. Fibrous media have been studied experimentally by many researchers, some researchers have considered only single fibers for their experimental work as summarized in Table 7 :

Table 7 : Range of fiber diameters used in the literature

Researcher	Fiber Diameter [μm]
Yeh and Liu (1974) [91]	11.2
Myojo et al. (1984) [92]	11-70
Thomas et al. (2001) [93]	370
Song et al. (2006) [94]	100
Kasper et al. (2010) [95]	8 and 30

Fiber diameters larger than 100 μm are deemed too large and diameters smaller than 10 μm are considered too small and fairly rare. The range of diameters between 10 μm and 100 μm are further analyzed to determine the flow regime. At 100 μm and 10 μm, the Knudesn number is calculated to be 1.32e-3 and 1.32e-2 respectively. The Knudsen number for a fiber diameter of 100 μm is on the border of slip and non-slip regime based on the criteria mentioned above, however, a fiber with diameter of 10 μm is in the slip flow regime. For the sake of thoroughness in analysis, a fiber diameter of 10 μm is chosen for this study.

The flow around the fiber is in the slip regime and slip boundary condition needs to be applied to the boundary of the fibers. First, an understanding of slip flow needs to be established. The following section illustrates this concept.

3.3.2 Slip Flow

Assuming a fluid flowing in a tube, the fluid molecules constantly strike and reflect from the solid inner wall of the tube. In a hypothetical case, it can be assumed that the inner surface of the tube is perfectly smooth meaning that the particles reflect off of the surface at the same angle that they approached the surface prior to reflection, similar to the rays from a mirror. In this case the molecules' tangential momentum is conserved and no shear is exerted on the wall of the tube. This type of reflection is termed specular reflection and results in perfect slip flow at the walls of the tube. However, this case is an unrealistic scenario because there is no such thing as perfectly smooth surface and even the most polished surfaces appear rough. The other possibility is that the incident particles reflect at a random angle uncorrelated with the incidence angle, this case is termed diffuse reflection [78]. In the case of diffuse reflection, the lack of complete transfer of tangential momentum to the reflected fluid particle is balanced by a slip velocity to accommodate shear transmitted to the wall.

The slip flow model in this study is based on the works of Maxwell [96]. Maxwell's slip flow boundary condition considered a monatomic hard sphere gas and required Boltzmann equation [96], however, the boundary condition can also be used in Navier Stokes equations [97]. Equation 23 shows the calculation of slip velocity required for application of slip flow boundary condition :

$$u_{slip} = \frac{G}{\mu}\left(\tau n - \left((n^T \tau n)n\right)\right) + \frac{3}{4}\frac{\mu}{\rho T_g}[\nabla - n(n \cdot \nabla)][T_g - \frac{8}{3}G\left(n \cdot \nabla T_g\right)] \quad (23)$$

$$G = \frac{2-\sigma}{\sigma}\lambda \quad (24)$$

$$\sigma = \frac{\tau_i - \tau_r}{\tau_i - \tau_w} \quad (25)$$

u_{slip} is the slip velocity, n is the boundary normal, τ is the viscous stress tensor, μ is the gas viscosity, ρ is the gas density, and $T_g$is the gas temperature. In Equation 24, σ is the tangential momentum accommodation coefficient and λ is the mean free path. In Equation 25, τ_i is the tangential momentum of incoming gas molecules, τ_r is the tangential momentum of the reflected gas molecules, and τ_w is the tangential momentum of the remitted molecules ($\tau_w = 0$ for stationary surfaces.)

Equation 26 shows the equation for the viscous stress tensor based on the definition of the strain-rate tensor shown in Equation 27:

$$\tau = 2\mu S - \frac{2}{3}\mu(\nabla \cdot u)I \quad (26)$$

$$S = \frac{1}{2}(\nabla u + (\nabla u)^T) \quad (27)$$

In Equation 23, the left-hand term represents viscous slip and the right-hand term shows thermal slip. In this formulation, the temperature of the wall is assumed to be constant and equal to the temperature of the gas.

Slip velocity is generally not important at high Reynolds numbers as the flow near the wall is turbulent, but it becomes more important in flows with low Reynolds number which is the case with the model under study [78].

COMSOL provides the option to apply slip flow boundary condition based on Maxwell's model, and since slip is considered an important aspect of this study, it is decided to validate the slip boundary condition provided by COMSOL using an analytical solution [98].

3.3.3 Slip flow Boundary Condition Validation

The model, shown in Figure 26, is a simple rectangular domain where air enters from the left at 2.27 m/s and exits from the right. The dimensions of the model are in micrometers which reflect the small scale of the geometry compared to the velocity of air passing through it. Using the distance between the top and bottom wall, 3.3 μm, as the characteristic length in the model the Knudsen's number is calculated to be 0.02 which is in the slip flow regime, making the problem ideal for

validation of COMSOL slip boundary condition feature. Figure 26 also shows the velocity field as well as streamlines calculated for the domain of the problem. The goal here is to compare the solution calculated by COMSOL to the analytical solution by Barber et al. [98] and validate COMSOL's slip boundary condition.

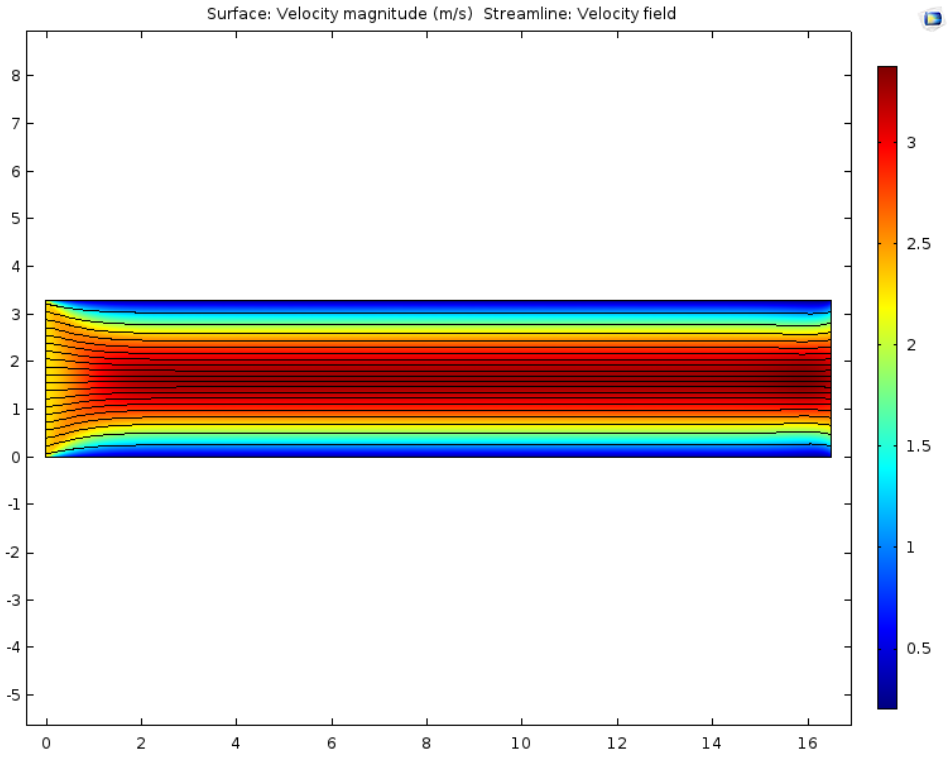

Figure 26 : Domain and solution of the model for slip boundary condition validation (axes in µm)

The comparison of the results is shown in Figure 27. Two cases have been considered for this comparison : $kn = 0.10$ and $kn = 0.01$ where the height of the channel is the varying parameter. As expected, with a larger Knudsen's number the phenomenon of slip has a larger effect as seen by the difference between the non-dimensional velocity at the walls for the two Knudsen's numbers.

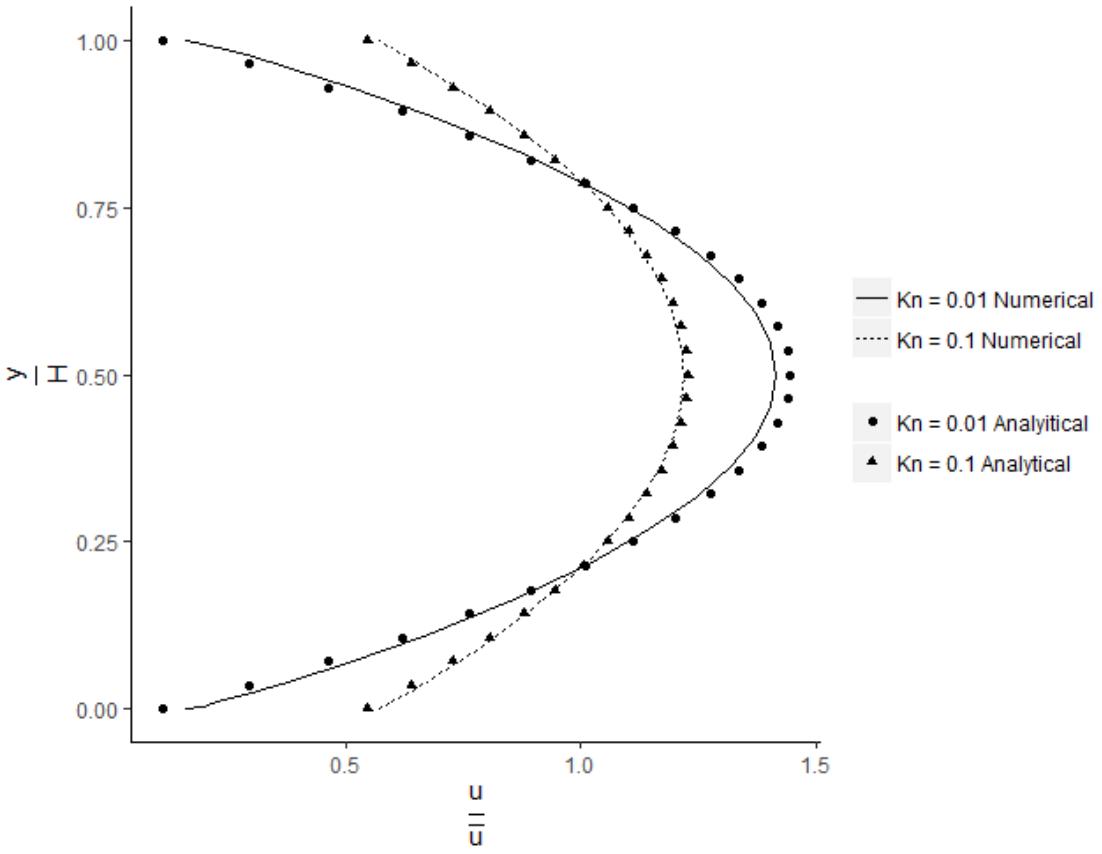

Figure 27 : Velocity profile at the exit of the channel - numerical and analytical

The numerical and analytical velocity profiles show very close agreement which means that the slip-flow feature in COMSOL is proven to be an accurate representation of Maxwell's slip model. This feature is used in the next stages of the simulation. The next step in setting up the single fiber model is the flow field around a single fiber.

3.4 Flow Field Around Single Fiber

With assurance of the functionality of the slip boundary condition, the staggered model presented by Yeh et al. [70] is used as the basis for establishing the fundamental element of the model : a single fiber. Validation of results in this stage of the study paves the way for expanding the model to include particles in the flow and consequently flow around multiple fibers. This section describes the single fiber model characteristics followed by comparison of numerical results with analytical results.

3.4.1 Model Setup

The geometry of the model is similar to the staggered model presented by Yeh et al. with a fiber diameter of 10 µm. The selection of fiber size is explained in section 3.3.1. Figure 28 shows the geometry of the.

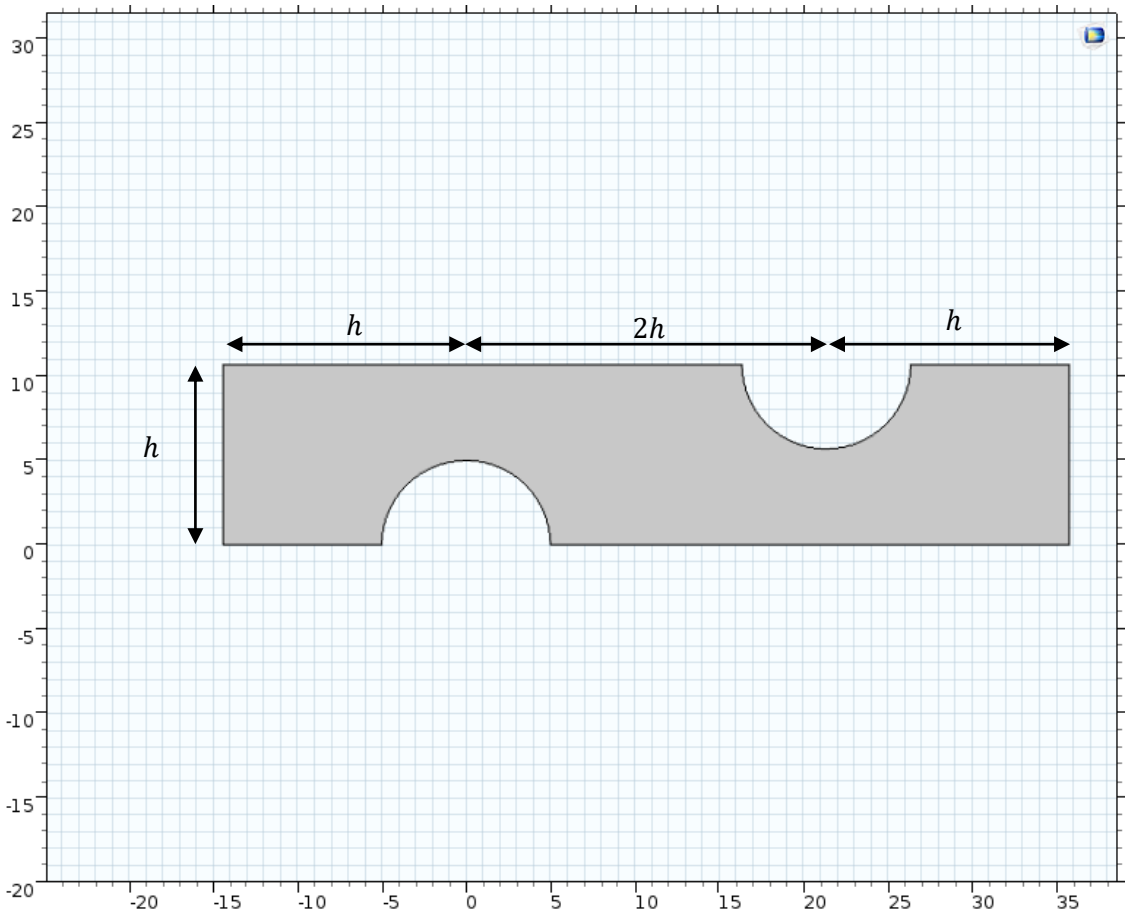

Figure 28 : Geometry of the single fiber model (axes in µm)

The parameter h , is defined as the height of the domain and the width of the domain is $4h$ to ensure consistency with Yeh's staggered model. The parameter h is calculated based on the fiber volume fraction of the filter (α). Fiber volume fraction refers to the fraction of the control volume that is occupied by volume of the fibers and is equal to one minus the porosity of the control volume, as shown in Equation 28:

$$\alpha = 1 - porosity = \frac{\pi d_f^2}{16h^2} \tag{28}$$

Porosity of fibrous media determines the proximity of fibers. In a theoretical scenario where fibers are stacked on each other in an orderly fashion, different porosity levels affect the flow field around the fibers. In real-life fibrous media where the fibers are randomly placed on top of each other, the effect of porosity is as significant however the relationship is not as easy to understand as it is in the theoretical scenario with orderly arranged fibers. This study focuses on the theoretical arrangement of fibers.

Common porosity values for fibrous media range from 10% to 20% depending on the application of the fibrous media.

Table 8 shows some of the common porosity values used in fibrous filter research.

Table 8 : Common porosity values for fibrous filters

Researcher	Porosity Reported
Zhao et al. (2016) [99]	80-90%
Wang et al. (2013) [87]	82.8 %
Martins et al. (2016) [100]	86-93%
Jackierwicz et al. (2015) [101]	91.3%

Porosity value of 82.8% is used for the current study, in agreement with the work of Wang et al. to facilitate further comparison of results. Equation 28 is solved for h assuming a fiber volume fraction of 17.2% and resulted in value of 10.68 µm.

The mesh of the solution domain is selected based on a mesh convergence study discussed in Section 3.4.4.1. It consists of triangular elements with a minimum element size and maximum element size of 0.00427 and 0.299 µm respectively. The elements adjacent to the fiber are rectangular becoming progressively thinner towards the surface of the fiber as shown in Figure 29. This configuration allows for better resolving of the fluid near the surface of the fiber.

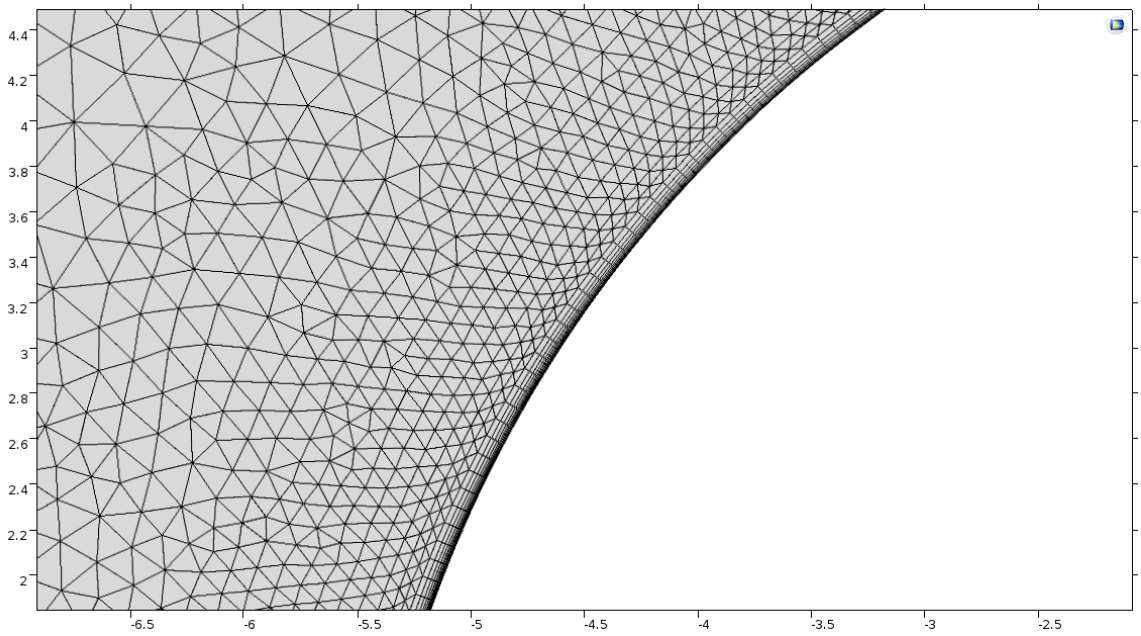

Figure 29 : Close-up view of the mesh near the surface of the fiber

3.4.2 Governing Equations

Governing equations for the flow are similar to the ones mentioned in Section 3.2.2: conservation of mass and momentum in 2D.

3.4.3 Boundary Conditions

The flow considered in this study is a steady laminar flow with Reynolds number less than 1. The fluid is standard air and the inlet velocity is uniform with a magnitude of 0.1 $m\,s^{-1}$ resulting in a Reynolds number of 0.068 as shown in Equation 29 :

$$Re = \frac{\rho u d_f}{\mu} = 0.068 \tag{29}$$

As discussed in Section 3.3.1, slip velocity becomes important at low Reynolds numbers, therefore a slip boundary condition is applied to the surface of the fibers in the model as illustrated in Figure 30. The tangential momentum accommodation coefficient, σ, is 0.99 based on a study that is discussed in Section 3.4.4.2.

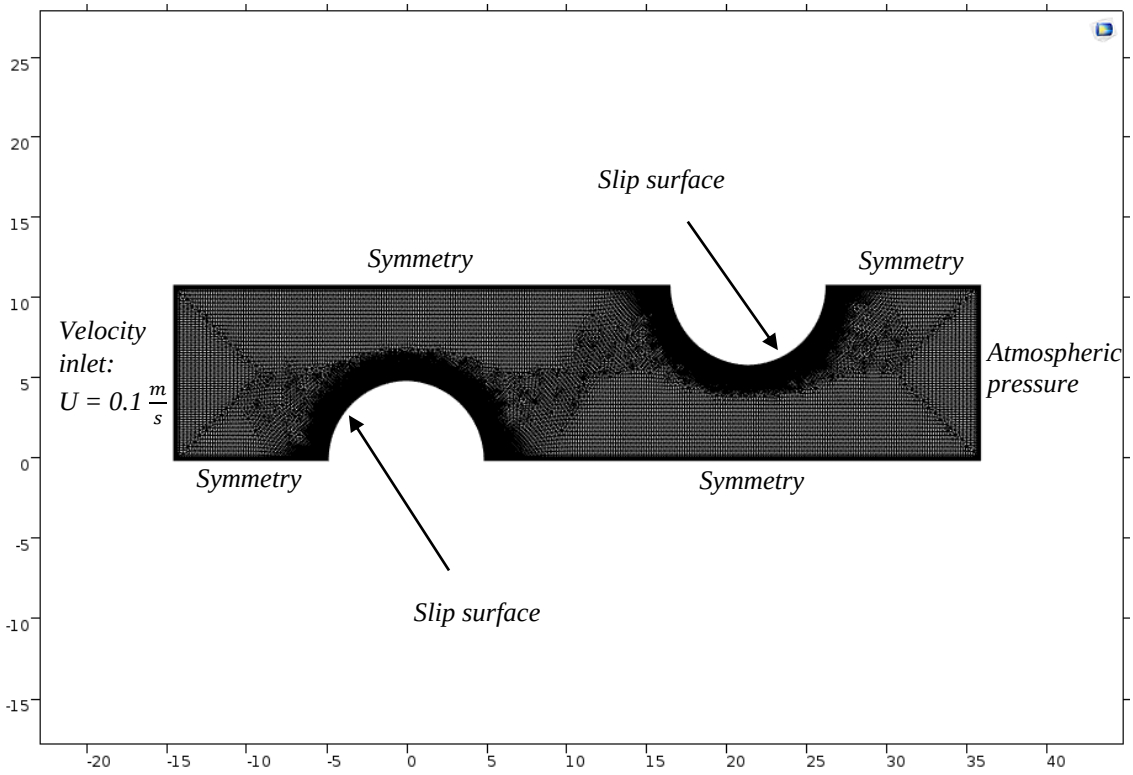

Figure 30 : Boundary conditions of the single fiber model without particles (axes in µm)

The symmetry boundary condition is used to represent the array of fibers that are assumed to be located above and below the solution domain, shown in Figure 30.

3.4.4 Results and Discussion

The flow field around the single fiber is the main topic of interest for validation of results. One of the most important modeling parameters that is expected to influence the results is the fineness of the mesh. A very fine mesh is computationally expensive when it comes to calculations and a very coarse mesh may not resolve the features of the flow. Therefore, a mesh analysis is required to balance the trade-off.

The slip boundary condition used in this study uses a key parameter: the tangential momentum accommodation coefficient hereafter referred to as slip coefficient. However, there is no reliable data reported in the literature for applications similar to the one in this study. Therefore, a separate analysis is conducted on the effect of the slip coefficient on the results of the model and a value is selected accordingly. Based on the comparison between the current work and the analytical results presented by Yeh et al. [91] a reasonable mesh and an appropriate value for the slip coefficient has been selected.

3.4.4.1 Mesh Study

Two meshes are considered for the mesh study: a coarse mesh and a fine mesh referred to as mesh 1 and mesh 2 respectively. Mesh 1 has a minimum element size 0.02 μm and a total of 5400 triangular elements and 800 quadrilateral elements. The quadrilateral elements are used in the construction of the boundary layer mesh near the surface of the fibers. Mesh 2 has a minimum element size of 0.004 μm and a total of 25000 triangular and 2200 quadrilateral elements. These meshes are shown in Figure 31 and Figure 32.

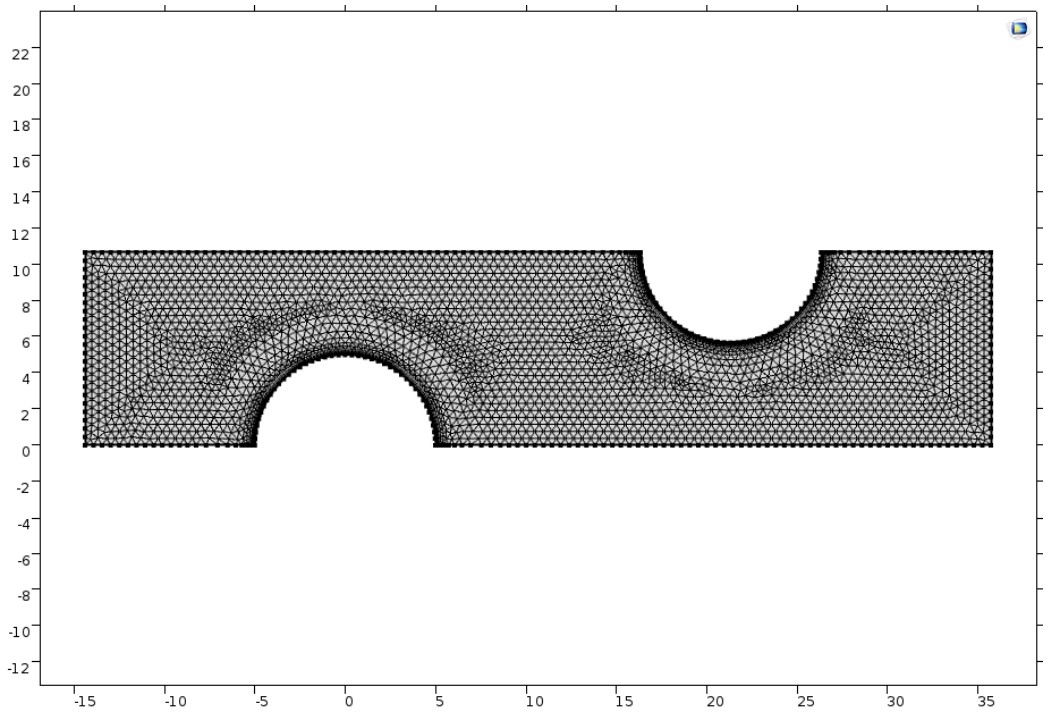

Figure 31 : Coarse mesh for solving flow over single fiber (mesh 1)

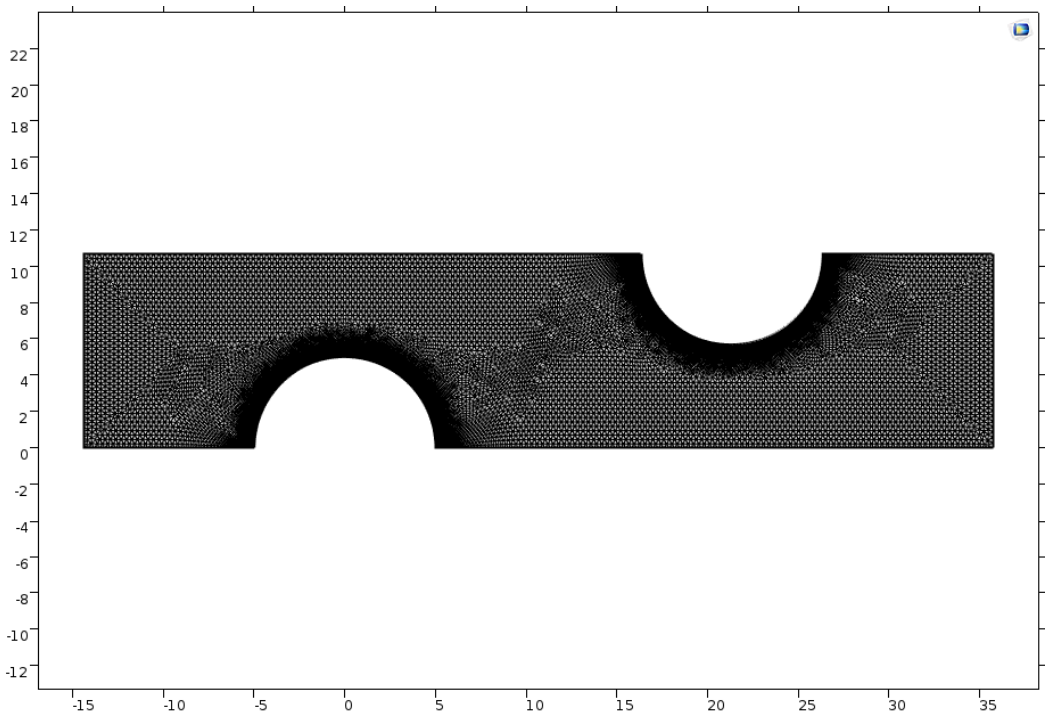

Figure 32 : Fine mesh for solving flow over single fiber (mesh 2)

The results obtained by solving the model using each of the meshes is compared to the analytical results of Yeh et al. as shown in Figure 33. It is noteworthy that both the x and y axis are normalized by the diameter of the fiber and only three streamlines are shown, one that is very close to the surface of the fiber, and two that are progressively further away from the fiber. The two meshes have resulted in almost identical streamlines which show reasonable agreement with the streamlines obtained analytically. As the benefit of a finer mesh is not noticeable based on this analysis, mesh 1, the coarser mesh, is chosen for proceeding to the next stages of the study.

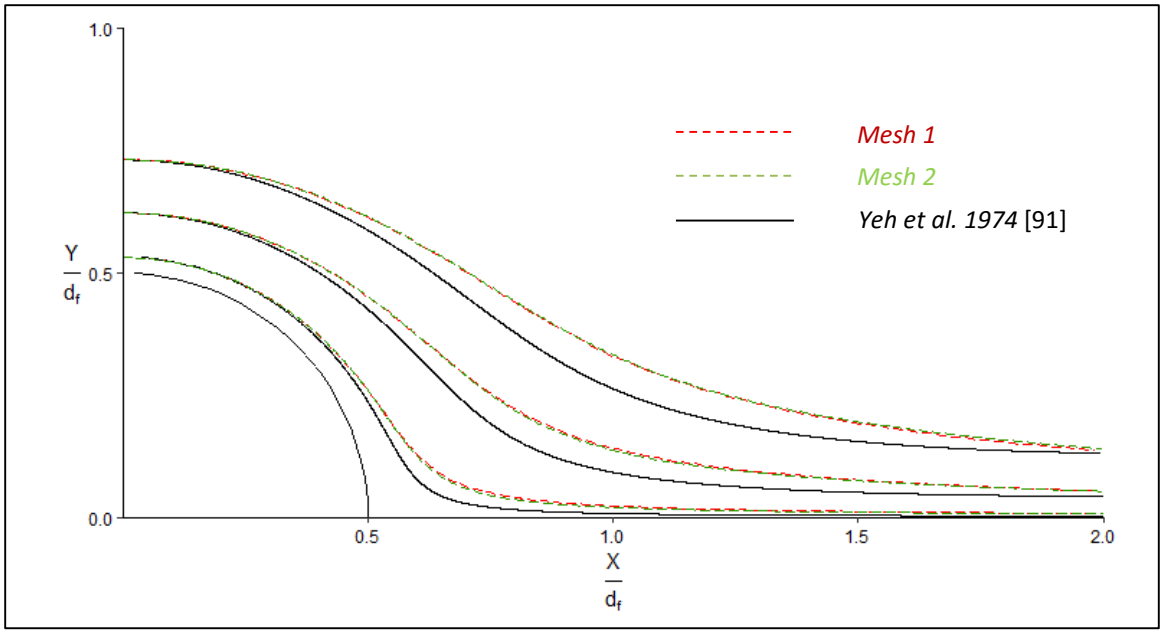

Figure 33 : Comparison of results of mesh study and analytical results

3.4.4.2 Slip Coefficient Study

With the mesh analysis yielding the appropriate mesh to be used for the rest of the study, an analysis is conducted on three values for the slip coefficient. The results are compared with the analytical solution as shown in Figure 34. It is observed that as the slip coefficient increases the streamlines from the numerical solution align more closely with the analytical solution with a slip coefficient of 0.99 resulting in the best alignment. The value for the slip coefficient for the study is therefore determined to be 0.99.

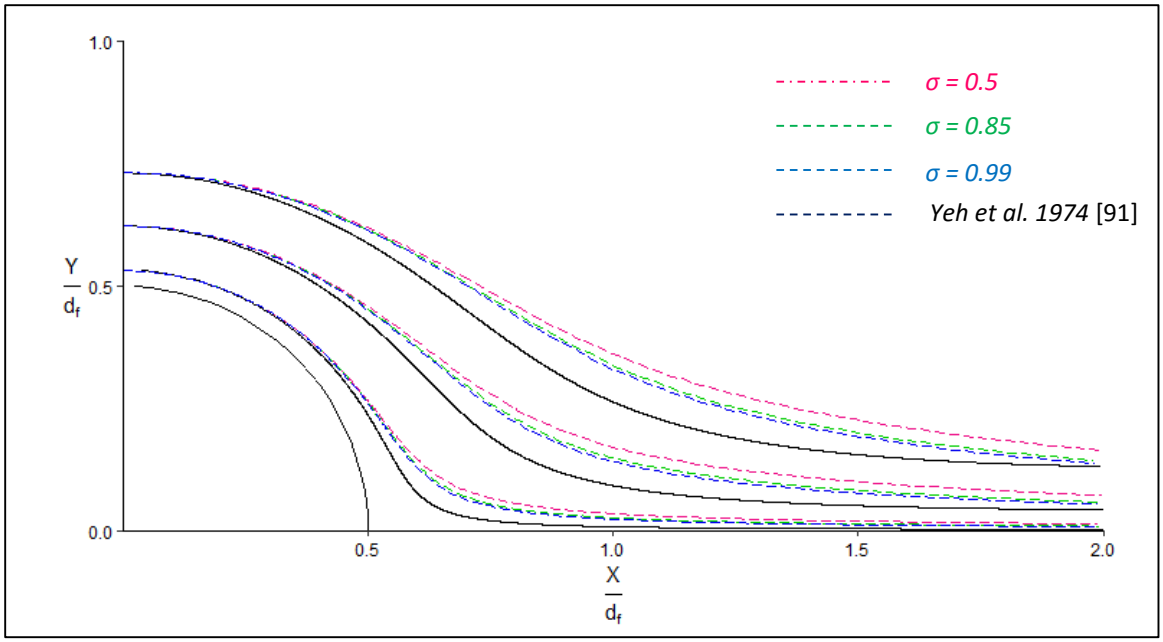

Figure 34 : Comparison of different tangential momentum accommodation coefficients with analytical results

The resulting flow field of the model with the appropriate mesh and slip coefficient is shown in Figure 35. The streamlines of the numerical model show a reasonable agreement with the analytical model.

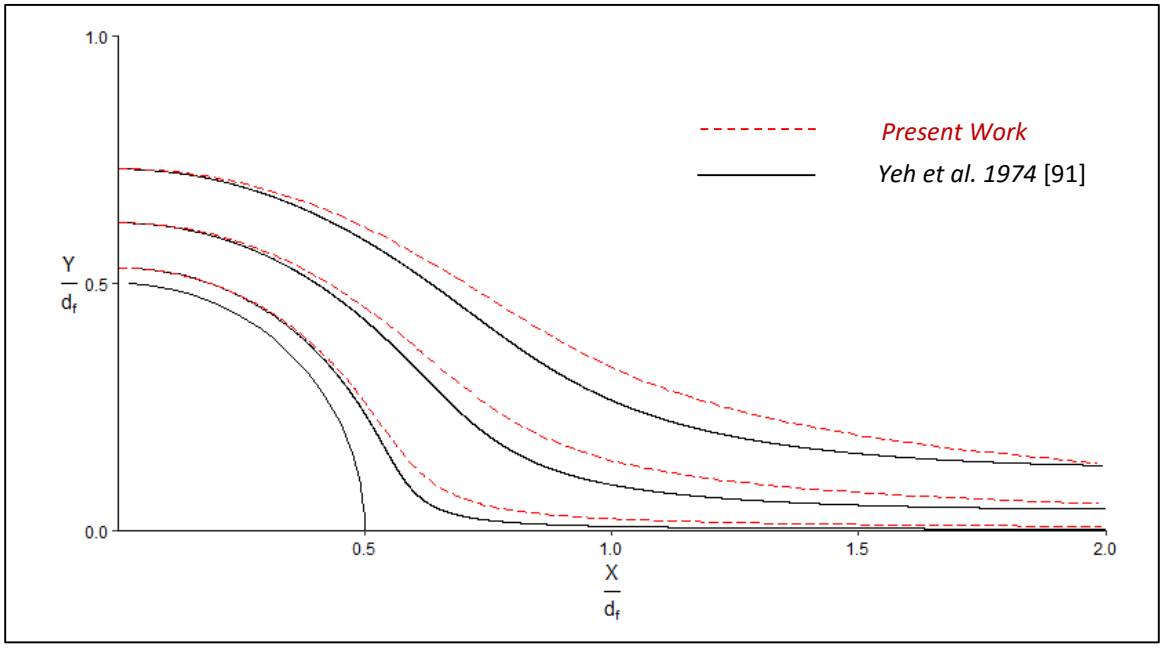

Figure 35 : Comparison of the numerical and analytical solutions for single fiber flow field

In the next stages of the study as particles are added to the flow, the interaction of the particles with the surface of the fibers is much more important than the flow of particles past the fibers where no capturing of the particles is expected.

3.5 Summary

Single fiber model without particles was studied in this section of the study. First, two-dimensional flow around a no-slip circle was solved and the solution provided by the solver was verified. Then, the slip-flow feat of COMSOL was validated against an analytical solution for flow in a thin channel. At this stage, the solver was validated and paving the way for solving flow around a single-fiber. A mesh study and a slip coefficient study were undertaken to find the correct setup of the model: a slip coefficient of 0.99 was deemed suitable. The next section of the study focuses on adding particles to the flow solution around a single fiber.

4 Single Fiber with Particles

There are many different types of microscopic particles floating in the air: suspended soil particles, salt particles formed from ocean spray, smoke from power generation, rubber from tire wear and water droplets or ice particles. All such particles are categorized as aerosols defined as the large number of small particles suspended in the air around us [102]. Understanding of the properties of the aerosols and their interaction with mechanical systems, such as the GDL in fuel cells is of great practical importance.

Aerosols are present in air in different compositions and forms. In tropical regions where there is high frequency of precipitation, there is a high concentration of water droplets in the air. In the vicinity of sand deserts there is a high concentration of fine sand particles in the air and with the slightest blow of wind, the concentrations of these aerosols would change dramatically given their miniscule size. The study of properties, behavior and physical principles of aerosols and the knowledge pertaining to their measurement and control is known as Aerosol technology [103]. Given the broad scope of aerosol technology, this study aims to use specific aspects of aerosol technology with some simplifications. This section will explain the approach towards adding particles to the flow field. The setup of the model, various studies on the model, parameter selection, assumptions, and results are presented in the sections to follow.

4.1 Particle Dynamics and Capture Mechanisms

The ultimate application of this study is a fuel cell powered vehicle, which realistically is exposed to different types and concentrations of particles throughout its lifecycle. A one-solution-for-all is the ideal goal. The approach towards this goal is breaking the problem into simpler ones and adding details in stages to arrive at a comprehensive model. Therefore, the scope of this study is limited to monodisperse particles : particles with geometric standard deviation of less than 1.25 [104], in fact, the particles introduced to the flow are all of similar size and density. While this assumption is not realistic, it is extremely useful in developing an understanding of the dynamics of the particles and the overall trends.

Aerosols in ambient air have many different shapes, sometimes even hardly similar within the same class of particles. One of the most common types of aerosols are soot particles which appear as the byproduct of incomplete combustion of hydrogen, carbon monoxide, and hydrocarbons [105]. Soot particles are known to have open and chainlike shape with chains sometimes extending to few hundred micrometers [106] [107] [108]. Mineral dust particles have non-spherical and highly irregular shapes due to the irregular growth of the crystals on nucleation sites [109]. The irregularities in shape of particles is a major obstacle in the study of particle capture. The approach taken in this study is to assume spherical shape for all particles introduced to the flow for simplicity. This assumption allows for calculation of drag forces using conventional drag over sphere calculations which are much less computationally expensive than calculation of drag force over otherwise irregular shapes.

It is important to note that in realistic conditions, the particles that are present in the air, or in the case of this study, enter the fuel cell, collide with each other. Depending on the condition of the flow, such collisions could result in sticking of the particles together and forming larger particles,

breaking of the particles into smaller ones, or some form of deflection based on the material properties of the particles. For example, as discussed in the humidity model section, Section 6, as the humidity level increases, particles tend to become sticky and form larger agglomerates. One of the assumptions made about particles in this study is that they are rigid and they do not interact with each other. This assumption is reasonable when the particles are charge-free. If the charge on the surface of particles is taken into account, then the assumption of absence of inter-particle interactions fails. This model assumes neutral charge for all particles.

There are four mechanisms through which a neutral particle can deposit on a neutral fiber : interception, inertial impaction, Brownian diffusion, and gravitational settling [110]. Interception occurs when the particle travels along a streamline that comes closer than one radius of the particle to the surface of the fiber. This mode of deposition is particularly important when particles do not have high inertial forces and as a result do not deviate from the streamline [111]. Inertial impaction happens when the particles traveling along the streamline, due to their high inertial forces and a sudden change in flow direction near the fiber, collide with the fiber and are captured. This mode of capture is common with particles of high density and large size. Brownian diffusion refers to the diffusion of the particles away towards the surface of the fiber due to their Brownian diffusion. This form of capture becomes dominant when the particle size and mass is small and with the increase in the temperature of the particle, the Brownian diffusion becomes more intense. Gravitational settling takes place when a particle falls on a fiber, usually when the flow speed is very low. This mode of capture is neglected in flows with high speed, such as the flow in this study.

For a single fiber, collection efficiency is defined as the ratio of particles captured by the fiber, to the total number of particles. In order to have a better understanding of the capture mechanisms, the efficiency for each mechanism as well as the overall efficiency for the single fiber can be calculated. This will help determine which mode of particle capture is the dominant in this study. The following calculations are based on the model presented by Yeh et. al [70].

For the cell model presented by Yeh et. al , the single fiber efficiency due to inertial impaction per unit length of the fiber, η_{ip}, can be calculated as :

$$\eta_{ip} = \left(\frac{Stk_m}{2Y}\right) I \tag{30}$$

$$Stk_m = \frac{Stk}{2Y} \tag{31}$$

$$Stk = \frac{\rho_p d_p^2 C_c U_0}{18\mu d_f} \tag{32}$$

$$Y = -\frac{1}{2} ln\alpha - \frac{3}{4} + \alpha - \frac{\alpha^2}{4} \tag{33}$$

$$I = \begin{cases} (29.6 - 28\alpha^{0.62})R^2 - 27.5R^{2.8} & \text{For R} < 0.4 \\ 2 & \text{For R} \geq 0.4 \end{cases} \quad (34)$$

Stk_m is the modified Stokes number, R is the interception parameter, and C_c is the Cunningham correction factor for particles to account for slip and is determined by Equation suggested by Allen and Raabe [112]:

$$C_c = 1 + Kn[1.142 + 0.558 \exp\left(-\frac{0.999}{Kn}\right)] \quad (35)$$

The single fiber efficiency due to Brownian diffusion, η_D, is calculated as :

$$\eta_D = \frac{3.65\ (Pe_m)^{-\frac{2}{3}} + 0.624(Pe_m)^{-1}}{2Y} \quad (36)$$

$$Pe_m = \frac{Pe}{2Y} \quad (37)$$

$$Pe = \frac{U_0 d_f}{D_p} \quad (38)$$

$$D_p = \frac{kTC_c}{3\pi\mu d_p} \quad (39)$$

k is the Boltzmann constant with the value of $1.38 \times 10^{-23}\ m^2 kg\ s^{-2} K^{-1}$. Pe_m is the modified Peclet number, it shows the effect of convective transport over diffusive transport of particles.

The single fiber efficiency due to interception, η_{it}, is determined as :

$$\eta_{it} = \frac{1+R}{2Y}[2\ln(1+R) - (1-\alpha) + \left(1 - \frac{\alpha}{2}\right)(1+R)^{-2} - \frac{\alpha}{2}(1+R)^2] \quad (40)$$

With efficiency of each individual capture mechanism known, the total efficiency of a single fiber can be determined by adding the efficiencies up. Figure 36 shows the efficiencies due to different mechanisms of capture as well as the total single fiber efficiency for a range of particle diameters. The efficiency values in this figure are calculated based on a porosity value of 81.8% with a fiber diameter of 10 μm, particle density of 2000 $kg\ m^{-3}$, and air as the particle carrying fluid. The total efficiency of a single fiber is dominated by the Brownian diffusion mechanism for particles diameters of 0.1 μm and smaller. However, interception and inertial impaction are the dominant mechanisms for particle sizes of about 2 μm and larger. In the particle diameter range of 0.1 μm to 2 μm, the total efficiency is a combination of the three mechanisms.

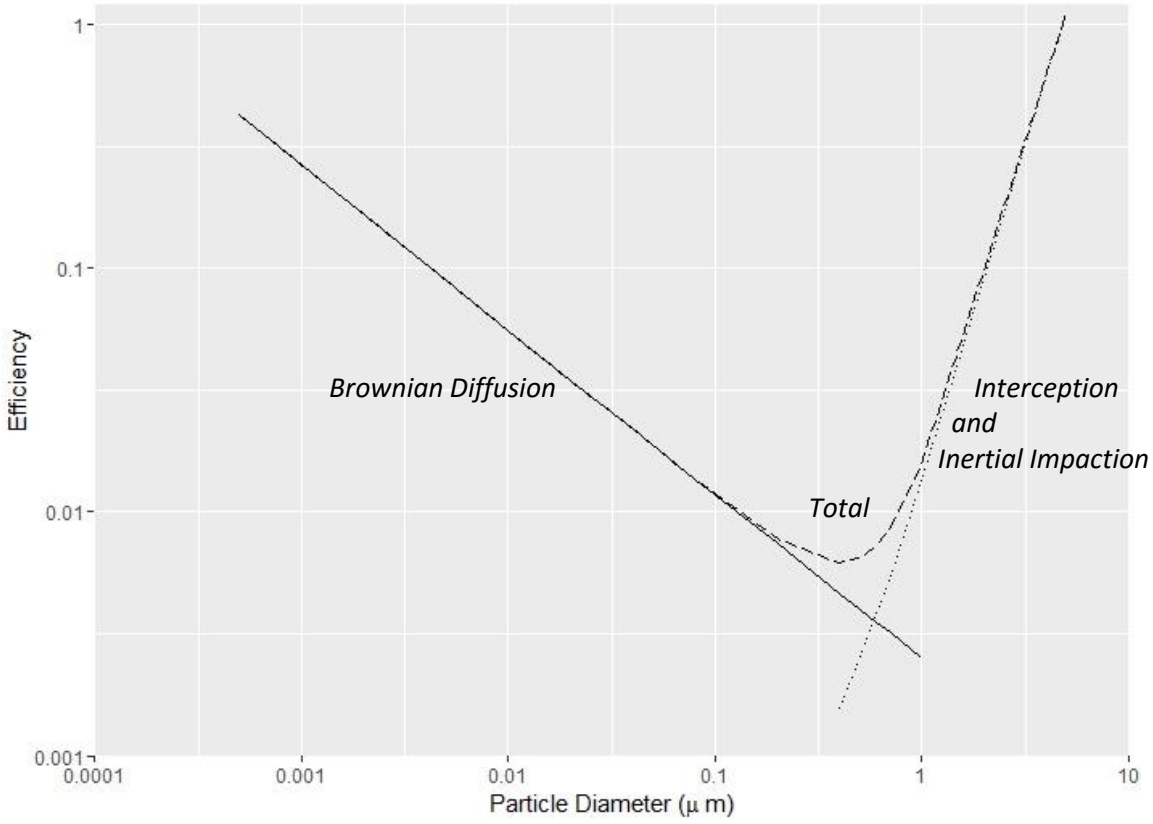

Figure 36 : Theoretical particle capture efficiency of single fiber

High efficiency particulate air (HEPA) filters are one of the most common filters in removing aerosols. HEPA filters are standardized to have a minimum particle collection efficiency of 99.97% on particles of size 0.3 µm [113] [114]. Assuming a HEPA filter upstream of air that enters the cathode of a fuel cell, it is very important to study the smaller particles that make it through a HEPA filter. Therefore, for this study, the size of the particles is assumed to be 0.1 µm. Based on Figure 36, the dominant mechanism of particle capture for 0.1 µm particles is Brownian diffusion, therefore this mode must be accounted for in the model. The interception and inertial impaction modes of capture are not expected to play a significant role in this size range.

Another important assumption in this study is the assumption of clean fibers. In the current stage of the study where a single fiber is considered, and in the next stages of the study where multiple fibers are present, it is assumed that the fibers have not been exposed to particles previously. This means that particles are only expected to collide with fiber surface, and not with particles previously deposited on the fibers. This assumption simplifies the modeling requirements significantly. First of all, if the structure of the particles and their interaction with each other were to be considered, a coupled fluid-solid model would have to be solved which requires numerical approaches that are beyond the scope of this study including: dynamic mesh, advanced convergence handling, and very large computation times to mention a few. However, with the assumption of clean fibers, a one-way modeling approach can be implemented as shown in the following section.

4.2 Approach to Modeling

There are two options for modeling particles in the flow. First option is to model the particles as rigid solids with a defined volume and set up a coupled fluid-solid model. The coupled model would communicate the results of the fluid model and the motion of the solid model to each other in each iteration continuously. In such a model, the particle and the flow mutually affect the solution. The main advantage of this option is the high accuracy of the solution due to the realistic assumptions. However, such a model would require large computations time. Furthermore, given the two-dimensional nature of this study, it is impractical to introduce three-dimensional particles to the flow. This option would be very useful for particle sizes that are in the same order of magnitude as the size of the fiber, however, in the current study, the size of the particles is 0.1 μm which is 100 times smaller than the size of the fiber. Therefore, the increased accuracy achieved by this approach is deemed marginal.

The second option is to assume particles are small enough that they do not affect the flow and therefore, the solution for the flow around the fiber and the motion of the particles can be solved separately. While the solution of the flow around the model can be solved using a steady state assumption, the solution of the particle motion must be solved assuming a transient model where the position of the particle is solved at each time step. If the particles are small enough, the solution of the flow can be calculated separately, and then applied to the particles for calculating their motion. The main advantage of this approach is the quick computation time however, this comes at the cost of lower accuracy. Furthermore, this option does not require three-dimensional modeling of the particles and is achievable with the two-dimensional scope of the study. Given that the particles in this study are 100 times smaller than the size of the fiber, this option is deemed reasonable and the following section describes the implementation of this approach.

4.3 Model Setup

The geometry of the model is similar to the geometry used for flow without particles, shown in Figure 28. As discussed in the previous section, particles are added to the solution of the flow around the fiber calculated in Section 3.

4.4 Governing Equations

As mentioned before, the approach to this model is to apply the solution of the flow around fiber to the particles in order to determine their motion through the fluid. Therefore, for brevity the governing equations for the flow around the fiber are not repeated here as they can be found in Section 3.2.2.

Momentum of the particle is determined based on Newton's second law : net force on a particle equals the particle's time rate of change of its linear momentum in an inertial reference frame [83] :

$$\frac{d}{dt}\left(m_p u_{particle}\right) = F_D + F_g + F_{ext} \tag{41}$$

where F_D is the drag force, F_g is the force due to gravity, and F_{ext} is any external forces such as electric forces. Drag force is defined as:

$$F_D = \left(\frac{1}{\tau_p}\right) m_p (u_{fluid} - u_{particle}) \tag{42}$$

where m_p is the particle mass, and τ_p is the particle velocity response time in seconds. The particle response time for spherical particles in a laminar flow is defined as:

$$\tau_p = \frac{\rho_p d_p^2}{18\mu} \tag{43}$$

Equations 42 and 43 are also known as Stokes drag law. This law is valid for particles with low Reynolds number and also assumes that the surrounding fluid is a continuous medium [115].

The gravity force is defined as:

$$F_g = m_p g \frac{\rho_p - \rho}{\rho_p} \tag{44}$$

Where ρ is the density of the surrounding fluid , air in this case and g is the gravity vector.

As mentioned in Section 4.1, Brownian diffusion mechanism is expected to be the dominant mode of particle capture in this problem therefore Brownian force is the only contributor to F_{ext}. The contribution is defined as:

$$F_{ext} = \zeta \sqrt{\frac{6\pi k \mu T d_p}{\Delta t}} \tag{45}$$

where ζ is a normally distributed random number with a mean of zero and a unit standard deviation, k is the Boltzmann constant with the value of $1.38 \times 10^{-23}\ m^2 kg\ s^{-2} K^{-1}$, T is the absolute fluid temperature, d_p is the particle diameter, Δt is the time step taken by the solver. A new random number is generated at each time step for each component of the Brownian force [83].

4.5 Boundary Conditions

Figure 37 shows the particle-related boundary conditions applied to the walls of the solution domain. Particles are released from the particle inlet and as they travel through the domain, they would either pass through certain walls of the domain or stick to the walls representing the fibers. All the particles that make it without passing through walls or getting stuck on the surface of the fiber are then captured at the right hand side of the solution domain for counting purposes. The release of the particles can be modeled to happen continuously on specified time steps or can be released all at once. For this study, the particles are released all at once.

It is noteworthy that upon sticking to the surface of the fiber, the particles are removed from the domain of the solution. This means that there is the possibility that more than one particles collide with the same fiber at the same location on the surface of the fiber. While this is not the case in reality, it is very rare to have two particles hit the fiber at the exact same location given the much smaller size of the particles relative to the fiber.

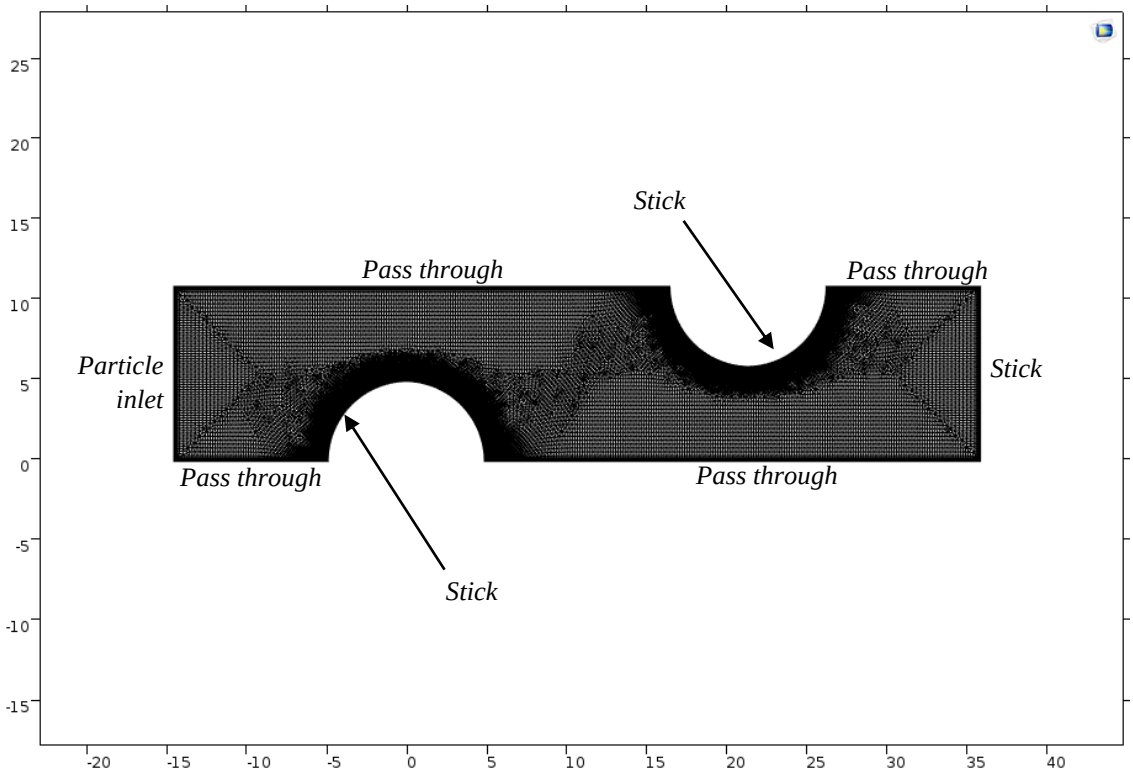

Figure 37 : Boundary conditions of single fiber with particles (axes in µm)

The particles introduced to the model are perfectly spherical with a diameter of 0.1 µm. The particles in this study are assumed to have an equal amount of ammonium sulfate ($\rho = 1780\ kg\ m^{-3}$), ammonium nitrate ($\rho = 1730\ kg\ m^{-3}$), elemental carbon ($\rho = 2000\ kg\ m^{-3}$), and soil dust ($\rho = 2300\ kg\ m^{-3}$) [63] resulting in an overall density of 2000 $kg\ m^{-3}$.

The following section describes the governing equations used for solving the motion of the particles.

4.6 Solver Type and Convergence Criteria

The time-dependent solver is used when the field variables of interest change over time, or in other words, for problems that are transient in nature [83]. The method for the time-dependent solver is Generalized-α which is an implicit, second order accurate solver with a parameter for controlling numerical damping. This method was first developed for second-order equations in structural mechanics [116] and extended to first order problems later [117].

This method updates the variables of interest at each time step. The solver can be controlled for settings such as tolerance, time step size and damping factor for a more efficient solution. There

are two approaches to determining termination of a time step: scaled and unscaled methods. The unscaled method has been used for the current study. This method deems a time step acceptable using a relative and absolute tolerance as shown in Equation 46:

$$\left(\frac{1}{M}\sum_{j=1}^{M}\frac{1}{N_j}\sum_{i=1}^{N_j}\left(\frac{|E_i|}{A_{us,i}+R|U_i|}\right)^2\right)^{0.5} < 1 \tag{46}$$

Where E is the solver's estimate of the absolute error in the current time step, $A_{us,i}$is the unscaled absolute tolerance for DOF i, R is the relative tolerance, U is the solution vector corresponding to the solution at given time step, M is the number of fields, and $N_j$is the number of degrees of freedom in field j.

The steps of the time-dependent solver are defined using time unit, time span for the simulation, time step size, absolute and relative tolerance. The time unit in this study is seconds and the time span, time step size, relative tolerance, and absolute tolerance values are determined by conducting separate studies shown in the following sections.

4.6.1 Simulation Time Step Size

Time step size is one of the most important parameters of the time-dependent solver. A time step size that is too large results in a coarse resolution and important phenomena might get skipped. On the other hand, a time step size that is too small results in unnecessarily long computation times, therefore an optimal time step size must be determined to accommodate a good resolution and a reasonable computation time. In order to find the optimal time step size a study is conducted on the effect of time step size on the number of particles that collide with the surface of the fibers in the model. In this study, the time step sizes in the range of 1e-9 s and 1e-5 s are tested as shown in Figure 38. The computation time for the largest time step size, 1e-5 s, is about 1 min, increasing to about 60 minutes for the smallest time step size, 1e-9 s. Based on this figure, it is evident that the number of particles removed does not change when the time step size is reduced from 1e-8s to 1e-9s. Therefore, a time step size of 1e-8s has been chosen as the optimal time step size for the rest of the study.

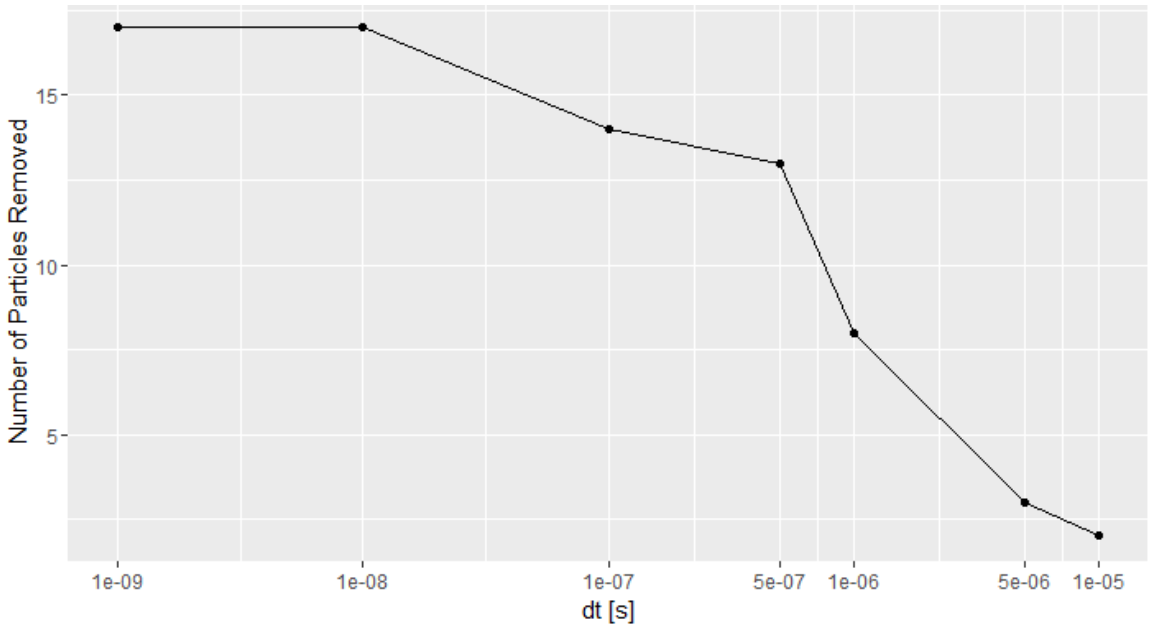

Figure 38 : Time step size analysis for the time-dependent solver

4.6.2 Simulation Time Span

With the particles in the model released all at once from the inlet of the solution domain, it is imperative to make sure sufficient time is available for the particles to reach the outlet of the solution domain. A short simulation time span simply stops the calculations before all potential particles are captured. A sufficiently long time span is different than a sufficiently long calculation time for each iteration: the former ensures a physically meaningful calculation while the latter ensure a converged solution. The parameters controlling convergence are discussed in the next section. Figure 39 shows the number of particles removed from the domain after colliding with the fiber surface as a function of time for four different relative tolerance values. The steps in the plot show the capture of additional particles. In all four cases, after 0.001 seconds of simulation time, there is no more particles being removed suggesting that $t = 0.001\ s$ is a reasonable time to stop the simulation.

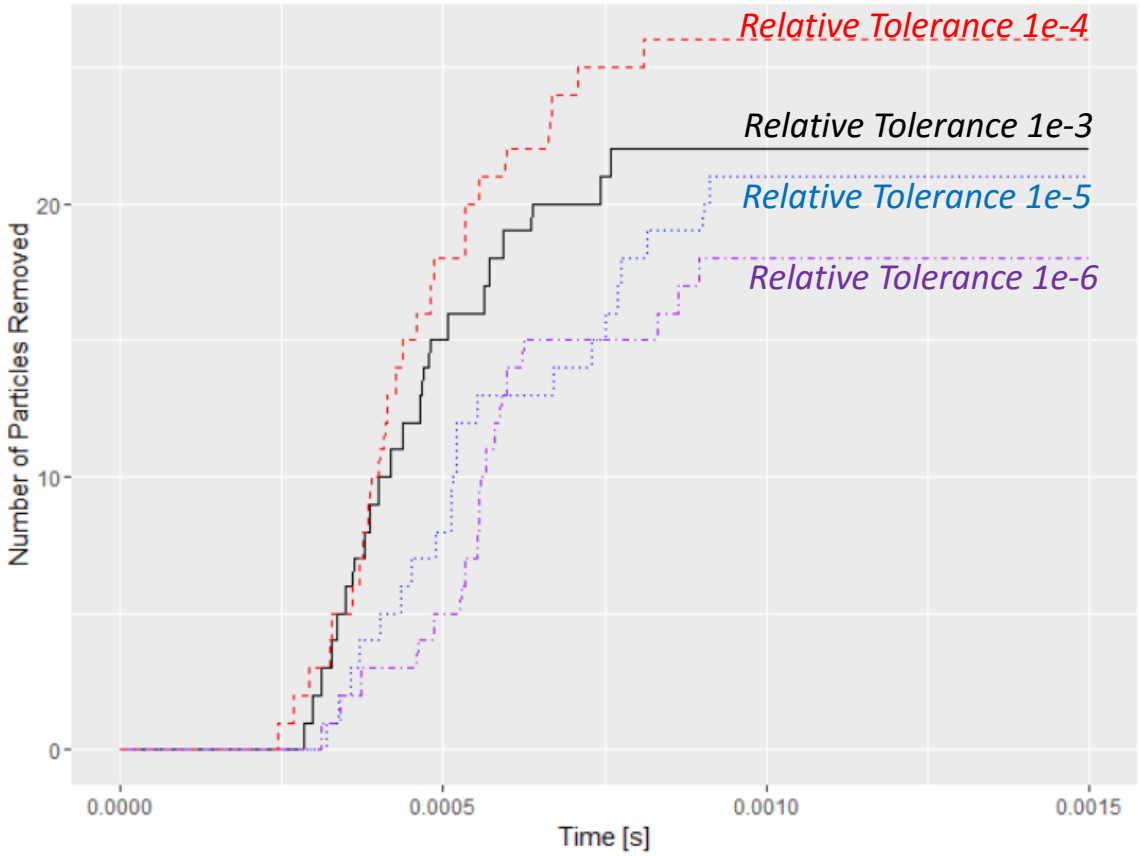

Figure 39 : Simulation time span study for the time-dependent solver

4.6.3 Simulation Tolerance

Both relative and absolute tolerance play an important role in the convergence of the problem. As shown in Equation 46, a larger value for the relative tolerance, makes the error to solution ratio smaller and more likely to meet the convergence requirement even though the error value is large. In other words, a larger value of relative tolerance imposes a less strict convergence requirement on the solver. This phenomenon is evident in the computation time of similar models with different relative tolerances: the model with a smaller value of relative tolerance will take longer to compute. In Figure 39, four curves are plotted for four different values of relative tolerance. The maximum difference between the number of particles removed for the curves in Figure 39, is 10 particles which is insignificant compared to the 4000 particles released in the model. A relative tolerance value of 1e-4 is deemed reasonable to avoid unnecessarily long computation times and to consider the scenario with most particles captured, which is the worst case scenario in a GDL as will be discussed later.

The effect of the value for absolute tolerance on the convergence of the solution is similar to that of the value of the relative tolerance. A study is undertaken to find the optimal value of the absolute tolerance. Figure 40 shows the effect of the change in the value of the absolute tolerance in the number of particles removed after colliding with the fiber. It is evident that for absolute tolerance values smaller than 1e-6, the change in the number of particles removed is insignificant. This value is used in the time-dependent solver for the rest of this study.

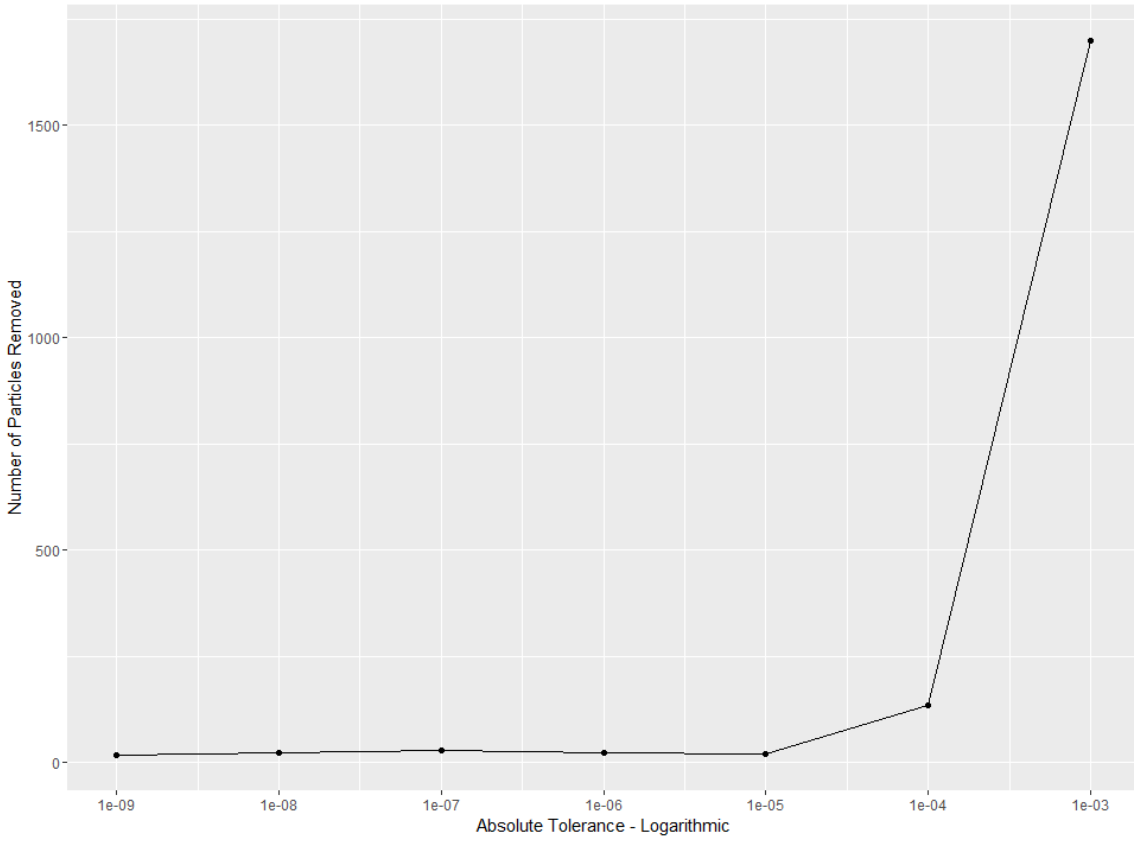

Figure 40 : Absolute tolerance study for the time-dependent solver

4.7 Results and Discussion

The flow field for the model is shown in Figure 41. This figure shows the velocity field and streamlines for the single-fiber model. High velocity regions, colored red, are observed between two vertical fibers and slow velocity regions are observed near the surface of the fiber, shown in blue. Refer to Section 3 for flow field validation.

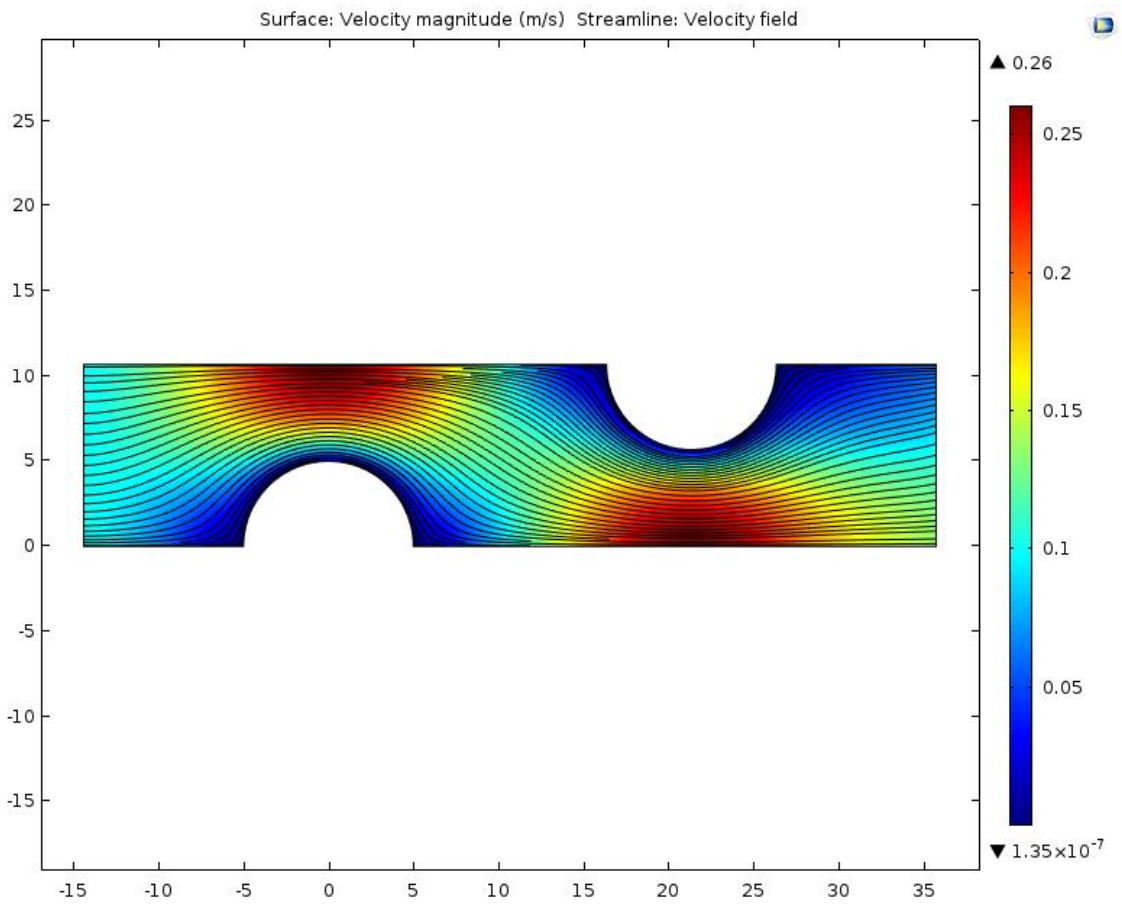

Figure 41 : Single fiber flow field

The results for the flow of particles around a single fiber are presented in the form of change in the efficiency of a single fiber as the diameter of the particles changes. This model has an important assumption that is worth discussing here. As discussed in Section 4.1 particles are assumed to be much smaller than the fiber; one must be careful in considering the physical bounds of the model as well as interpretation of the results. To reiterate, the size of the particle of interest in this model is 0.1 µm which is 100 times smaller than the 10 µm fiber considered in the model. For the results in this section, particles of diameter 0.04 µm to 1.9 µm are considered with the particles with diameters around 1 µm on the verge of contradicting the assumption of small particles. As can be seen in Figure 36, in the vicinity of diameter size of 1 µm, inertial and impaction modes start to become increasingly dominant.

The assumption of small particles, calls for a mesh study to understand the effect of minimum element size of the mesh on the motion and ultimately capture of the particles. Figure 42 to Figure 44 show three meshes used for this study. Mesh 1, shown in Figure 42, is the finest mesh with minimum element size of 0.005 µm. Mesh 2, shown in Figure 43, is coarser than mesh 1 with minimum element size of 0.1 µm and mesh 3, the coarsest of the three , illustrated in Figure 44 has a minimum element size of 0.2 µm.

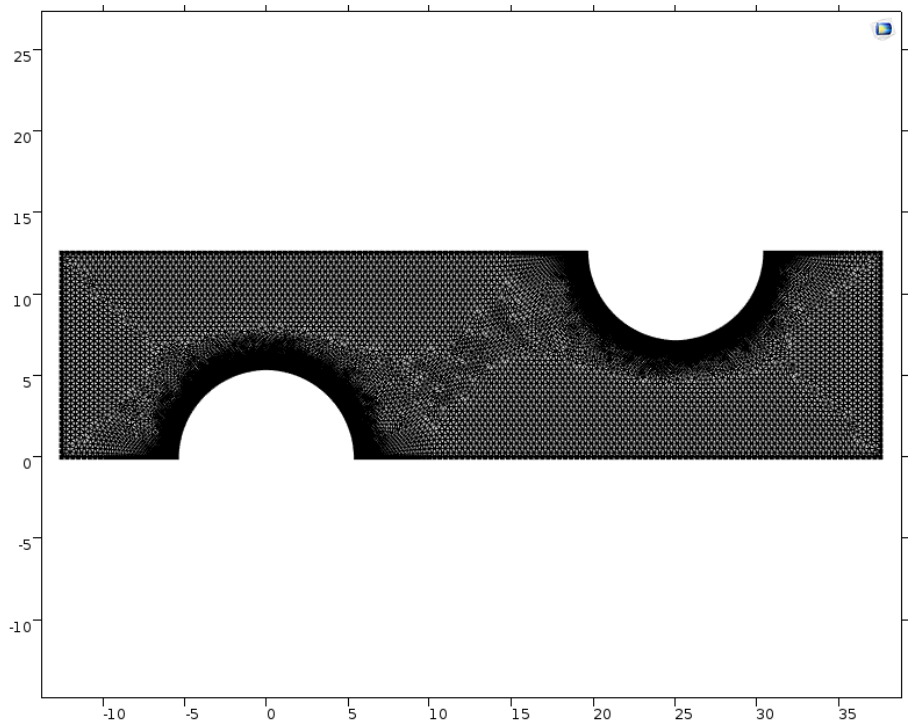

Figure 42 : Fine mesh for solving single fiber efficiency (mesh 3)

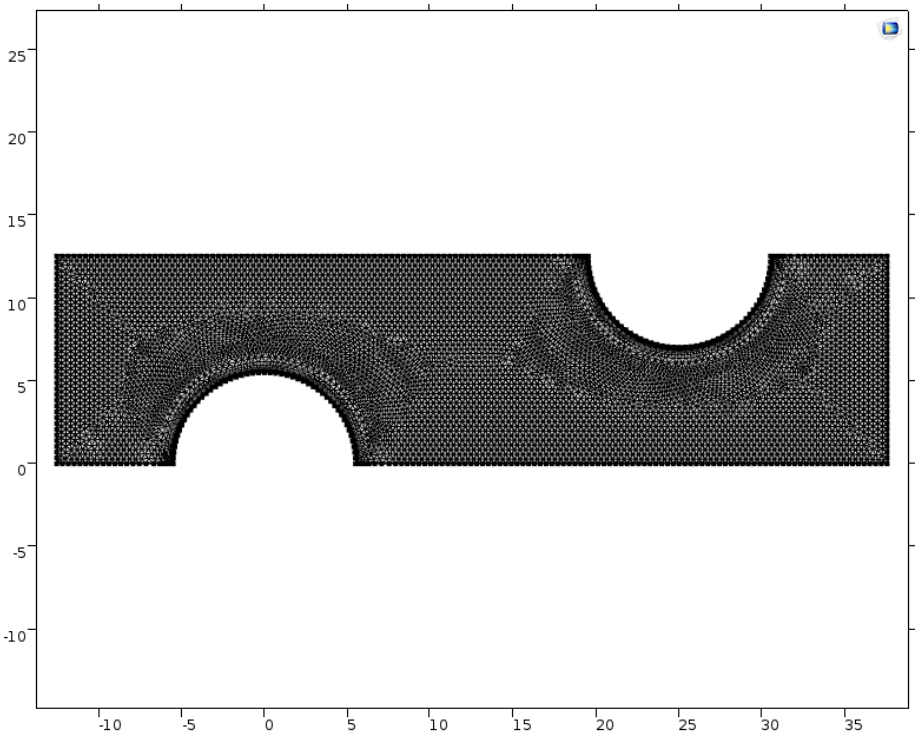

Figure 43 : Normal mesh for solving single fiber efficiency (mesh 4)

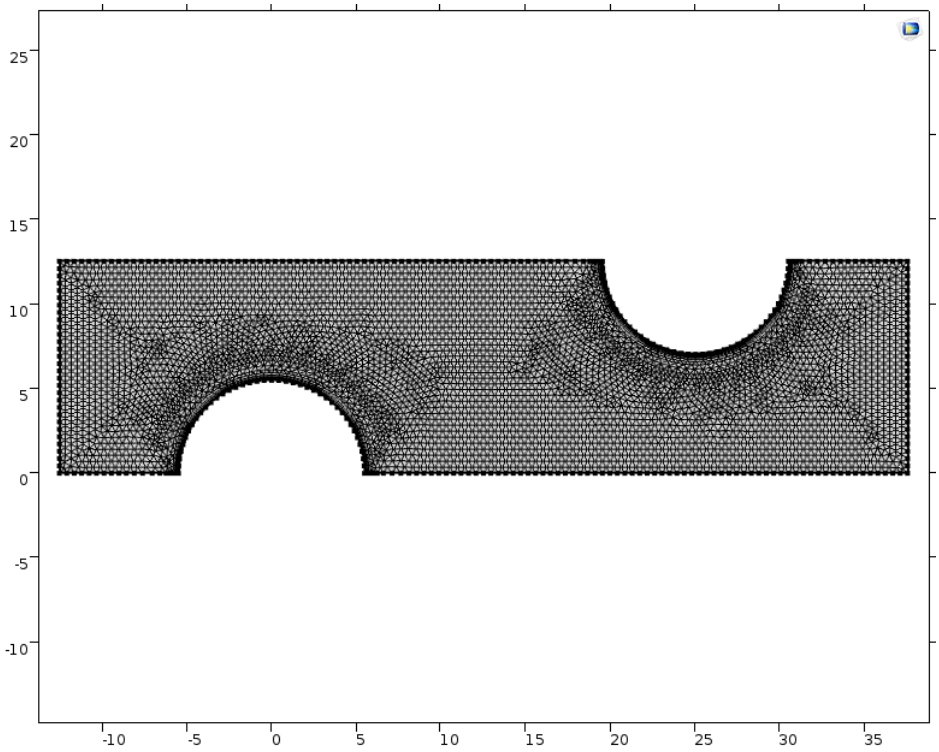

Figure 44 : Coarse mesh for solving single fiber efficiency (mesh 5)

The results of the single fiber efficiency model are presented in Figure 45 with experimental results by Lee [118] and theoretical results by Tan [111] plotted for comparison. Three observations are made based on these results. First, both the experimental and theoretical results reveal the same pattern: decline of the single fiber efficiency as the particle size is decreased to a range between 0.1 and 1 μm followed by increase of the single fiber efficiency. The curves for the experimental and theoretical results are not in perfect agreement, which is due to the randomness inherent in the motion of the particles. The second observation is that the numerical results for the three meshes are very similar and the minimum size of the element in the mesh seems to have minimal effects on the single fiber efficiency calculated.

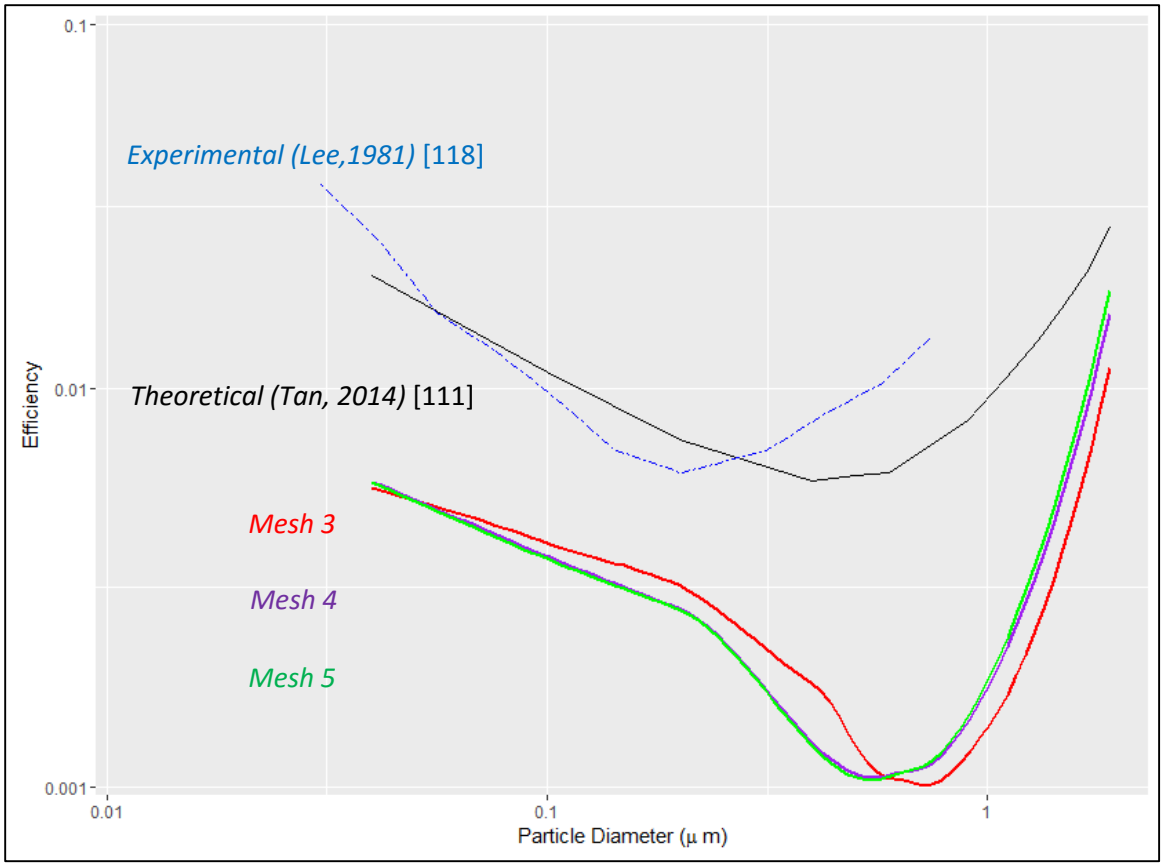

Figure 45 : Single fiber particle capture efficiency results

The third observation is the similar pattern between the numerical results and the experimental and theoretical results. While the agreement is not perfect, the similarity is evidence for reasonability of the assumptions made in the model and hence, validates the single fiber efficiency model.

4.8 Summary

In this stage of the study, particles were added to the solution for flow around a single-fiber. The particles were uniform in size and were solved using a one-way coupling scheme, where the solution for the particles is calculated based on the solution for the flow. In order to find the correct setup for the model, simulation time step size, simulation time span, and simulation tolerance studies were conducted yielding the following parameters for the model: Simulation time step size was determined to be 1e-8s, simulation time span was determined to be 0.001s, and simulation tolerance was 1e-6. The particle capture results of the single fiber model showed reasonable agreement with theoretical and experimental results, correctly predicting the transition between particle capture mechanisms. With single-fiber model fully set up, the next stage of the study discusses a multi-fiber model with particles.

5 Multi-Fiber with Particles

This stage of the study is an attempt to modify the single fiber model into a more realistic one. The single fiber model represented the fundamental unit in the structure of the gas diffusion layer and it served as a verification step. Having assurance of the validity of the single fiber model, in this stage of the study, more fibers are added to the model to create an array of 16 fibers.

5.1 Approach to Modeling

The approach to modelling in this stage of the study is an extension of the approach in the single fiber stage. First, the flow around the fibers is calculated as a steady state solution. Then, the particles are introduced to the model with their motion calculated based on the steady state solution of flow around the fibers. The properties of the particles and fluid remain the same.

5.2 Model Setup

The geometry of this model is an extension of the geometry of the single fiber model. The geometry is shown in Figure 46.

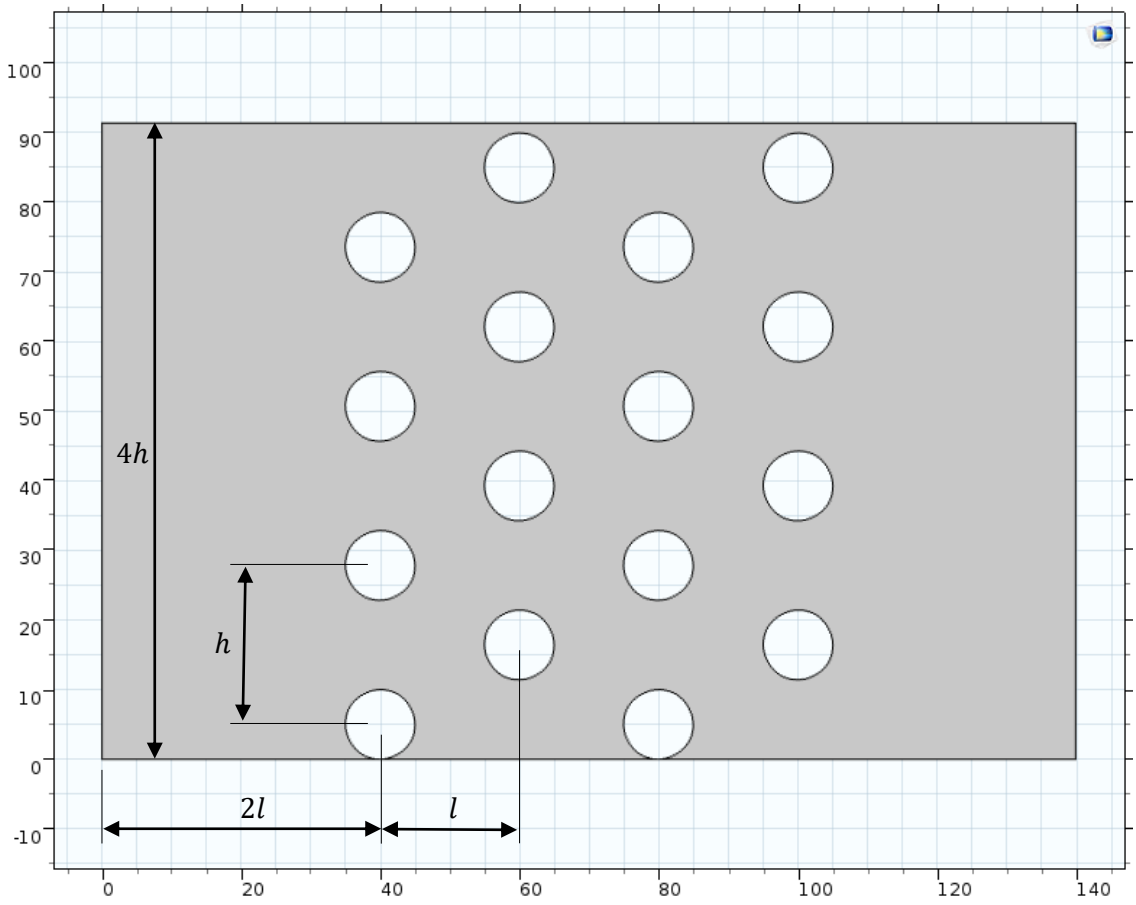

Figure 46: Geometry of the multi-fiber model (axes in µm)

l and h are the horizontal and vertical distances between fibers in the model respectively. The values for l and h are determined based on the solid volume fraction of the fiber and the relative ratio of l and h. Solid volume fraction is defined as:

$$\alpha = 1 - porosity = \frac{\pi d_f^2}{4lh} \tag{47}$$

The relative ratio of l and h plays an important role in the model. A value of 0.875 is determined suitable for this model based on the work of Wang et al. [87]. The solid volume fraction of the model used in this study is 17.2% and the values of l and h are calculated to be 19.98 µm and 22.84 µm respectively. A distance of $2l$ is considered in the entrance and exit of the model.

Even though the single fiber model was based on a staggered arrangement of fibers in the solution domain, a parallel model is also considered in this stage of the study. The geometry of the parallel model is shown in Figure 47. The results of the parallel model will be compared to the staggered model in the next sections.

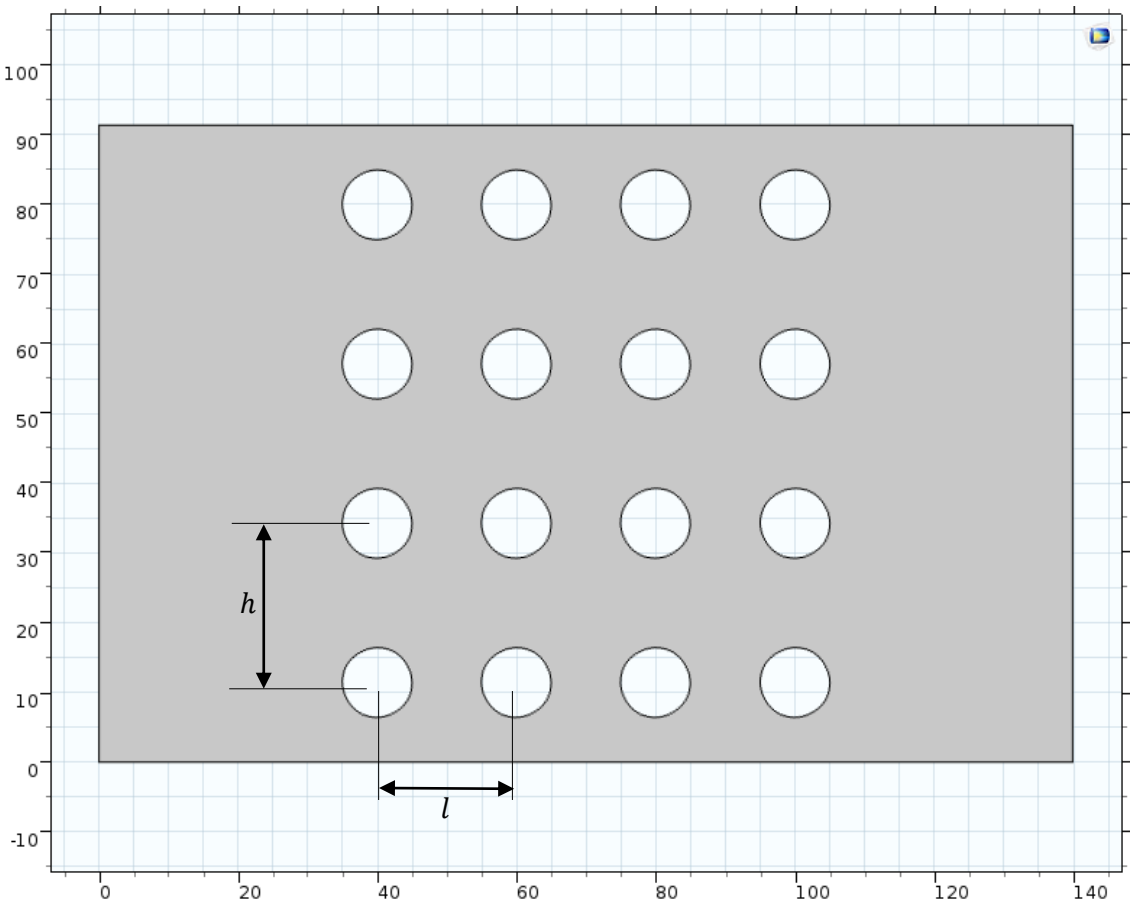

Figure 47 : Geometry of the multi-fiber model (parallel configuration)

5.3 Governing Equations

The governing equations for this model are identical to the governing equations for the single fiber as discussed in Section 4.4. All the initial assumptions about the model remain unchanged. The only change in the solution of the model is the simulation time span. Since the length the particles are expected to travel in the current model is about three times the length in the single fiber model, it is important to increase the time span of the simulation time accordingly. Based on the study of the single fiber model a time span of 0.001 s deemed sufficient to have the particles reach the outlet of the model. In the current multi-fiber model, this value is multiplied by three.

5.4 Boundary Conditions

There are two sets of boundary conditions used in this model: flow field boundary conditions and particle boundary conditions. In Figure 48, both types of boundary conditions are shown with the particle boundary conditions underlined.

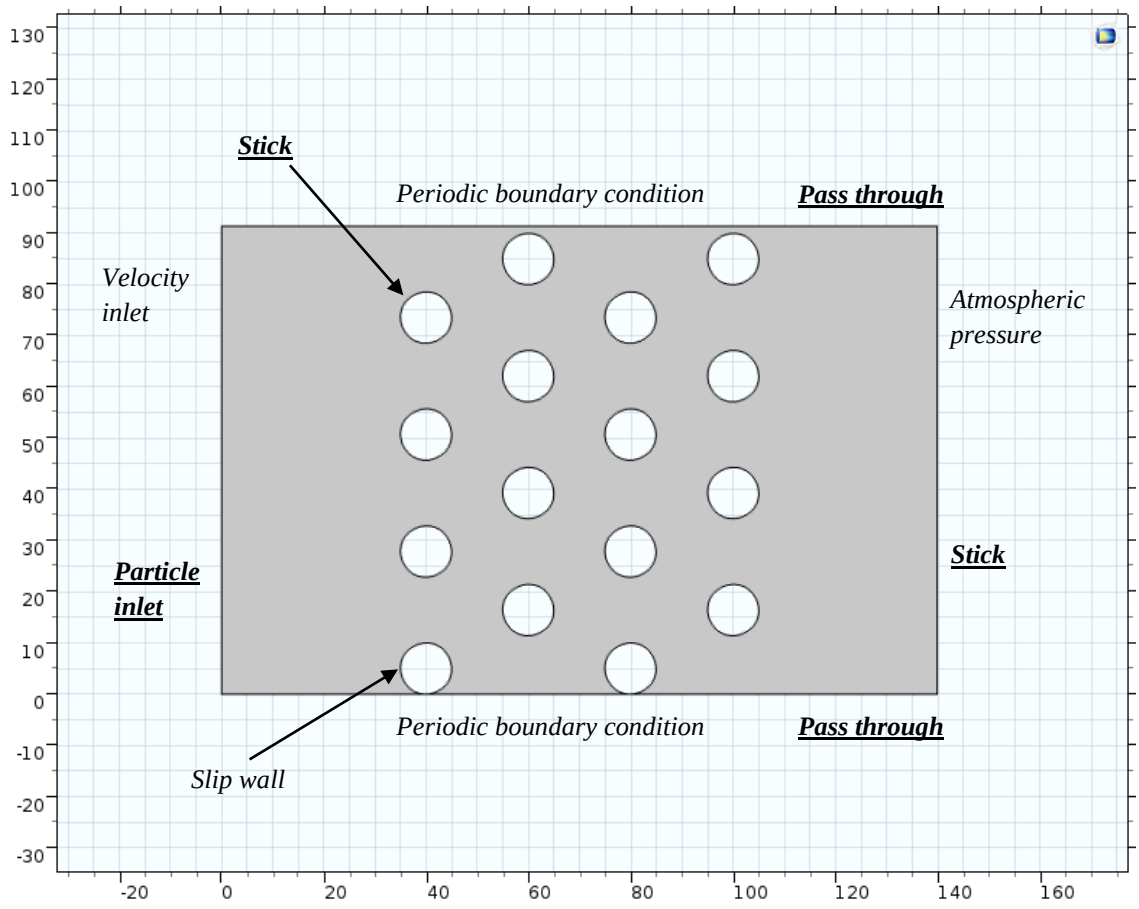

Figure 48 : Flow field and particle boundary conditions of the multi-fiber model (axes in μm)

Air enters the solution domain from the left-hand side with a uniform velocity of 0.14 $m\,s^{-1}$, consistent with a Reynolds number of 0.1 based on the diameter of the particle, and exits the domain through the outlet on the right-hand side where pressure is atmospheric. Periodic boundary conditions on the top and bottom wall are used to represent the repeating pattern of fibers. A slip boundary condition is applied to the surface of all fibers with parameters discussed in Section

3.4.4.2. The particles enter from the particle inlet with the initial velocity of 0.14 $m\ s^{-1}$ and after passing through the mesh of fibers, collide with the outlet of the domain where a stick boundary condition is applied for counting purposes. The particles are assumed to pass through the top and bottom walls upon collision with them. Such particles will be entering another hypothetical solution domain identical to the current domain. The particles that collide with the fibers are assumed to stick to the fibers and then immediately removed from the domain. These particles do not affect the flow or other particles.

5.5 Results and Discussion

The focus of this stage of the study is to validate the particle capture performance of the model in an attempt to build a reliable foundation for more complex models. Three meshes are considered for this stage, each progressively coarser than the base mesh (mesh 1). The mesh characteristics are discussed in this section.

Mesh 1, is the finest of the three meshes used for this study. The mesh, shown in Figure 49, consists of triangular elements away from the surface of the fibers, and rectangular elements near the surface of the fibers. The rectangular elements are more suited for boundary layer compared to triangular elements. The mesh has a total of 41700 elements with a minimum element size of 0.005 µm.

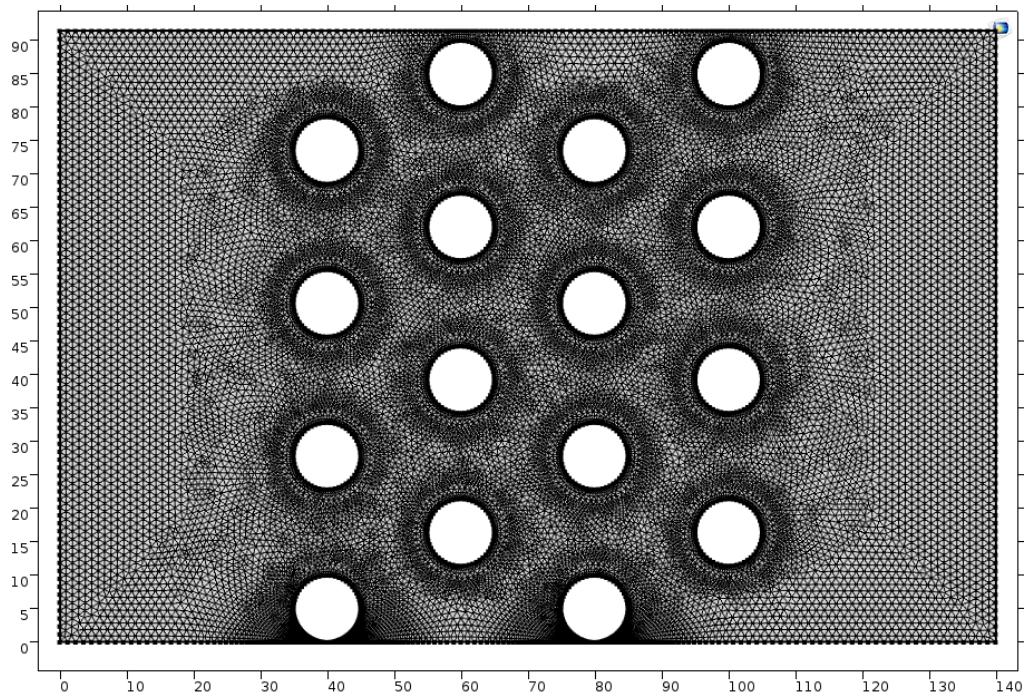

Figure 49 : Multi-fiber mesh 1

Mesh 2, depicted in Figure 50, is a coarser version of mesh 1 with a total of 28000 elements and a minimum element size of 0.1 µm.

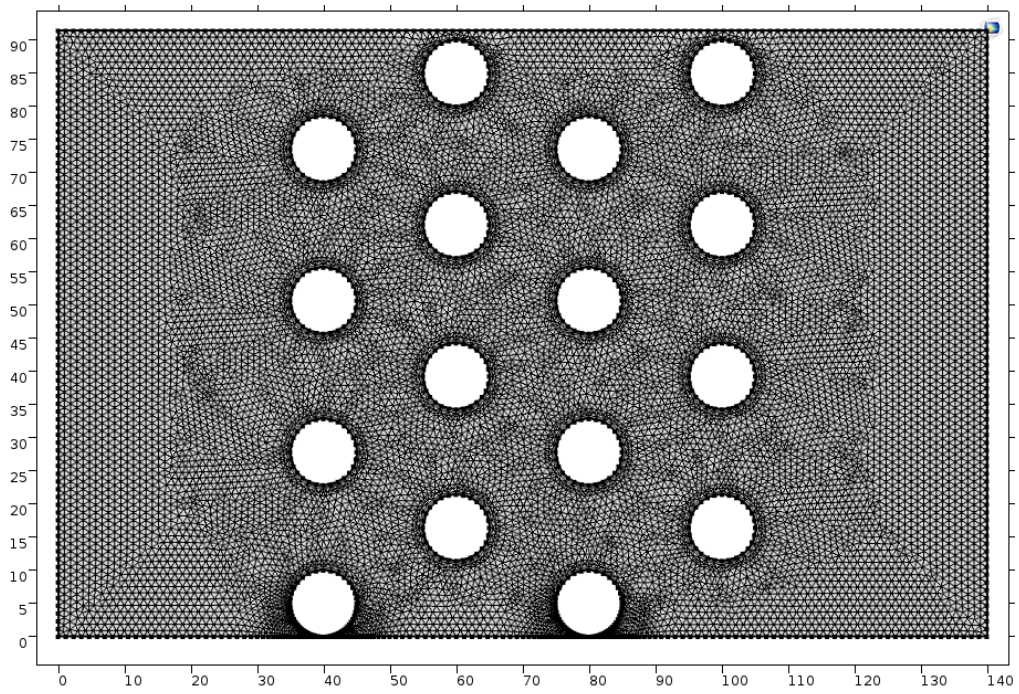

Figure 50 : Multi-fiber mesh 2

Mesh 3 is shown in Figure 51 and is the coarsest of all. The number of elements in the mesh is 19000 with a minimum element size of 0.2 µm.

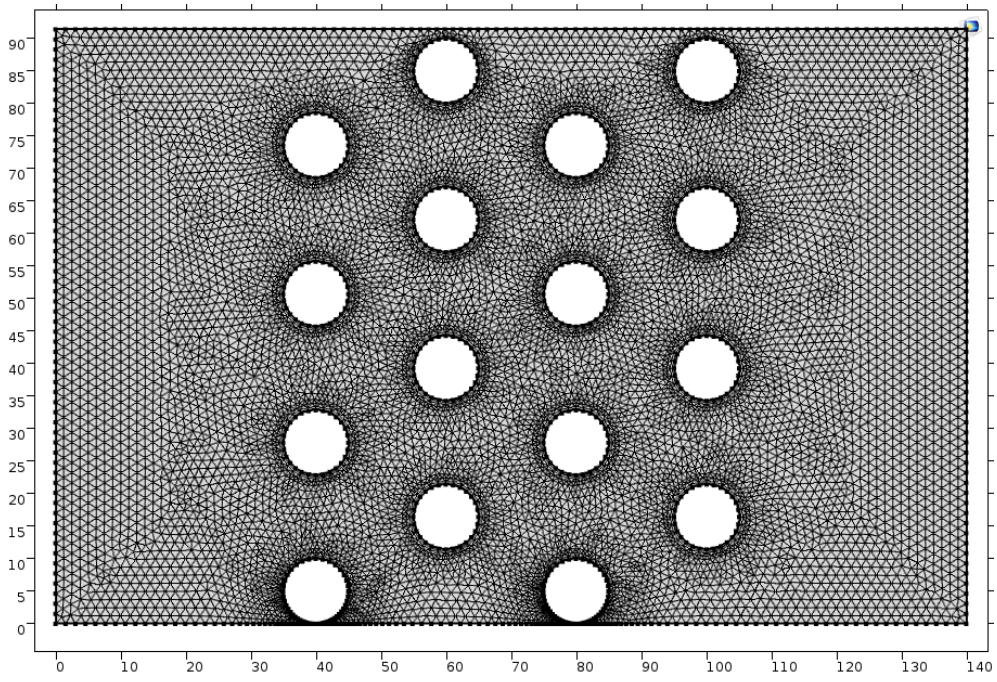

Figure 51 : Multi-fiber mesh 3

One of the important characteristics of each mesh is the ratio of the minimum element to the size of the particle. The ratio is 0.05 for mesh 1, and 1 and 2 for mesh 2 and mesh 3 respectively. A ratio

too large or too small results in a mesh that does not accurately resolve the interaction of the particles with the fluid. For example, if the ratio is too small, it means that the mesh element size is much smaller than the particle size. In such a scenario, the particle would occupy multiple elements as it travels through the domain and given the inherent interpolations among the elements for solving the model, the solution to the motion of the particle would be compromised.

The flow field around the fibers for the staggered configurations is shown in Figure 52. The flow enters the domain at a velocity of $0.14\ m\ s^{-1}$ and passes through the array of fibers experiencing a minimum velocity of $1.65 \times 10^{-5}\ m\ s^{-1}$ near the surface of each fiber and a maximum velocity of $0.359\ m\ s^{-1}$ downstream of each fiber as indicated by the red color in Figure 52.

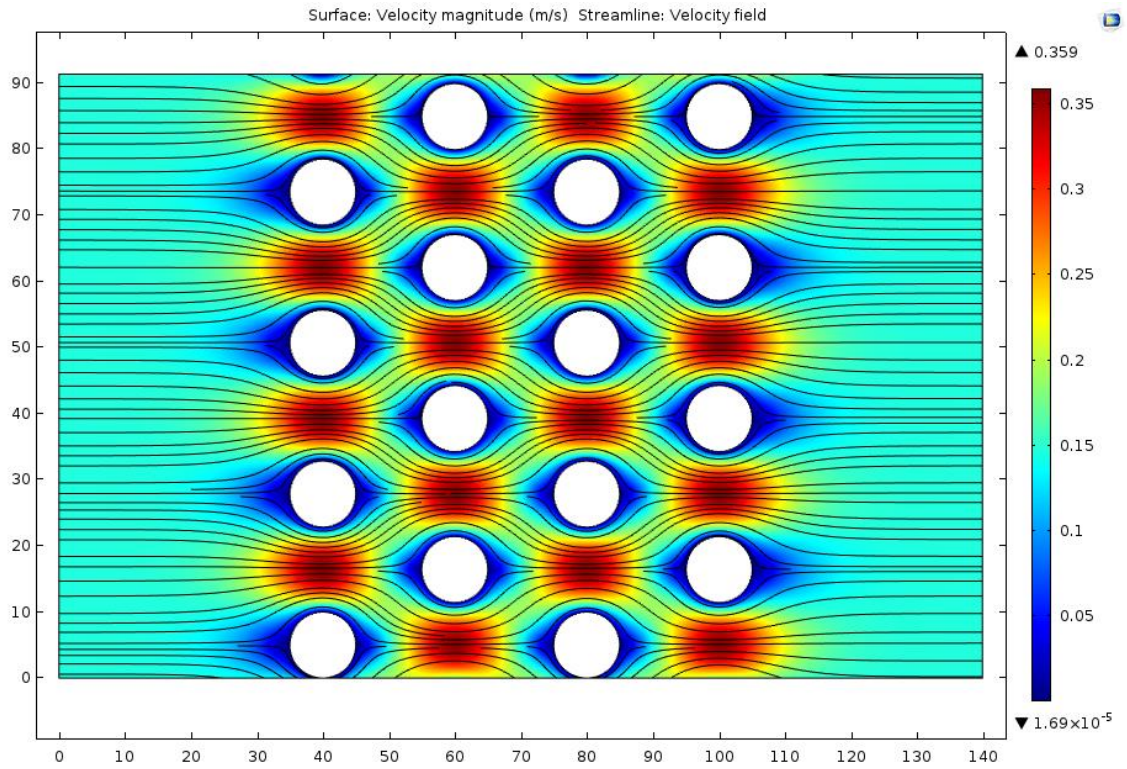

Figure 52 : Multi-fiber flow field (staggered configuration)

Figure 53 shows the horizontal velocity profile at a hypothetical line drawn at $x = 40\ \mu m$. Based on this figure, it is observed that the maximum horizontal velocity occurs half-way between two vertically consecutive fibers and the minimum velocity occurs at the top and bottom of the fibers. It is also noted that since a slip-wall boundary condition is defined at the surface of the fibers, the

minimum velocity value is not zero, as it would have been in an otherwise no-slip boundary condition scenario.

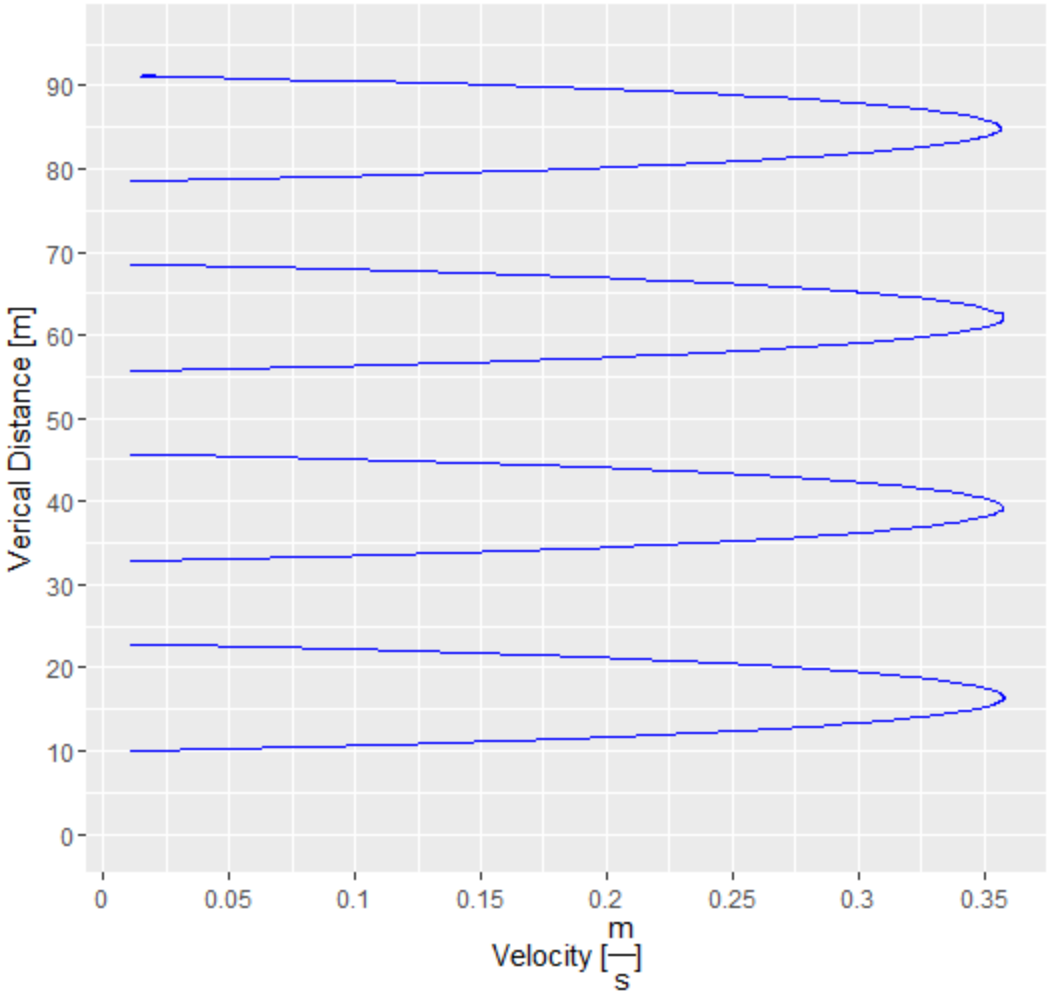

Figure 53 : Horizontal velocity at x=40 µm

The results for particle capture efficiency of the multi-fiber model are presented in Figure 54. The vertical axis shows the particle capture efficiency of the model in logarithmic scale. To reiterate, the particle capture efficiency of the model is determined as the ratio of the number of particles that stick to the fibers to the number of particles that reach the outlet of the model. The particles that cross the pass-through walls are not taken into account in this calculation.

Based on the theoretical formulation for the staggered model, discussed in Section 3, as the size of the particles gets larger, the mode of particle capture transitions from Brownian diffusion to interception and inertial impaction. This transition is shown in Figure 36 and partially in Figure 54 in the theoretical curve. This pattern is also visible in the results of the current multi-fiber study with all three meshes showing reasonable agreement with the theoretical results.

It is noted that the differences between the three curves corresponding to the three meshes used in this model are insignificant leading to the conclusion that it is best to use the coarsest mesh proceeding to the next stages of the study.

The results for the parallel model are also shown for comparison purposes in Figure 54. In the parallel model, the initial decrease in the efficiency of the model is more distinguished. However, the subsequent jump in the efficiency is rather weak without much recovery. It must be noted that the theoretical model in this figure is based on a staggered model and one must not interpret the disagreement between the theoretical curve and the parallel curve due to inaccuracy of the model or theory. The importance of the comparison is to determine which configuration of fibers is suitable for proceeding to the next stage of the study. The overall efficiency in the parallel model seems to be less than the staggered model therefore for worst-case-scenarios, the staggered model is considered appropriate.

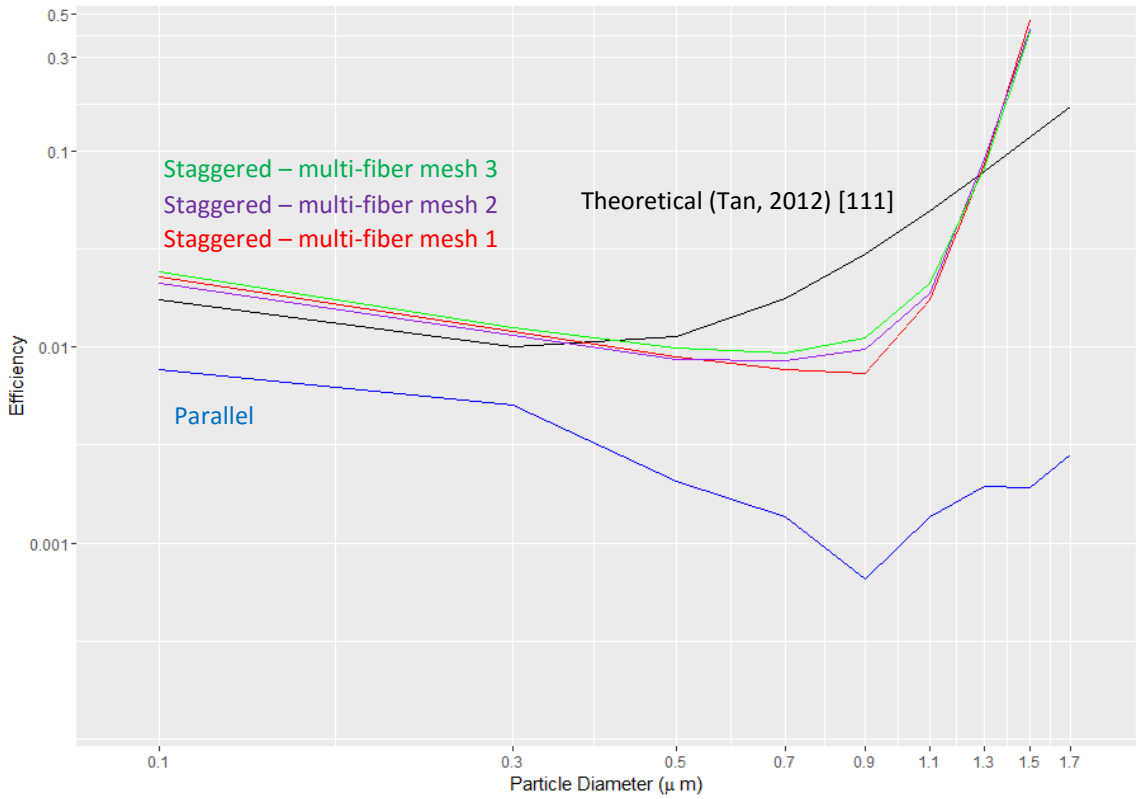

Figure 54 : Multi-fiber particle capture results comparison

With the multi-fiber model validated, the groundwork for the ultimate goal of studying the effect of humidity on particle capture in the gas diffusion layer is laid and the next section explains the approach towards modeling the effect of humidity.

5.6 Summary

A staggered multi-fiber model, with 16 fibers in total, was studied in this stage of the study. Using similar governing equations and boundary conditions as the single-fiber model, the particle capture efficiency of the multi-fiber model was compared to theoretical data. For small particles,

the Brownian particle capture mechanism was dominant. As the particle size increased, the dominant capture mechanism transitioned to inertial impaction and interception following the theoretical curve with reasonable agreement. The next stage of the model shows the development of a humidity model which will be added to the multi-fiber model.

6 Humidity Model

So far, the stages of the study have been focused on building the foundation for studying the effect of humidity on the gas diffusion layer. First a single fiber model was developed followed by addition of particles. Then the single fiber model was extended to include more fibers and the results were validated. This section discusses the development of the humidity model.

6.1 Background

Due to the lack of research on the effect of humidity on the filtration efficiency of fibrous media, it is decided the best way to approach the modeling of this phenomenon is by breaking the problem into effect of relative humidity on parameters that can be input to the model such as particle diameter, particle density, and particle bounce. The effect of humidity on fibrous media is assumed to stem from four major sources: the effect of humidity on the size of the particles, the effect of humidity on the density of the particles, the effect of humidity on the particle bounce behavior, and the effect of humidity on the density of air. Each one of the four factors are studied separately and ultimately, the cumulative effects are presented.

6.2 Effect of Relative Humidity on Particle Size

Adding humidity to particles for the purpose of particle detection is a well-established practice used by major manufacturers of aerosol detection equipment. TSI, a leading particle-related equipment manufacturer, uses this concept in the model TSI 3775 particle detector. As shown in Figure 55, water vapor is added to the stream of incoming particles. After mixing of vapor with the particles, the mix is heated to saturate the flow and then using cooling, condensation occurs on the particles and their size increases facilitating better detection as they pass through the optics.

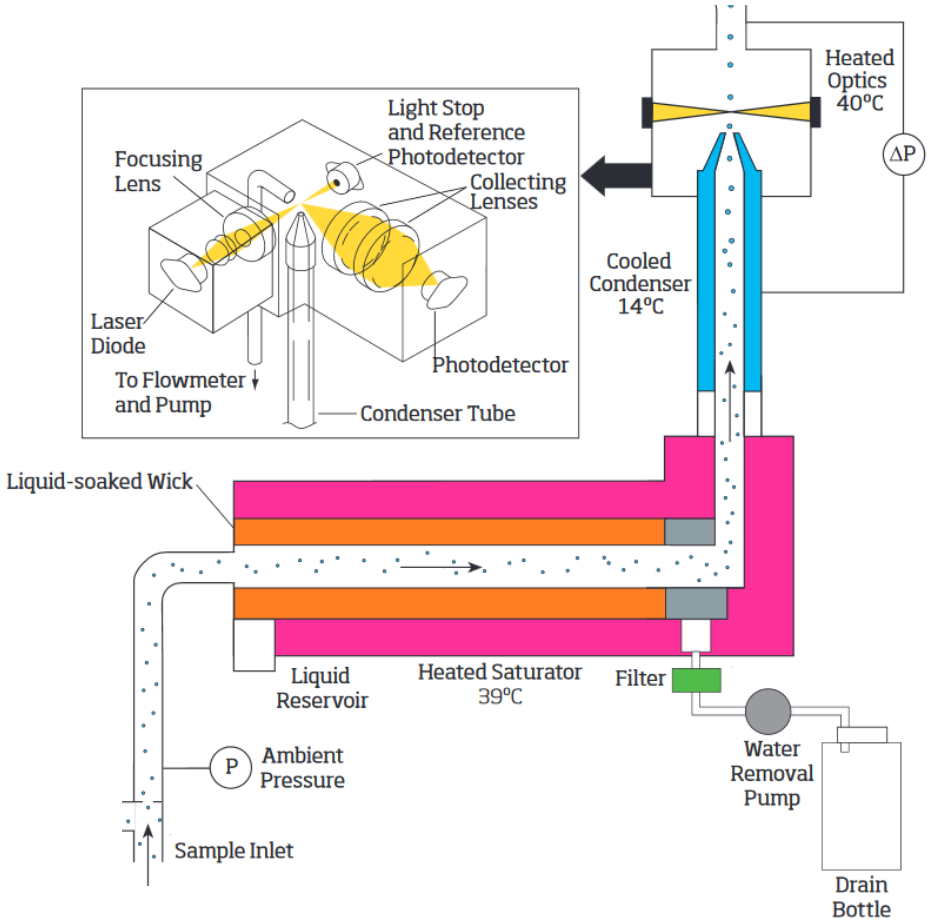

Figure 55 : Schematic of operation of condensation particle counter [119]

In the case of the particle detector, saturation and condensation of vapor onto particles is controlled by adjusting the temperature of the flow. Zhang et al. has proposed a model for the increase in size of particles under various relative humidties based on the composition of the particle [64]. Zhang's model takes into account the ratio of water-soluble species to non-water-soluble species in the dry particle, as well as the ratio of nitrates to sulfates in the dry particle. The amount of each one of the abovementioned constituents in the dry particles, affects the amount of water vapor absorbed by the particle and hence the change in the size of the particle. Equation 48 shows the particle diameter growth as a function of relative humidity (RH) and as a function of the composition of the particle represented by the term $f(RH, Composition)$.

$$\frac{D}{D_0} = \left[1 + f(RH, Composition)\frac{RH}{1 - RH}\right]^{\frac{1}{3}} \tag{48}$$

D is the wet particle diameter and D_0 is the dry particle diameter. The composition term is defined based on C_r , β , and A which are defined in Equations 49 to 54

$$f(RH, Composition) = \frac{1}{1 + \beta} C_r \tag{49}$$

$$C_r = 1.05 - 2.61RH + 2.40RH^2 \qquad A < 0.5 \tag{50}$$

$$C_r = 0.52 - 1.04RH + 1.06RH^2 \qquad 0.5 < A < 2.0 \tag{51}$$

$$C_r = 0.93 - 1.94RH + 1.65RH^2 \qquad A < 0.2 \tag{52}$$

$$\beta = \frac{non\ water\ soluble\ species\ in\ dry\ particle}{water\ soluble\ species\ in\ dry\ particle} \tag{53}$$

$$A = \frac{amount\ of\ nitrate\ in\ dry\ particle}{amount\ of\ sulfate\ in\ dry\ particle} \tag{54}$$

It is important to note that the composition of the particle has significant impact on its size change in humid conditions. In the current study both β and A are assumed to be one, meaning that the amount of non-water-soluble species is equal to the amount of water-soluble species and the amount of nitrate is equal to amount of sulfate in the dry particle. Figure 56 shows the relationship between relative humidity level and the size of the particle. It is observed that as the humidity level increases, the particle becomes larger with a relatively large growth at relative humidity levels above 80.

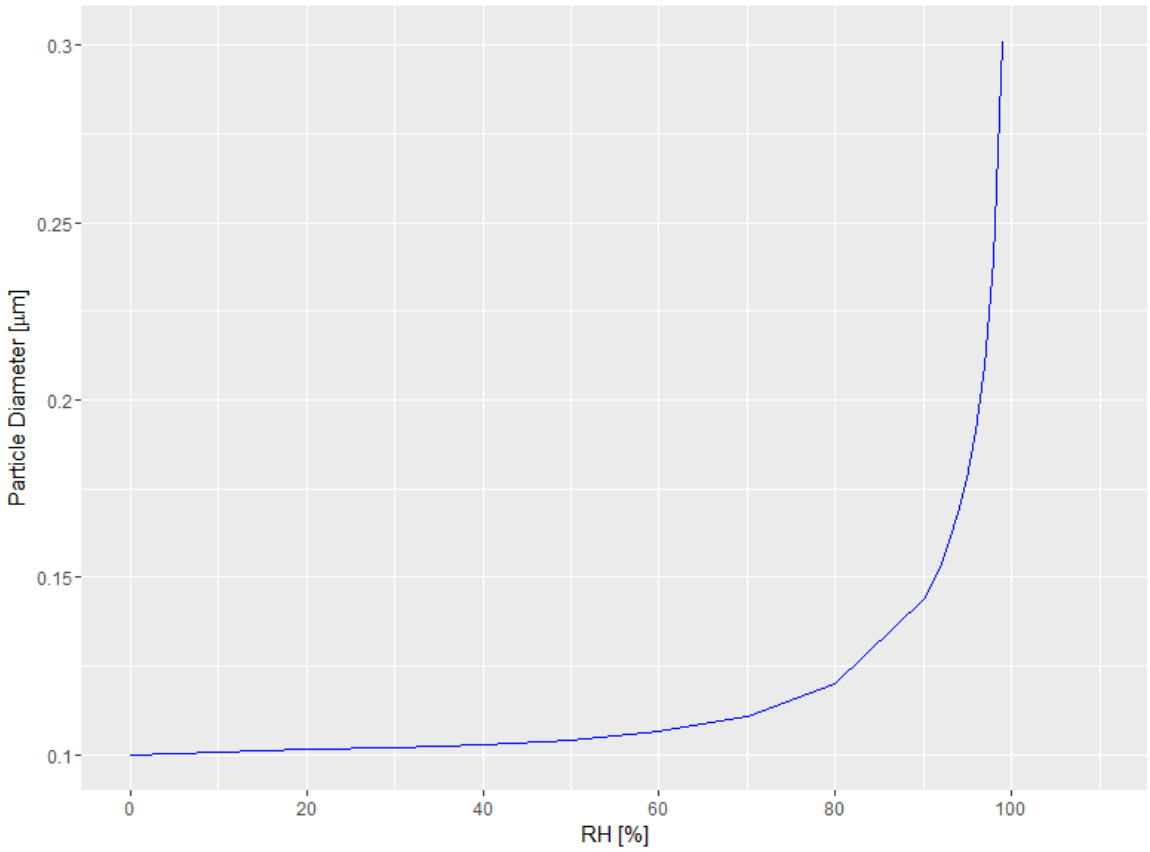

Figure 56 : Effect of relative humidity on particle diameter

Figure 57 shows the change in the efficiency of the multi-fiber model as a function of the change in the size of the particles as humidity is increased. It is worth reiterating that this graph does not represent the full effect of humidity on efficiency and rather, shows one aspect of it: the change in particle size as humidity changes. It can be seen that as the humidity level increases, the particle size increases and the particle capture efficiency decreases.

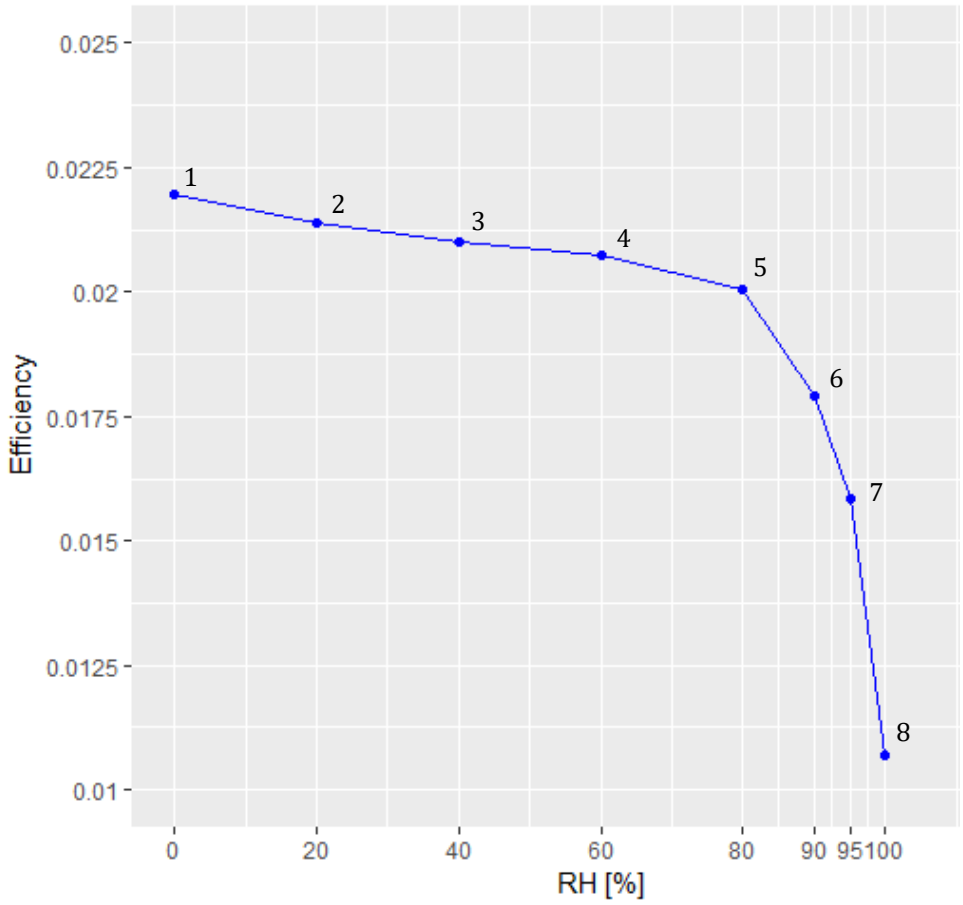

Figure 57 : Effect of particle size change due to change in humidity on particle capture efficiency. Effective diameter at each numbered point in ascending order is 0.1 μm, 0.1015 μm, 0.103 μm, 0.1065 μm, 0.1201 μm, 0.1441 μm, 0.178 μm, 0.3007 μm

The results might seem counter-intuitive, however, the drop in capture efficiency is well in agreement with the particle capture theory presented in Figure 36. The drop in capture efficiency is simply due to the transition of capture mechanism from Brownian diffusion to interception and inertial mechanisms.

6.3 Effect of Relative Humidity on Particle Density

The extra water content due to increase in humidity is expected to form in layers on the surface of the particle as evidenced by the particle size increase discussed in the previous section. Water, with density of $1000\ kg\ m^{-3}$, added to the surface of a dry particle, with assumed density of $2000\ kg\ m^{-3}$ results in a particle with a density in between. In other words, the higher the water content, the closer the density of the mixture to that of water. Stein et al. uses Zhang's diameter growth factor and presents a model for the density of the particle under different levels of relative humidity as shown in Equation 55 [63]:

$$\rho_{p,RH} = \frac{\rho_{p,dry} + [\left(\frac{D}{D_0}\right)^3 - 1]}{\left(\frac{D}{D_0}\right)^3} \quad (55)$$

$\rho_{p,RH}$ is the wet particle density and $\rho_{p,dry}$ is the dry particle density. Figure 58 shows the effect of relative humidity on the particle density: the higher the level of relative humidity, the lower the density of the particles.

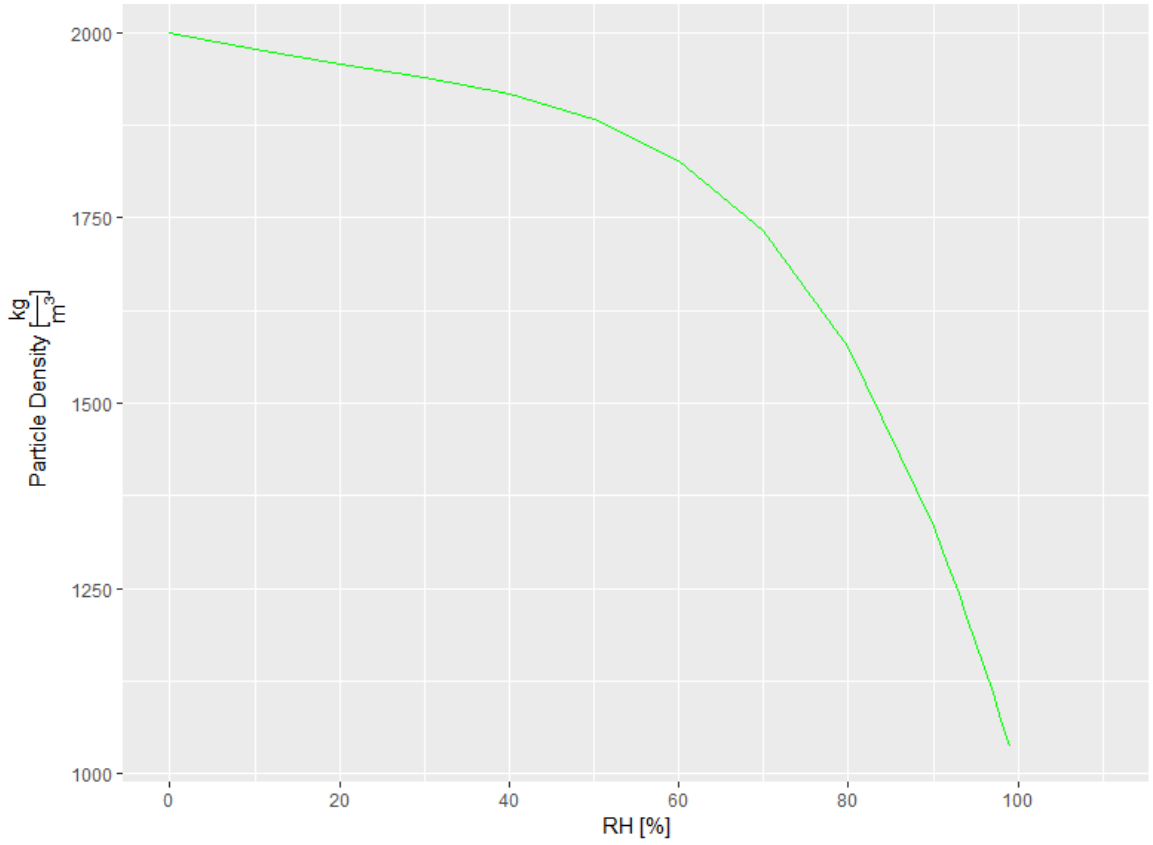

Figure 58 : Effect of humidity on particle density

The isolated effect of decrease in particle density as result of humidity on particle capture efficiency is shown in Figure 59. The change in particle capture efficiency is deemed insignificant: it has increased from 2.22% to 2.27% when changing humidity level from 0% to 100%.

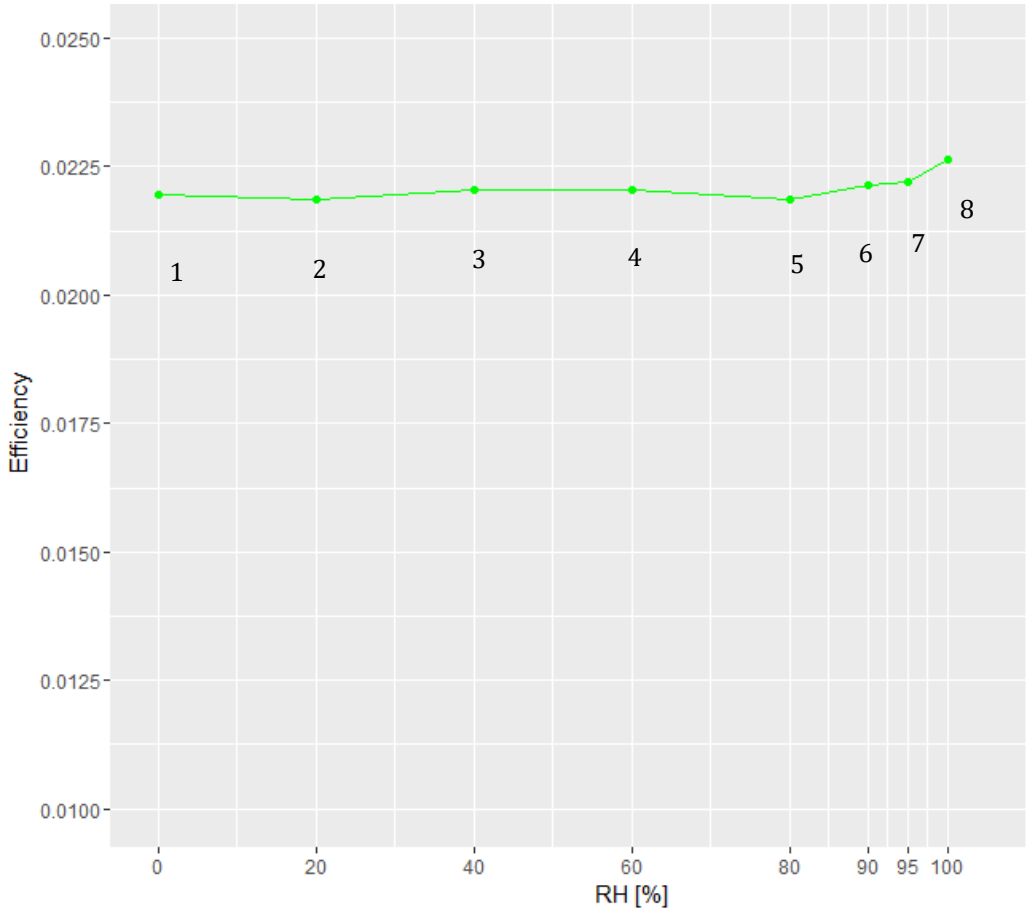

Figure 59 : Effect of particle density change due to change in humidity on particle capture efficiency. Effective density at each numbered point in ascending order is $2000\ kg\ m^{-3}$, $1958\ kg\ m^{-3}$, $1828\ kg\ m^{-3}$, $1916\ kg\ m^{-3}$, $1577\ kg\ m^{-3}$, $1334\ kg\ m^{-3}$, $1177\ kg\ m^{-3}$, $1037\ kg\ m^{-3}$

6.4 Effect of Relative Humidity on Air Density

The air properties used in the previous stages of the study were dry air properties and it is important to study the effect of humidity on these properties. The property of interest here is the air density which is expected to change as the humidity level increases. Equation 56 shows the formula for calculating the moist air density :

$$\rho_{moist\ air} = \frac{\frac{P}{R_a T}(1+W)}{(1+W\frac{R_w}{R_a})} \tag{56}$$

Where P is the pressure of the mix, atmospheric pressure here, R_a is the gas constant for dry air with value of $287\ J\ kg^{-1}K^{-1}$, T is the temperature of the moist air, $298\ K$, R_w is the gas constant for water vapor with a value of $462\ J\ kg^{-1}K^{-1}$, and W is the humidity ratio defined as the ratio of mass of water vapor to the mass of dry air in the mixture [120]. The values for the humidity ratio are obtained from psychrometric charts published by American Society of Heating,

Refrigerating and Air-Conditioning Engineers [121]. The effect of relative humidity on the moist air density is shown in Figure 60.

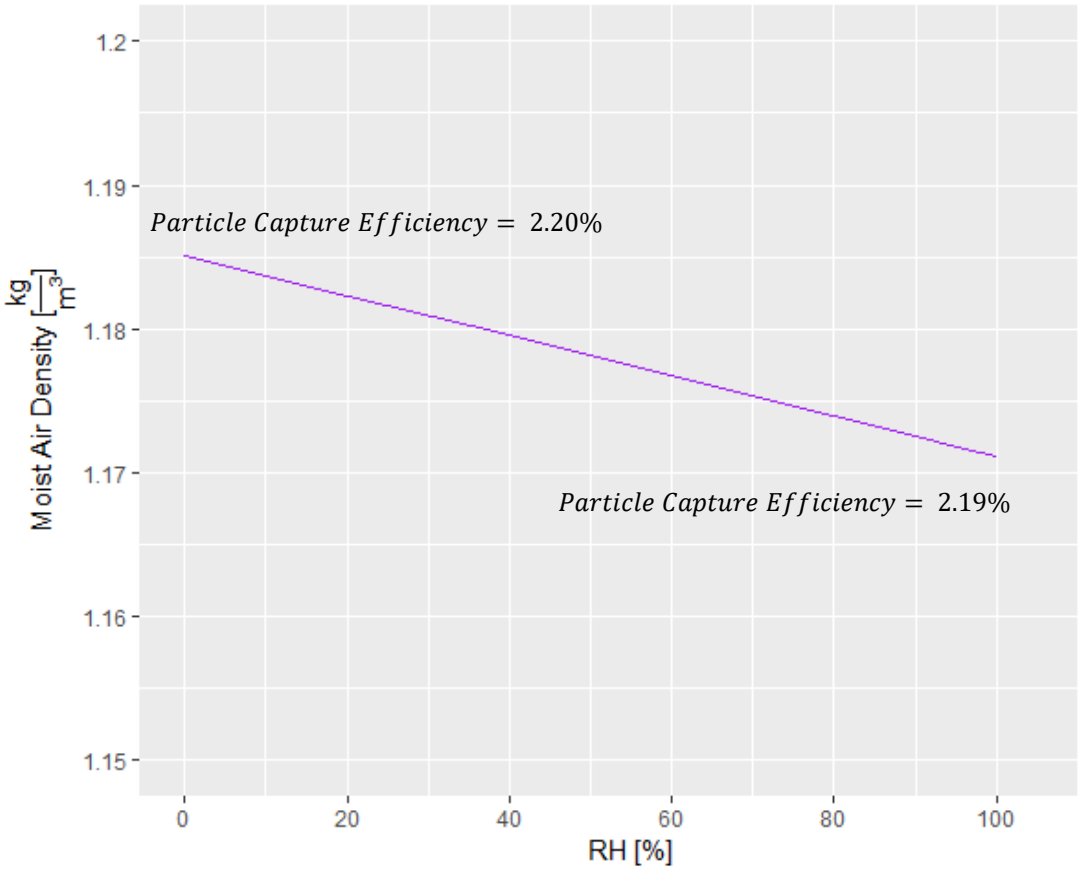

Figure 60 : Effect of relative humidity on moist air density

The moist air density changes from a value of 1.185 kg m^{-3} to 1.171 kg m^{-3} when humidified from 0% relative humidity to 100%. The decrease in the air density is considered very small and once input into the multi-fiber model, it resulted in very small change in the particle capture efficiency. As illustrated in Figure 60, the particle capture efficiency drops 0.01%. Therefore, the effect of humidity on air density is deemed insignificant.

6.5 Effect of Relative Humidity on Particle Bounce

Particle bounce has many applications and it has been studied for particles of different materials. It is well known that the roughness of the impact surface plays an important role. Surfaces that have coatings of oil or water improve particle adhesion resulting in reduced particle bounce [111]. This phenomenon occurs because the presence of a liquid layer at the surface significantly increases the capillary forces [122].

In order to approach the effect of relative humidity on particle bounce, first, the operation of a particle cascade impactor is explained and then the effect of relative humidity on the operation of particle impactor is extended to fibrous media.

Cascade impactor is a common instrument used for measuring particle size [123]. As shown in Figure 61, the larger particles, due to their higher inertial force, separate from the flow streamlines and collect on the impaction surface, also known as the substrate. The smaller particles continue to flow past the substrate to the next impaction stage, with progressively smaller particles being collected on the lower stages until a desired cut-off particle size is reached.

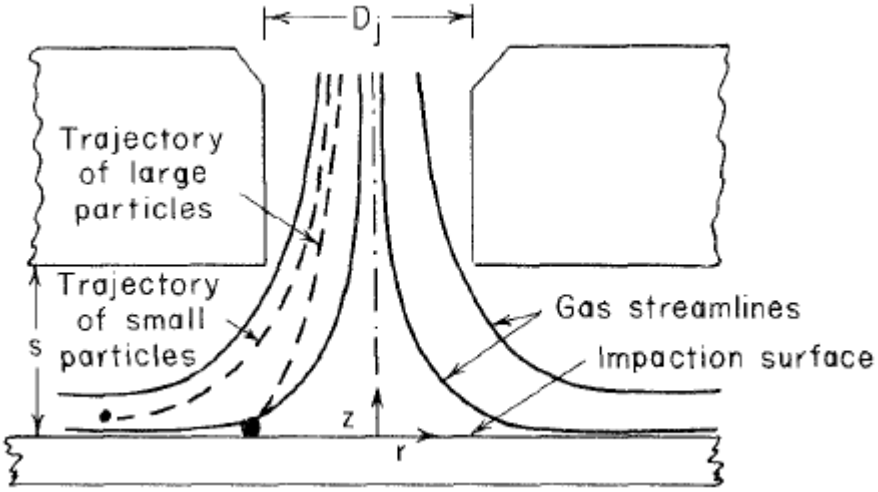

Figure 61 : Schematic of a particle impactor [123]

Historically, it was believed that upon impaction, particles stick to the surface of impact, however, this is not always the case and many studies have shown that laboratory-generated and atmospheric aerosols' bounce can be significant. Particle bounce has been investigated for particle impactors and fibrous media such as filters. The similarity between the particle bounce behavior in these two applications is extremely useful in extending the understanding of particle behavior from one application to another. The characterization of the particle bounce involves studying of the bounce behavior of the particle using particle impactors with different operation conditions including different substrates and different levels of relative humidity.

Bateman et al. investigated the effect of relative humidity on the adhesion and bounce of submicron particles composed of liquid oleic acid, solid ammonium sulfate, and solid polystyrene latex (PSL) from an aluminum substrate [124]. Bateman et al. observed that particle bounce is strongly related to relative humidity, even for non-hygroscopic PSL particles as illustrated in Figure 62. Bateman et al. noticed that at high relative humidity levels, layers of water adsorb to the surfaces resulting in adhesion force between the particle and the surface upon impaction.

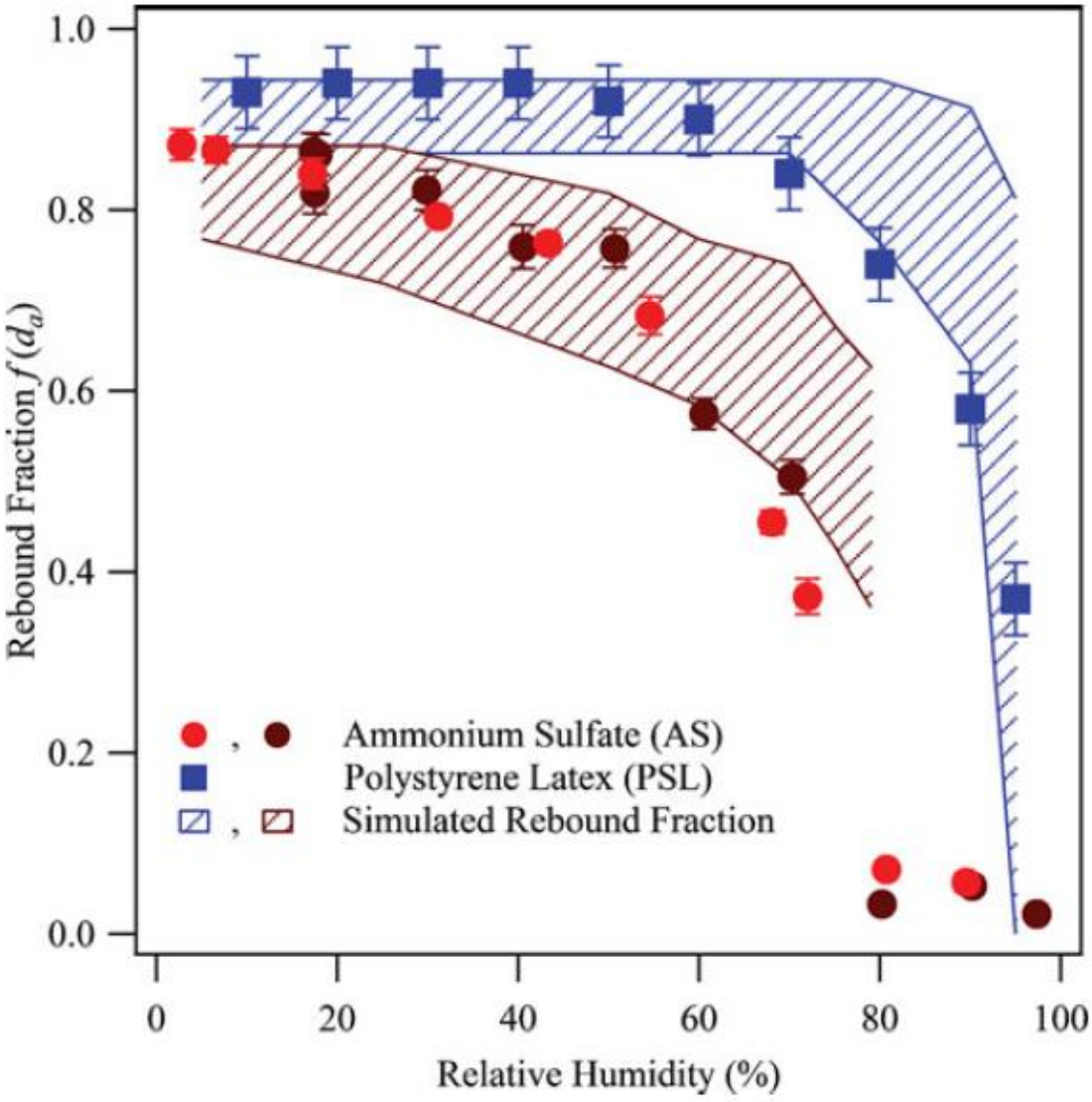

Figure 62 : Effect of relative humidity on the rebound fraction of test aerosols of ammonium sulfate and polystyrene latex (PSL) from an aluminum substrate [124]

Bateman's results for PSL are extremely useful in the modeling of particle bounce in fibrous media. The only obstacle in the way of application of his results to the model under study is the material used for the substrate in his experiments which is aluminum. This issue can be remedied by finding the difference in particle bounce between aluminum and a similar fiber material at very low relative humidity and adjusting Bateman's results based on that.

Chang et al. have experimentally investigated the effect of impaction substrate design and material on particle bounce [125]. Chang et al. use various particle sizes in combination with different substrate materials in a configuration shown in Figure 63. Particles drawn through the inlet section pass through the acceleration nozzle and impact the substrate, shown in the figure as a black rectangle. The particles that do not hit the substrate together with the bouncing particles are collected at the filter.

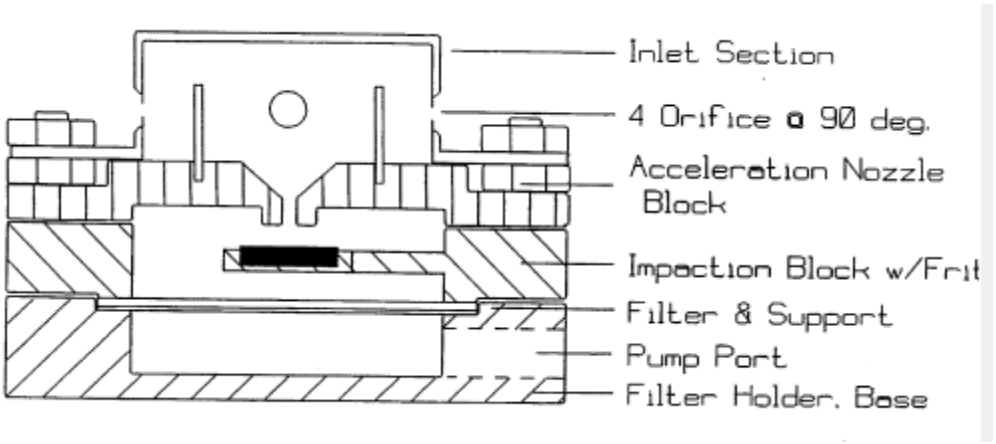

Figure 63 : Schematic of the impactor used by Chang et al. [125]

The collection efficiency of each substrate is reported as the ratio of particles that collect on the substrate, C_{sub} , to the total particles that are collected on the substrate and on the filter, C_{fil} , as shown in Equation 57:

$$collection\ efficiency = \frac{C_{sub}}{C_{sub} + C_{fil}} \tag{57}$$

Figure 64 shows the collection efficiency of the aluminum and glass fiber substrate for different particle diameters. Glass fiber is the closest material to carbon fiber among glass fiber, Teflon, and Nuclepore, all tested by Chang et al.. The minimum particle diameter shown here is 1 µm which is 10 times larger than the target 0.1 µm diameter. What is important is the difference in particle bounce, measured by one minus collection efficiency, between the two substrates. Glass fiber has shown a rather steady collection efficiency with different particle diameters and aluminum has shown a decreasing collection efficiency with increasing particle diameter meaning that as the diameter has increased, bounce fraction has increased. Simple linear regression is used to model the data in the range of diameter sizes used in the experiments, the interpolation lines are dashed in Figure 64. The model is then used for extrapolating the data to the target diameter of 0.1 µm as shown in Figure 64, it is determined that for the target 0.1 µm particle, the difference in particle bounce between aluminum and glass fiber would be 20%.

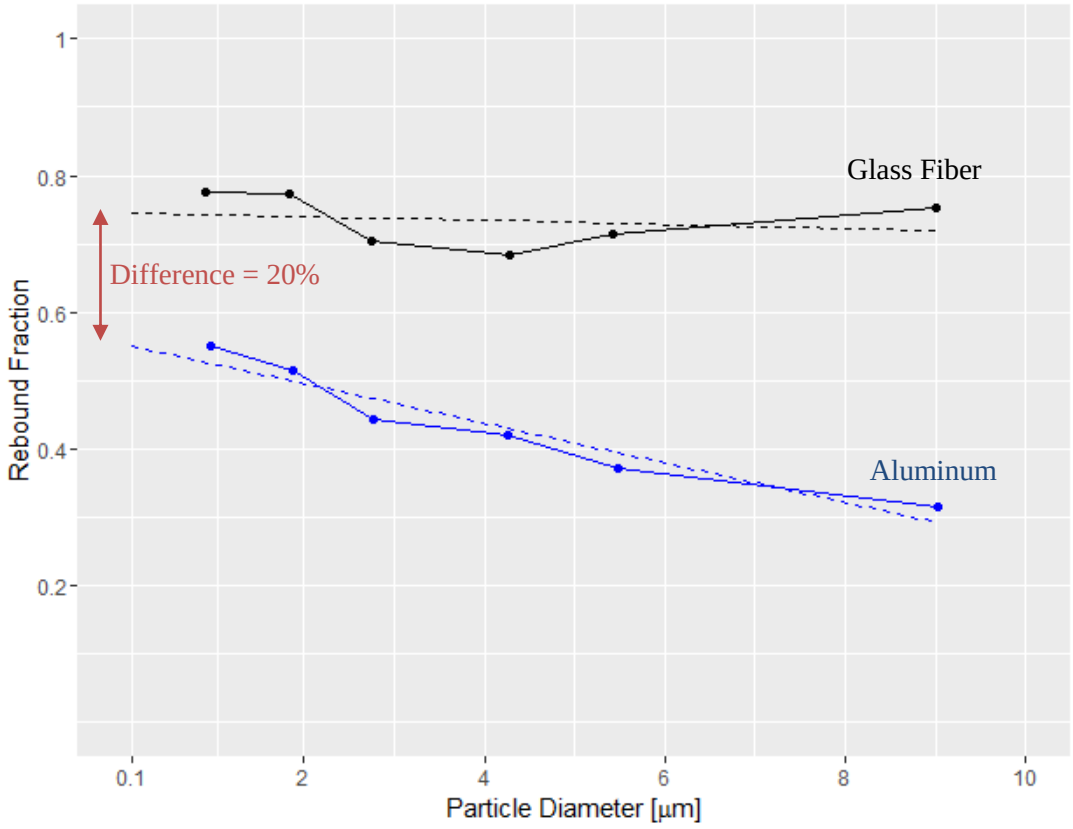

Figure 64 : Particle collection efficiency for aluminum and glass fiber [125]. Dashed lines show linear interpolation.

Now, the measurements by Bateman et al. can be adjusted to reflect the effect of substrate material. In doing so, a few assumptions are made that are worth underlining: First, the bounce behavior of fibers under study is assumed to be similar to that of fiber glass. Second, the effect of humidity on particle bounce is assumed to be similar for aluminum substrate and gas diffusion layer substrate. To reiterate, this means that the change in particle bounce fraction is assumed to be the same regardless of the material used in the substrate, however, the unique properties of each material need to be accounted for by shifting the curve for aluminum substrate. In the case of this study, the shift is 20% as discussed above. Under these assumptions, the fiber is expected to have a bounce probability of 75% and 0% in relative humidity levels of 0% and 100% respectively.

Table 9 : Bounce probability of particles off fibers at different relative humidity levels

RH (%)	Bounce probability – aluminum (%)	Bounce probability – GDL fiber (%)
0	95	75
20	94	60
40	94	45
60	90	30
80	77	15
90	60	8
95	39	4
100	2	0

Upon implementation of the fiber bounce probabilities for different relative humidity levels, it is observed that the particle capture efficiency shows a slight increase, as depicted in Figure 65. The efficiency has increased from a value of 2.05% to 2.20%. The change is rather small but not insignificant. The current multi-fiber model under study only includes 16 fibers, which is very few.

Once the number of fibers in the model is increased, the change in bounce probability becomes more important.

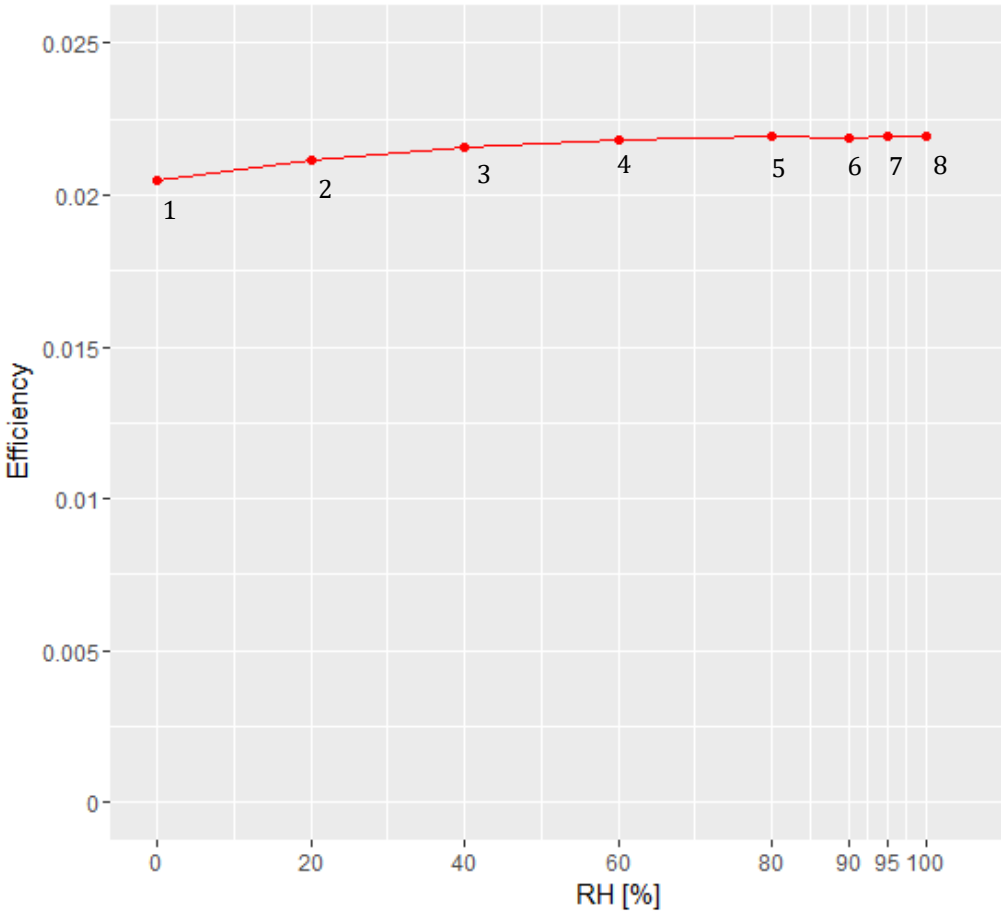

Figure 65 : Effect of bounce probability due to change in relative humidity on particle capture efficiency. Bounce probability for each numbered point in ascending order is 0.75, 0.6, 0.45, 0.3, 0.15, 0.08, 0.04, 0.00

6.6 Cumulative Effect of Relative Humidity

To reiterate, four mechanisms were considered for modeling the effect of relative humidity on the particle capture efficiency: effect of relative humidity on particle size, particle density, air density, and particle bounce. The cumulative contribution of each mechanism is shown in Figure 66. Of the four mechanisms, the effect on particle size in the most dominant and the effect on air density is the smallest.

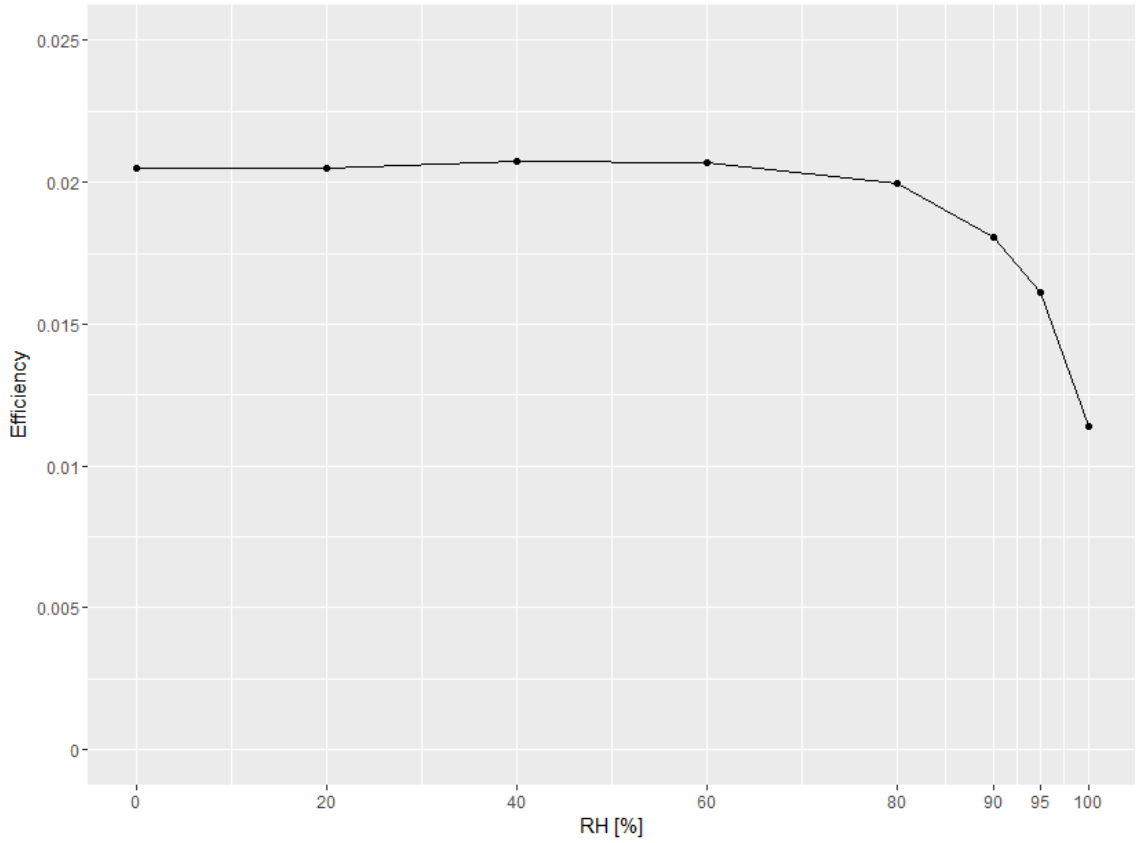

Figure 66 : Cumulative effect of relative humidity on particle capture efficiency, dry particle diameter 0.1 µm

The results of the humidity model developed in this section suggest a decrease in the overall particle capture efficiency as the relative humidity has increased. This is extremely useful in controlling the relative humidity of the cathode stream in a fuel cell. Based on these results, it is ideal to humidify the air that enters the fuel cell to 100% ensuring minimum particle capture in the GDL. The humidity model in this section only considers a few fibers, however, it is not sufficient for GDL modeling. The next section considers the entire thickness of a GDL.

6.7 Summary

This stage of the study focused on developing a humidity model based on the effect of relative humidity on particle size, particle density, air density, and particle bounce. It is found that relative humidity results in increase in particle size, decrease in particle density, decrease in air density, and decrease in particle bounce probability. Each of these effects was tested individually on the multi-fiber model for particle diameter 0.1 µm revealing effective particle size to be the most significant factor and effective air density to be the least significant factor. Finally, all four factors were cumulatively implemented in the multi-fiber model revealing a decreasing pattern in particle capture efficiency as relative humidity increased. The next stage of the study incorporates the humidity model into a GDL model.

7 Particle Capture in the Gas Diffusion Layer

In this stage of the study a staggered model of the gas diffusion layer (GDL) is challenged with particles as the relative humidity varies from 0% to 100%. The GDL is an important component of PEM fuel cells and it is imperative to establish a basic understanding of it prior to any analysis. The following section provides background information about the GDL.

7.1 Background

The GDL plays a major role in PEM fuel cells in mass transport between the flow channels and the membrane. The GDL transports reactant gas to the catalyst layer and it has a strong effect on PEM fuel cell performance [126]. The GDL is often fabricated by stacking carbon fibers or woven carbon cloth on top of each other which results in a range of porosities and pore size distribution, dictating the mass transport characteristics of the GDL [42]. PEM fuel cell cathodes use a two-layer or three-layer structure for configuration of the components. The two-layer structure consists of a catalyst layer (CL) and a GDL while the three-layer configuration is composed of CL, GDL, and a microporous layer (MPL), where the MPL is located between the CL and the GDL as shown in Figure 67 [127]. Frequently, the GDL is coated with hydrophobic materials such as polytetrafluoroethylene (PTFE) to prevent water flooding. It is also common to add a carbon base layer (CBL) and multiple PTFE layers to create a multiple layer configuration [128]. The microporous layer added between the GDL and the CL is believed to facilitate liquid water removal from the CL and enhance the chemical and mechanical stability of the CL [129].

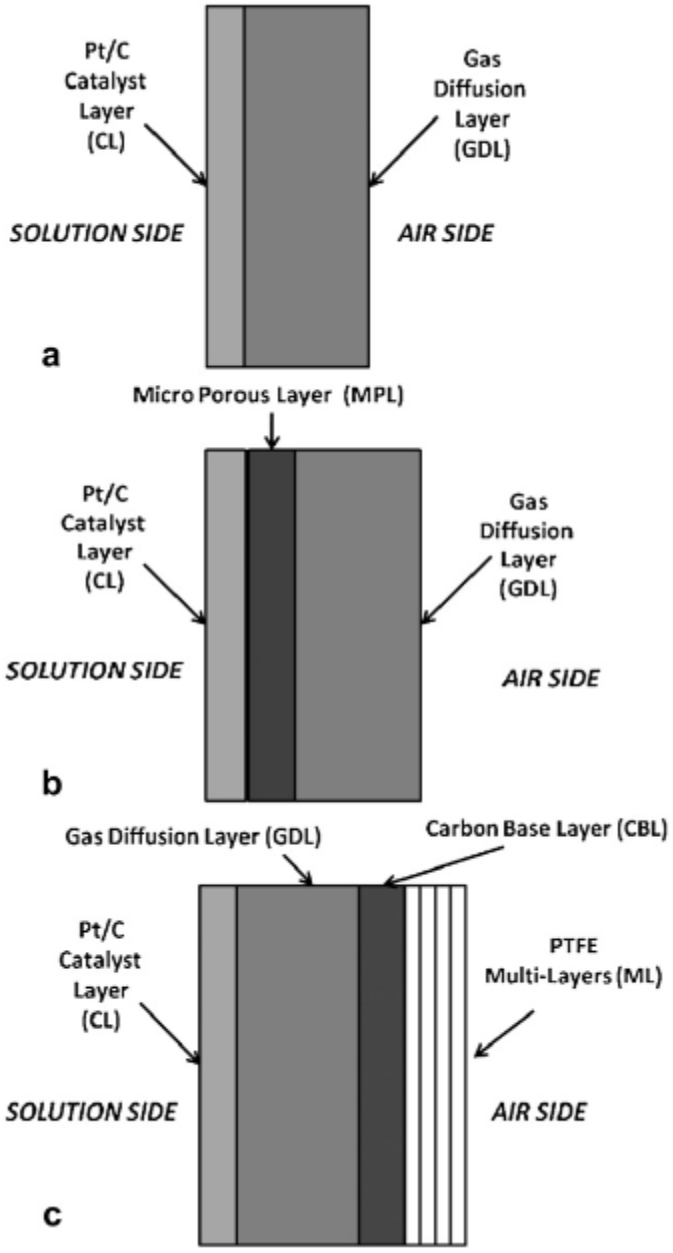

Figure 67 : Diagrams of (a) two-layer, (b) three layer, and (c) multiple-layer cathode configuration (not to scale) [128]

Figure 68 shows the cross section of a typical GDL with microporous layer and the view of the surface of GDL without microporous layer. The view clearly shows the fibrous structure of the GDL.

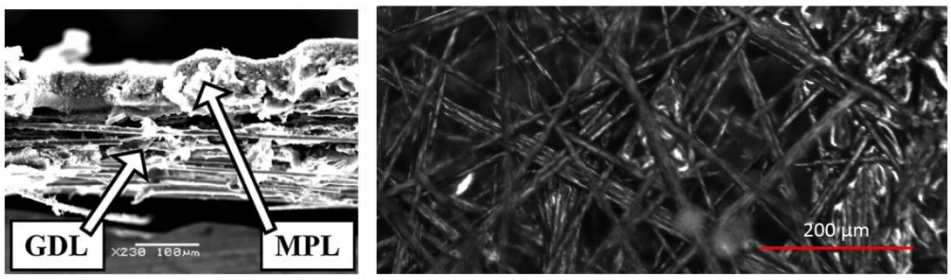

Figure 68 : Left : cross section of gas diffusion layer with microporous layer [42]. Right: surface view of the gas diffusion layer without microporous layer

The GDL considered for this study is Sigracet 10BA without the MPL layer. The next section discusses the setup of the model for the GDL.

7.2 Model Setup

The geometry for the GDL model is very similar to the one for the multi-fiber model discussed in the previous chapter. The main features of the GDL model are the number of fibers, the diameter of the fibers, and the distance between the fibers. Figure 69 shows the model for the GDL: twenty columns with four fibers in each column. Each column represents one layer of carbon fiber and according to the manufacturer there is a total of 20 layers. Therefore, the model in Figure 69 represents the thickness of the GDL. The arbitrary number of fibers in the column is set to four to save on computation time.

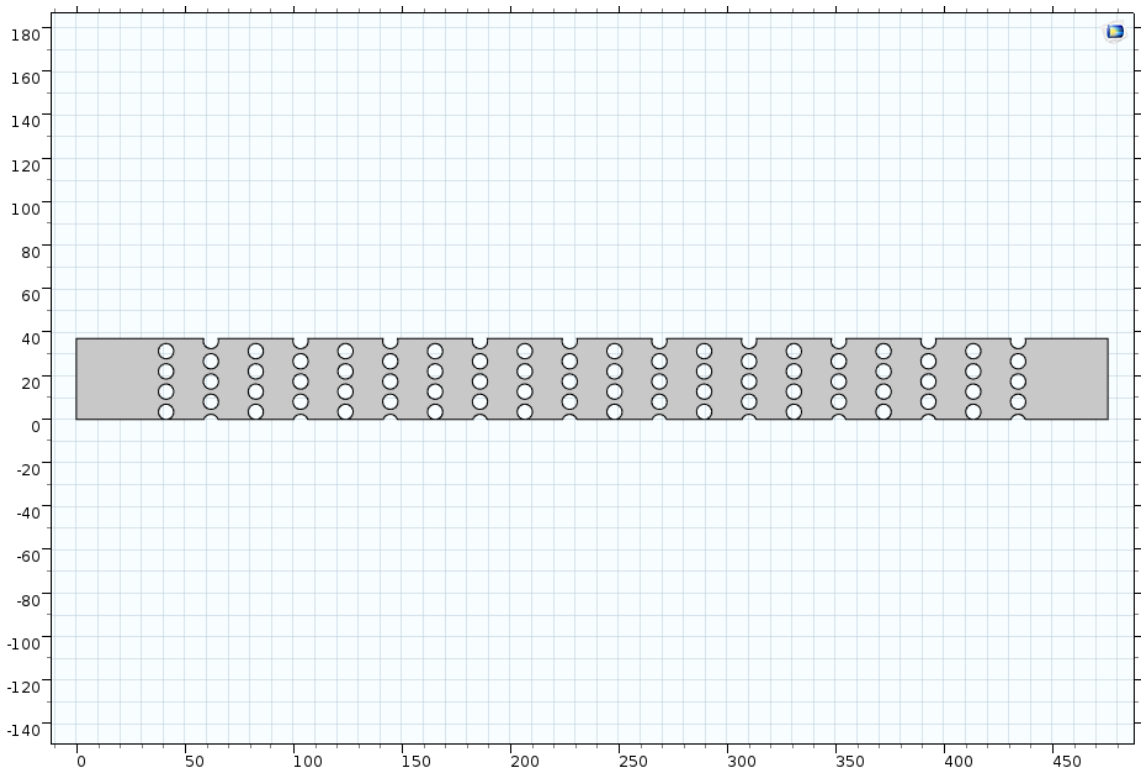

Figure 69 : Geometry of the gas diffusion layer model (axes in µm)

The close-up view of the configuration of the fibers is shown in Figure 70 with the main dimensions labeled. Based on the specification provided by the manufacturer, the fibers are 7 µm in diameter and the GDL has a thickness of 400 µm with a porosity of 0.2, equivalent to solid volume fraction of 0.8. With this information available, the values for l and h are calculated to be 20.68 µm and 9.30 µm respectively using the following Equations:

$$\alpha = 1 - porosity = \frac{\pi d_f^2}{4lh} \tag{58}$$

$$Thickness = 19l + d_f \tag{59}$$

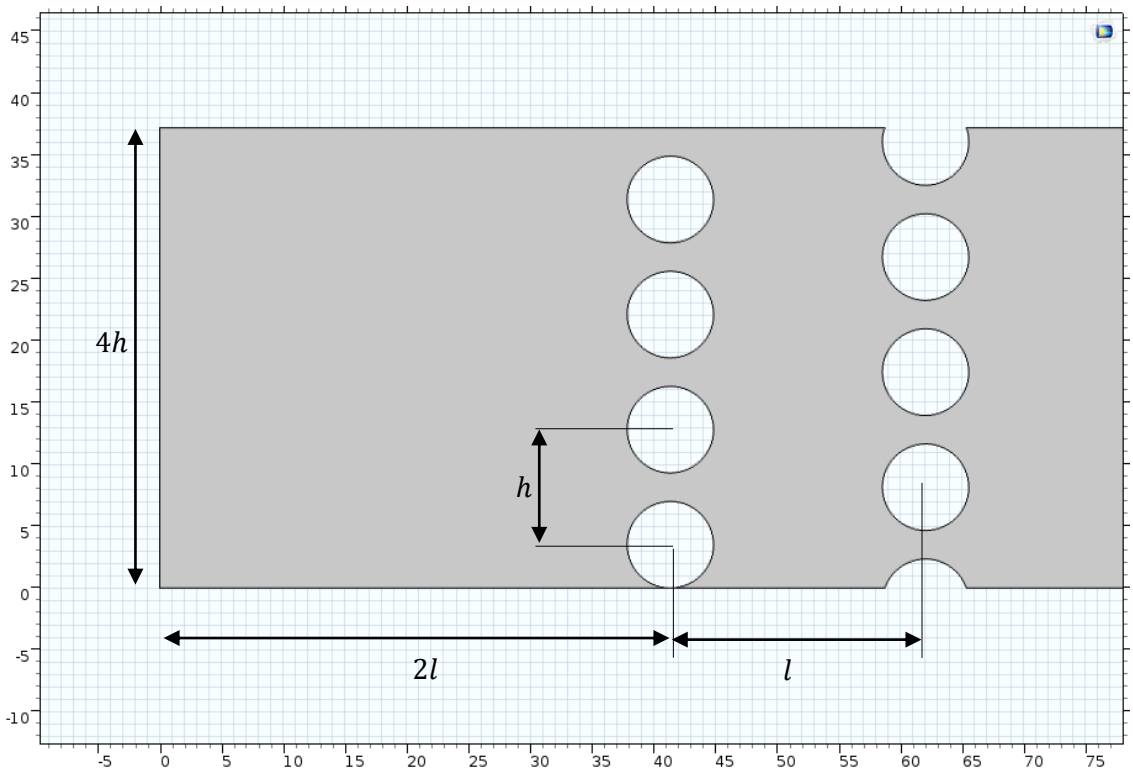

Figure 70 : Close-up view of fiber configuration in gas diffusion layer model

7.3 Governing Equations

The governing equations for the GDL model are identical to the ones used for the single-fiber model with particles , in Section 4.4.

7.4 Boundary Conditions

The boundary conditions for the GDL model are the same as the multi-fiber model shown in Figure 48, the only difference is the addition of more fibers to the model. Similarly, the mesh parameters for the GDL model are the same as mesh 3 for the multi-fiber model.

7.5 Results and Discussion

The overall flow field in the GDL model is qualitatively similar to the multi-fiber model, however, due to the different arrangement of the fibers, the velocity values are different. Figure 71 shows the flow field and streamlines in the entrance of the GDL model.

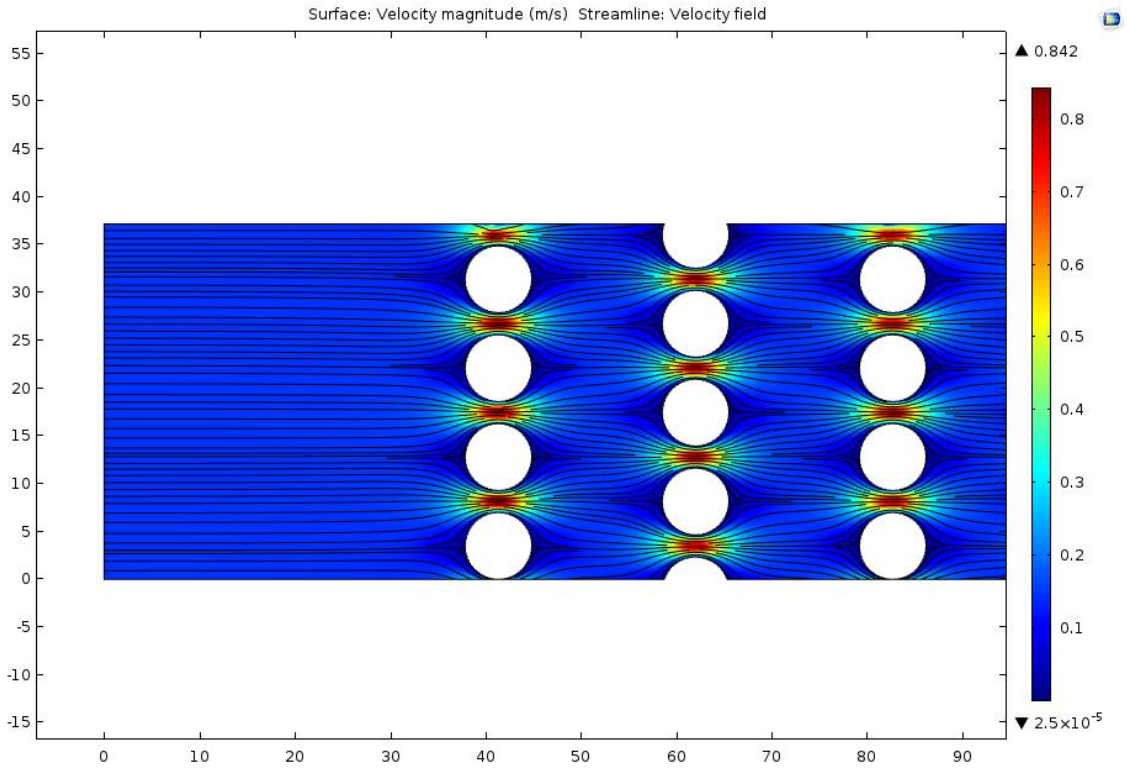

Figure 71 : GDL model flow field

The model is challenged with particles with dry diameter of 0.1 µm and 1.3 µm while relative humidity levels range from 0% to 100%. The humidity model developed from the previous chapter is used for analysis. The effect of relative humidity on particle removal from flow through the GDL is shown in Figure 72 and Figure 73. The overall shape of the curve in Figure 72 is similar to the one from multi-fiber model, shown in Figure 66, emphasizing the similarities between the two models. However, it is noteworthy that the efficiency values for the GDL model are much higher than the multi-fiber values. At 0% relative humidity, the multi-fiber model shows an efficiency of about 2 percent while the GDL model shows an efficiency more than 10 times larger, at 30%. The decreasing trend in particle removal efficiency as humidity level increases, is due to the effect of humidity on the size of the particle as described in the previous chapter.

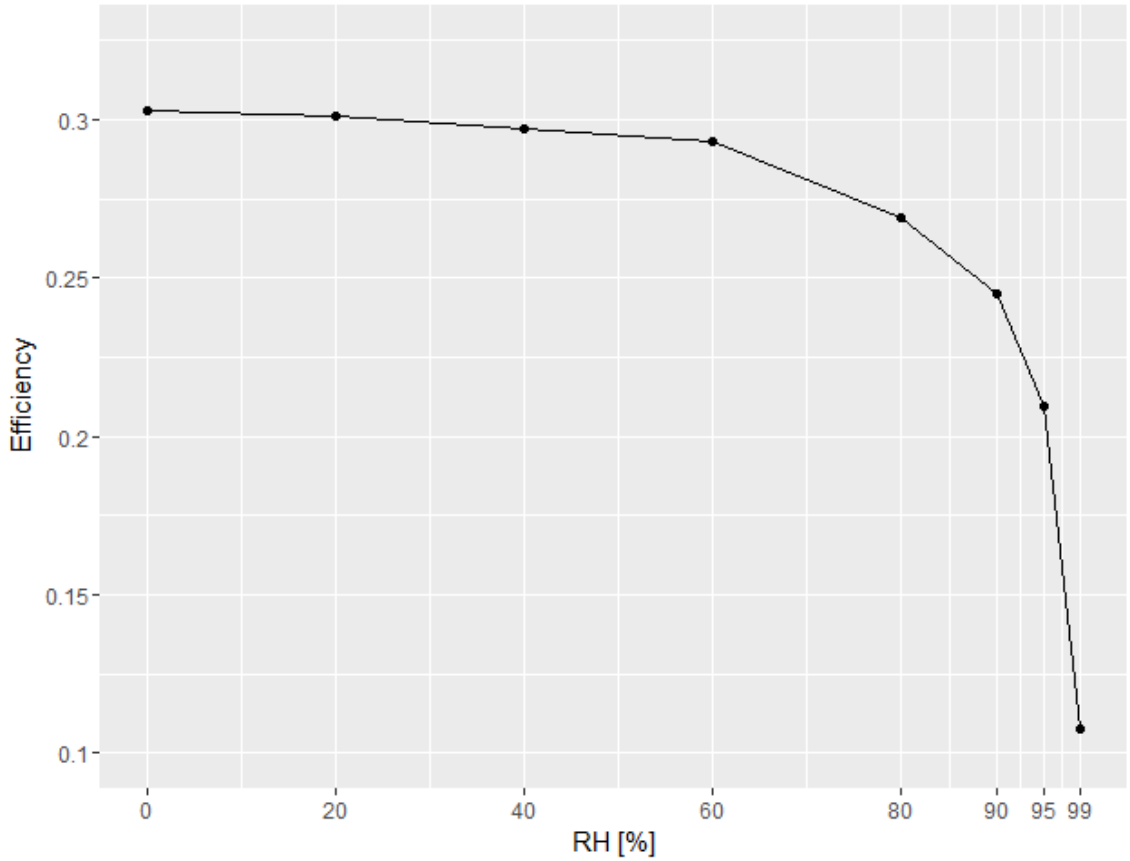

Figure 72 : Effect of humidity on particle capture efficiency of gas diffusion layer, dry particle diameter 0.1 µm

By increasing the dry diameter of the particles to 1.3 µm, the particle capture behavior of the GDL changes as shown in Figure 73. In this figure, as the relative humidity level has increased, the particle capture efficiency has also increased, from about 78% to 97% at relative humidity levels of 0% and 99% respectively. The difference in the behavior stems from the transition of particle capture mechanism from Brownian diffusion to interception and inertial impaction as the particle size has increased due to increased humidity levels. This transition is also shown in Figure 36.

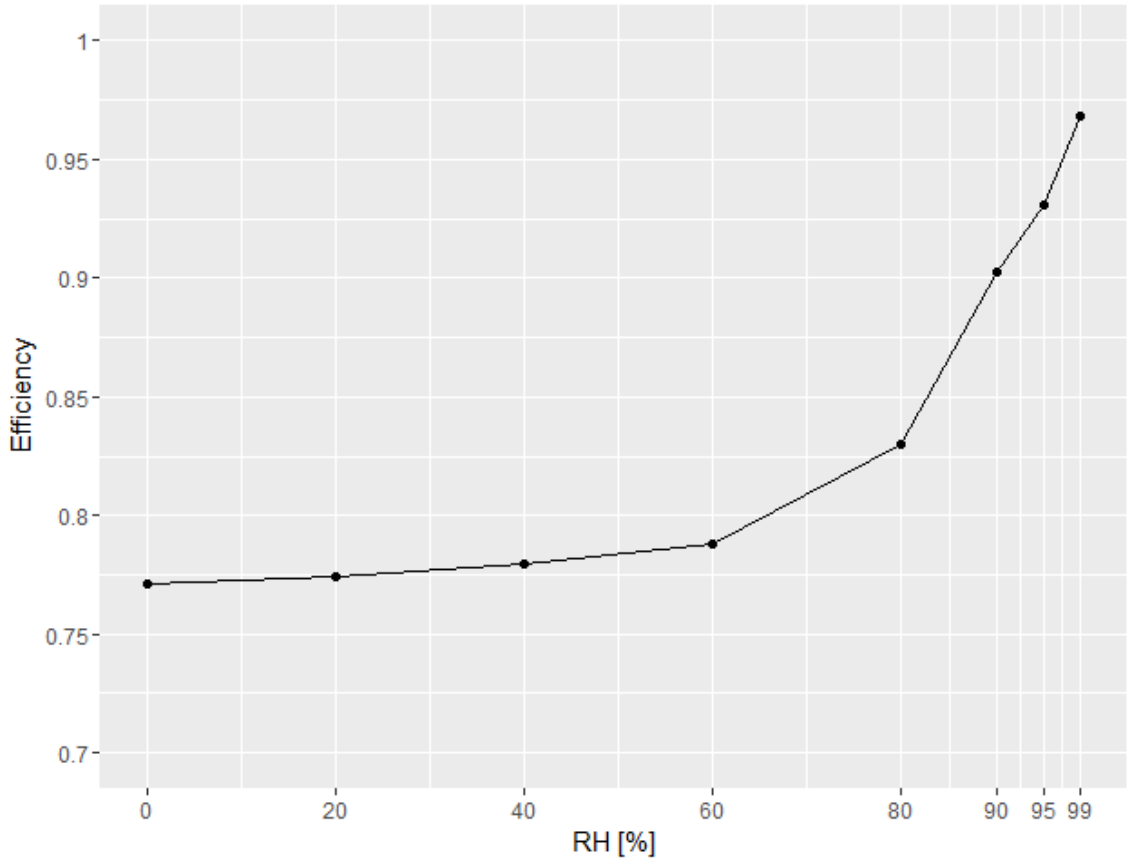

Figure 73 : Effect of humidity on particle capture efficiency of gas diffusion layer, dry particle diameter 1.3 µm

To reiterate, the higher the particle capture efficiency, the more particles will be captured, resulting in lower air flow rate through the GDL to the reaction. The captured particles obstruct the path of the flow reducing the amount of oxygen that is available for reaction with hydrogen. The results of the GDL model, shown in Figure 72 and Figure 73, are extremely important in determining the ideal operating condition for fuel cells in an environment with high level of particulate matter. When the particles are small, by increasing the relative humidity of the cathode air stream, the number of the particles that are captured by the fiber is reduced exponentially. This phenomenon is important in the relative humidity levels between 60% and 99%. The rapid drop in particle capture efficiency above 60% relative humidity testifies to the importance of humidifying the air to as high a level as possible.

It is noteworthy that humidification of the cathode stream is also important for optimal performance of the PEM fuel cell. For instance, the humidity in the cathode stream is essential in keeping the membrane inside the cell from drying. Ideally, to fulfill the humidity requirements for both functions, i.e. membrane requirement and particle capture requirement, the particles must be small enough so that the Brownian capture mechanism dominates, as is the case in Figure 72. Otherwise, if the particles are large enough that the scenario in Figure 73 dominates, with the increased levels of humidity, more particles are captured at the GDL, resulting in poor cell performance. Therefore,

in order to control the size of the particles that enter PEM fuel cell through the cathode stream, a filter must be implemented upstream of the GDL to remove larger particles.

7.5.1 Note on Performance of Cathode Filter

As discussed in Section 3, the structure of the GDL and fibrous filters are very similar : they are both made of stacked layers of fibers and both have fiber diameters in the same range. This means that the GDL model can also be used in understanding the effect of humidity on fibrous filters. The thickness of fibrous filters, is usually much larger than that of the GDL. In a setup where fibrous filter is used upstream of the GDL, the filter would remove the large particles and smaller uncaptured particles would pass through to the GDL. This means that the fibrous filter's main mechanisms of particle capture would be inertial impaction and interception. At the filter, as relative humidity increases, consequently resulting in increase in particle size, more particles will be captured by the filter, similar to the behavior observed in Figure 73. Therefore, the lifetime of a filter used under high relative humidity will be lower compared to an otherwise low humidity scenario.

The GDL model in this section has limitations. The numerical solver used for this model, uses the particle diameter to calculate the forces on the particles correctly however, it does not consider the physical size of the particles. For instance, in a hypothetical scenario where a particle of diameter 10 µm is modeled to pass through a 5µm gap, the solver does not resolve the obvious solution that the particle gets stuck at the gap; instead, it solves for the motion for the particle through the gap. While this limitation is a problem for large particle to fiber size ratio, it does not impose a problem for this study: the size of the particle is about 70 times less than the size of the fiber. However, one must be careful in extending the model in this study to particles sizes beyond 1.3 µm where size of the particle becomes comparable to the fibers.

7.6 Summary

A GDL model was developed based on a commercial GDL consisting of 20 columns of fiber with a porosity of 80% and fiber diameter of 7 µm. The GDL model was exposed to particle sizes 0.1 µm and 1.3 µm as relative humidity increased from 0% to 100%. For particle size 0.1 µm, as relative humidity increases, less particles are captured by the GDL fibers. This is due to the drop in particle capture by Brownian diffusion. However, for particle size 1.3 µm, as relative humidity increases, more particles are captured by the GDL due to the increase in particle capture by interception and inertial impaction. This conflicting pattern is extremely beneficial in protecting the GDL by implementing a fibrous filter upstream of the GDL. The fibrous filter allows for more of the larger particles to be captured at the filter, and fewer of the smaller particles be captured at the GDL as relative humidity increases.

8 Conclusions

This study has been undertaken with the goal of understanding the interaction of particles with the gas diffusion layer (GDL) in proton exchange membrane (PEM) fuel cells. Given the fibrous nature of the GDL a systematic approach is adopted in modeling the porous media: First stage of the study focused on validating the performance of the solver used in the study by running simulations with no-slip and slip boundary conditions. Upon deeming the solver acceptable, the flow field around a single fiber was developed and using slip boundary condition at the surface of the fiber, the flow was validated.

The second stage of the model added particles to the single-fiber model and discussed the possible capture mechanisms. Particle capture due to Brownian diffusion was determined to be the main mechanism of particle capture in the conditions defined in this application, taking precedence over the inertial impaction and interception mechanisms. The particle capture behavior of the single-fiber model was analyzed and it was concluded that the model showed reasonable agreement with the literature making it possible to expand the model to include more fibers.

In the third stage of the model, the single-fiber model was expanded to a multi-fiber model with particles in a staggered configuration. The results of the model from this stage of the study were validated paving the way for constructing a humidity model based on the staggered configuration. The conclusion drawn from this stage of the study is about the relevance of the staggered and parallel configurations for fiber arrangement in modeling porous media. In the particular application considered in this study, it is imperative to consider the worst-case-scenario which occurs when the most number of particles are captured in the GDL. Comparison of the staggered and parallel model reveal that the staggered model shows a higher particle capture efficiency. Therefore, it is concluded that the staggered model is a better model for analyzing design challenges such as the one described in this study.

In the fourth stage of the study, a humidity model was developed based on the effect of relative humidity on the particle as well as the ambient air. The effects were categorized into four independent mechanisms, each tested for significance separately. The effect of the relative humidity on the size of particles was the most significant of all four mechanisms, with the least significant effect associated with the effect of relative humidity on the density of air.

The last stage of the study applied the humidity model to a GDL model and identified the effect on the particle capture efficiency as relative humidity varied. The results of this study has shown that in order to minimize the amount of particle capture in the GDL, it is ideal to use a fibrous filter upstream of the GDL: The filter would be exposed to larger particles, with its particle capture efficiency increasing as relative humidity increases, and the GDL would be exposed to smaller particles, with particle capture efficiency decreasing as the relative humidity increases. The relative humidity level of the air must be maximized to 100% in order to remove most particles at the filter and have the least number of particles depositing on the GDL.

9 Future Work

The particle model developed in this study is a simplified application of particle impaction theory. In this study the particles are assumed rigid, spherical, uniformly distributed properties which is advantageous in preliminary modeling, but inaccurate for advanced analysis. Furthermore, the particles in this study do not have any effect on the flow through the porous media, in other words, the current model is a one-way simulation. It is recommended to use the current model as a foundation for implementing deformable particles with non-uniform properties. Implementation of deformable particles is challenging as the particle itself would need to be modeled separately and the effect of fluid on solid and vice versa cannot be ignored. This would require a coupled configuration between the fluid and solid domains. This approach will also pave the way for studying the effect of particles of different shapes on the gas diffusion layer.

This study has focused on developing an understanding of the interaction of particles and porous media in fuel cells numerically without any experimental observations. It is recommended to replicate the scenarios used in this study experimentally. Such an experiment would require mono-disperse particle generators and particle detection systems. The generated particles would have to be neutralized to remove any effects due to charges on the particles. Particles of different types are recommended to be considered for the experimental set up, including hygroscopic and non-hygroscopic particles. Results from such experiments would provide valuable input into calibration of the numerical models and especially into validation of the relative humidity model developed in this study.

The gas diffusion layer modeled in this study is a raw form without any coatings applied to it. However, many gas diffusion layers available in the market use coatings to improve water management in fuel cells. It is recommended to investigate the effect of coatings into models in the future. The best approach would be using the abovementioned experimental approach for characterizing the effect of particles on coated vs. non-coated samples.

11 References

[1] E. E. Michaelides, Alternative Energy Sources, Springer Berlin Heidelberg, 2012.

[2] M. Martin, Alternative Energy Sources and Technologies, Springer International Publishing, 2016.

[3] ExxonMobile, "Outlook for energy 2013-2040," 2013. [Online]. Available: http://www.clingendaelenergy.com/inc/upload/files/2013_ExxonMobil_Outlook_for_Energy_.pdf.

[4] D. G. Streets and S. T. Waldhoff, "Present and future emissions of air pollutants in China:: SO2, NOx, and CO," *Atmospheric Environment*, pp. 34(3), 363-374, 2000.

[5] X. Li, Principles of Fuel Cells, Taylor and Francis, 2006.

[6] A. Ziliukas, "Application of fuel cells in transportation," *Transport*, pp. 19(5), 219-223., 2004.

[7] J. PERLEZ, "Beijing, Bracing for 5 Days of Heavy Pollution, Issues Red Alert," The New York Times, 16 Dec. 2016. [Online]. Available: https://www.nytimes.com/2016/12/16/world/asia/beijing-air-pollution.html?_r=0. [Accessed 2017].

[8] J. Burke, "India's doctors blame air pollution for sharp rise in respiratory diseases," The Guardian, 23 Wednesday 2015. [Online]. Available: https://www.theguardian.com/world/2015/sep/23/india-doctors-air-pollution-rise-respiratory-diseases-delhi. [Accessed 2017].

[9] J. Burke, "Delhi's air pollution is health timebomb that poses threat to millions of children," The guardian Weekly, 3 Jul 2015. [Online]. Available: http://www.pressreader.com/uk/the-guardian-weekly/20150703/281685433500543/TextView. [Accessed 2017].

[10] U. Nations, "United Nations Framework Convention on Climate Cahnge," United Nations, [Online]. Available: http://unfccc.int/kyoto_protocol/items/2830.php. [Accessed 2017].

[11] "Energy Department Announces $35 Million to Advance Fuel Cell and Hydrogen Technologies," Energy.gov, 3 March 2015. [Online]. Available: https://energy.gov/eere/articles/energy-department-announces-35-million-advance-fuel-cell-and-hydrogen-technologies. [Accessed 2017].

[12] "Canada, China Sign Trade Deal Worth As Much As $2.5 Billion," huffingtonpost.ca, 11 08 2014. [Online]. Available: http://www.huffingtonpost.ca/2014/11/08/canada-china-trade-deal_n_6125180.html. [Accessed 2017].

[13] D. Jollie, "Aspects of fuel cell development and commercialisation," *Applied Earth Science*, pp. 114(3), 154-157., 2005.

[14] N. Sammes, Fuel cell technology: reaching towards commercialization, Springer Science & Business Media, 2006.

[15] S. Srinivasan, Fuel cells: from fundamentals to applications, Springer Science & Business media, 2006.

[16] https://www.scientific-computing.com/feature/fuel-thought-cars-future, "Fuel for thought on cars of the future," 1 January 2003. [Online].

[17] J. Zhang, PEM fuel cell electrocatalysts and catalyst layers: fundamentals and applications, Springer Science & Business Media, 2008.

[18] A. L. Dicks, "Hydrogen generation from natural gas for the fuel cell systems of tomorrow," *Journal of power sources,* pp. 61(1-2), 113-124, 1996.

[19] J. A. Turner, "Sustainable hydrogen production," *Science,* pp. 305(5686), 972-974, 2004.

[20] D. Das and T. N. Veziroğlu, "Hydrogen production by biological processes: a survey of literature," *International Journal of Hydrogen Energy,* pp. 26(1), 13-28, 2001.

[21] X. Cheng, Z. Shi, N. Glass, L. Zhang, J. Zhang, D. Song and J. Shen, "A review of PEM hydrogen fuel cell contamination: Impacts, mechanisms, and mitigation," *Journal of Power Sources,* pp. 165(2), 739-756, 2007.

[22] S. H. Oh and R. M. Sinkevitch, "Carbon monoxide removal from hydrogen-rich fuel cell feedstreams by selective catalytic oxidation," *Journal of Catalysis,* pp. 142(1), 254-262, 1993.

[23] S. Takenaka, T. Shimizu and K. Otsuka, "Complete removal of carbon monoxide in hydrogen-rich gas stream through methanation over supported metal catalysts," *International Journal of Hydrogen Energy,* pp. 29(10), 1065-1073, 2004.

[24] H. F. Oetjen, V. M. Schmidt, U. Stimming and F. Trila, "Performance data of a proton exchange membrane fuel cell using H 2/CO as fuel gas," *Journal of the Electrochemical Society,* pp. 143(12), 3838-3842, 1996.

[25] T. Okada, N. Nakamura, M. Yuasa and I. Sekine, "Ion and water transport characteristics in membranes for polymer electrolyte fuel cells containing H+ and Ca2+ cations," *Journal of the Electrochemical Society,* pp. 144(8), 2744-2750, 1997.

[26] J. M. Moore, P. L. Adcock, J. B. Lakeman and G. O. Mepsted, "The effects of battlefield contaminants on PEMFC performance," *Journal of Power Sources,* pp. 85(2), 254-260, 2000.

[27] R. Mohtadi, W. K. Lee, S. Cowan, J. W. Van Zee and M. Murthy, "Effects of hydrogen sulfide on the performance of a PEMFC," *Electrochemical and Solid-State Letters,* pp. 6(12), A272-A274, 2003.

[28] F. A. Uribe, S. Gottesfeld and T. A. Zawodzinski, "Effect of ammonia as potential fuel impurity on proton exchange membrane fuel cell performance," *Journal of the Electrochemical Society*, pp. 149(3), A293-A296, 2002.

[29] A. Q. Contractor and H. Lal, "Two forms of chemisorbed sulfur on platinum and related studies," *Journal of Electroanalytical Chemistry and Interfacial Electrochemistry*, pp. 96(2), 175-181, 1979.

[30] R. Mohtadi, W. K. Lee and J. W. Van Zee, "Assessing durability of cathodes exposed to common air impurities," *Journal of Power Sources*, pp. 138(1), 216-225, 2004.

[31] D. Yang, J. Ma, L. Xu, M. Wu and H. Wang, "The effect of nitrogen oxides in air on the performance of proton exchange membrane fuel cell," *Electrochimica Acta*, pp. 51(19), 4039-4044, 2006.

[32] M. Angelo and J. St-Pierre, "The Effect of Common Airborne Impurities and Mixtures on PEMFC Performance and Durability," *ECS Transactions*, pp. 64(3), 773-788, 2014.

[33] A. R. Khan, J. Zhao and O. Y. Polevaya, "Study of ammonia formation during the autothermal reforming of hydrocarbon based fuels," *MRS Proceedings*, pp. Vol. 756, pp. FF8-7, 2002.

[34] X. Z. Yuan, H. Li, Y. Yu, M. Jiang, W. Qian, S. Zhang and T. T. Cheng, "Diagnosis of contamination introduced by ammonia at the cathode in a polymer electrolyte membrane fuel cell," *international journal of hydrogen energy*, pp. 37(17), 12464-12473, 2012.

[35] J. St-Pierre, Y. Zhai and M. Angelo, "Quantitative ranking criteria for PEMFC contaminants," *international journal of hydrogen energy*, pp. 37(8), 6784-6789, 2012.

[36] J. St-Pierre, Y. Zhai and M. S. Angelo, "Effect of selected airborne contaminants on PEMFC performance," *Journal of The Electrochemical Society*, pp. 161(3), F280-F290, 2014.

[37] P. Faber, F. Drewnick, J. Piske, T. Kurz and S. Borrmann, "ffects of atmospheric aerosol on the performance of environmentally sustainable passive air-breathing PEM fuel cells," *international journal of hydrogen energy*, pp. 37(22), 17203-17208, 2012.

[38] "Central Pollution Control Board (Government of India)," [Online]. Available: http://www.cpcb.gov.in/CAAQM/mapPage/frmdelhi.aspx?stateID=6.

[39] "Environment and Climate Change Canada," [Online]. Available: http://ec.gc.ca/inrp-npri/donnees-data/ap/index.cfm?lang=En.

[40] "United States Environmental Protection Agency," 2012. [Online]. Available: https://www3.epa.gov/ttn/naaqs/standards/so2/s_so2_history.html.

[41] "United States Environmental Protection Agency," 2012. [Online]. Available: https://www.epa.gov/criteria-air-pollutants/naaqs-table.

[42] C. Chan, N. Zamel, X. Li and J. Shen, "Experimental measurement of effective diffusion coefficient of gas diffusion layer/microporous layer in PEM fuel cells," *Electrochimica Acta,* pp. 65, 13-21, 2012.

[43] S. Kuwabara, "The forces experienced by randomly distributed parallel circular cylinders or spheres in a viscous flow at small reynolds numbers," *Journal of the Physical Society of Japan, 14(4),* pp. 527-532, 1959.

[44] R. C. Brown, Air filtration: an integrated approach to the theory and applications of fibrous filters, Pergamon, 1993.

[45] A. Karadimos and R. Ocone, "The effect of the flow field recalculation on fibrous filter loading: a numerical simulation," *Powder technology,* pp. 137(3), 109-119, 2003.

[46] S. J. Dunnett and C. F. Clement, "A numerical study of the effects of loading from diffusive deposition on the efficiency of fibrous filters," *Journal of aerosol science,* pp. 37(9), 1116-1139, 2006.

[47] C. Kanaoka, S. Hiragi and W. Tanthapanichakoon, "Stochastic simulation of the agglomerative deposition process of aerosol particles on an electret fiber," *Powder Technology,* pp. 118(1), 97-106, 2001.

[48] W. Tanthapanichakoon, K. Maneeintr, T. Charinpanitkul and C. Kanaoka, "Estimation of collection efficiency enhancement factor for an electret fiber with dust load," *Journal of aerosol science,* pp. 34(11), 1505-1522, 2003.

[49] R. Przekop, K. Grzybowski and L. Gradoń, "Energy-balanced oscillatory model for description of particles deposition and re-entrainment on fiber collector," *Aerosol science and technology,* pp. 38(4), 330-337, 2004.

[50] Z. Hui, F. Haiming and K. Yanming, "Simulation of deposition of aerosol particles on a single fiber surface," *Environmental Pollution & Control,* pp. 3, 002, 2009.

[51] S. A. Hosseini and H. V. Tafreshi, "Modeling particle filtration in disordered 2-D domains: A comparison with cell models," *Separation and Purification Technology,* pp. 74(2), 160-169, 2010.

[52] M. Faessel, C. Delisée, F. Bos and P. Castéra, "3D Modelling of random cellulosic fibrous networks based on X-ray tomography and image analysis," *Composites science and technology,* pp. 65(13), 1931-1940, 2005.

[53] M. J. Lehmann, E. H. Hardy, J. Meyer and G. Kasper, "MRI as a key tool for understanding and modeling the filtration kinetics of fibrous media," *Magnetic resonance imaging,* pp. 23(2), 341-342, 2005.

[54] J. Hoferer, E. H. Hardy, J. Meyer and G. Kasper, "Measuring particle deposition within fibrous filter media by magnetic resonance imaging," *FILTRATION-COALVILLE-,* pp. 7(2), 154, 2007.

[55] Q. Wang, B. Maze, H. V. Tafreshi and B. Pourdeyhimi, "A case study of simulating submicron aerosol filtration via lightweight spun-bonded filter media," *Chemical Engineering Science,* pp. 61(15), 4871-4883, 2006.

[56] S. A. Hosseini and H. V. Tafreshi, "3-D simulation of particle filtration in electrospun nanofibrous filters," *Powder Technology,* pp. 201(2), 153-160, 2010b.

[57] B. Xu, Y. Wu, Z. Lin and Z. Chen, "Investigation of air humidity affecting filtration efficiency and pressure drop of vehicle cabin air filters.," *Aerosol and Air Quality Research,* pp. 14(3), 1066-1073., 2014.

[58] A. F. Miguel, "Effect of air humidity on the evolution of permeability and performance of a fibrous filter during loading with hygroscopic and non-hygroscopic particles," *Journal of Aerosol Science,* pp. 34(6), 783-799, 2003.

[59] A. Joubert, J. C. Laborde, L. Bouilloux, S. Calle-Chazelet and D. Thomas, "Influence of humidity on clogging of flat and pleated HEPA filters," *Aerosol Science and Technology,* pp. 44(12), 1065-1076, 2010.

[60] B. J. Mullins, I. E. Agranovski and R. D. Braddock, "particle bounce during filtration of particles on wet and dry filters," *Aerosol Science & Technology,* pp. 37(7), 587-600, 2003.

[61] S. C. Chen, C. J. Tsai, H. D. Chen, C. Y. Huang and G. D. Roam, "The influence of relative humidity on nanoparticle concentration and particle mass distribution measurements by the MOUDI," *Aerosol Science and Technology,* pp. 45(5), 596-603, 2011.

[62] P. Winkler, "Relative humidity and the adhesion of atmospheric particles to the plates of impactors," *Journal of Aerosol Science,* pp. 5(3), 235-240, 1974.

[63] S. W. Stein, B. J. Turpin, X. Cai, P. F. Huang and P. H. Mcmurry, "Measurements of relative humidity-dependent bounce and density for atmospheric particles using the DMA-impactor technique," *Atmospheric Environment,* pp. 28(10), 1739-1746, 1994.

[64] X. Q. Zhang, P. H. McMurray, S. V. Hering and G. S. Casuccio, "Mixing characteristics and water content of submicron aerosols measured in Los Angeles and at the Grand Canyon," *Atmospheric Environment,* pp. 27(10), 1593-1607, 1993.

[65] J. Happel, "Viscous flow relative to arrays of cylinders," *AIChE,* pp. 5(2), 174-177, 1959.

[66] A. A. Kirsch and N. A. Fuchs, "Studies on fibrous aerosol filters—II. Pressure drops in systems of parallel cylinders," *Annals of Occupational Hygiene,* pp. 10(1), 23-30, 1967.

[67] H. Hasimoto, "On the periodic fundamental solutions of the Stokes equations and their application to viscous flow past a cubic array of spheres," *Journal of Fluid Mechanics,* pp. 5(02), 317-328, 1959.

[68] K. Tamada and H. Fujikawa, "The steady two-dimensional flow of viscous fluid at low Reynolds numbers passing through an infinite row of equal parallel circular cylinders," *The Quarterly Journal of Mechanics and Applied Mathematics,* pp. 10(4), 425-432, 1957.

[69] A. A. Kirsch and N. A. Fuchs, "The fluid flow in a system of parallel cylinders perpendicular to the flow direction at small Reynolds numbers," *Journal of the Physical Society of Japan,* pp. 22(5), 1251-1255, 1967b.

[70] H. C. Yeh and B. Y. Liu, "Aerosol filtration by fibrous filters—I Theoretical," *Journal of aerosol science,* pp. 5(2), 191-204, 1974.

[71] A. Dipankar and T. K. Sengupta, "Flow past a circular cylinder in the vicinity of a plane wall," *Journal of Fluids and Structures,* pp. 20(3), 403-423, 2005.

[72] S. J. Price, D. Sumner, J. G. Smith, K. Leong and M. P. Paidoussis, "Flow visualization around a circular cylinder near to a plane wall," *Journal of Fluids and Structures,* pp. 16(2), 175-191, 2002.

[73] D. Sumner, J. L. Heseltine and O. J. P. Dansereau, "Wake structure of a finite circular cylinder of small aspect ratio," *Experiments in Fluids,* pp. 37(5), 720-730, 2004.

[74] A. Travin, M. Shur, M. Strelets and P. Spalart, "Detached-eddy simulations past a circular cylinder," *Flow, Turbulence and Combustion,* pp. 63(1-4), 293-313, 2000.

[75] B. N. Rajani, A. Kandasamy and S. Majumdar, "Numerical simulation of laminar flow past a circular cylinder," *Applied Mathematical Modelling,* pp. 33(3), 1228-1247, 2009.

[76] P. Catalano, M. Wang, G. Iaccarino and P. Moin, "Numerical simulation of the flow around a circular cylinder at high Reynolds numbers," *International Journal of Heat and Fluid Flow,* pp. 24(4), 463-469, 2003.

[77] S. Childress, An introduction to theoretical fluid mechanics (Vol. 19), American Mathematical Soc., 2009.

[78] F. M. White, Viscous Fluid Flow, McGraw-Hill, 1991.

[79] F. Nieuwstadt and H. B. Keller, "Viscous flow past circular cylinders," *Computers & Fluids,* pp. 1(1), 59-71, 1973.

[80] M. Coutanceau and R. Bouard, "Experimental determination of the main features of the viscous flow in the wake of a circular cylinder in uniform translation. Part 1. Steady flow," *Journal of Fluid Mechanics,* pp. 79(02), 231-256, 1977.

[81] O. Sahni, K. E. Jansen, M. S. Shephard, C. A. Taylor and M. W. Beall, "Adaptive boundary layer meshing for viscous flow simulations," *Engineering with Computers,* pp. 24(3), 267, 2008.

[82] F. M. White, Fluid Mechanics, New York: McGrawHill, 2011.

[83] *COMSOL Documentation,* COMSOL Multyphiscs, 2015.

[84] K. O. L. F. Jayaweera and B. J. Mason, "The behaviour of freely falling cylinders and cones in a viscous fluid," *Journal of Fluid Mechanics,* p. 1965, 22(04), 709-720.

[85] D. Tritton, "Experiments on the flow past a circular cylinder at low Reynolds numbers," *Journal of Fluid Mechanics,* pp. 6(04), 547-567, 1959.

[86] M. Nishioka and S. Hiroshi, "Measurements of velocity distributions in the wake of a circular cylinder at low Reynolds numbers," *Journal of Fluid Mechanics,* pp. 65.01 (1974): 97-112., 1974.

[87] H. Wang, H. Zhao, K. H. Y. Wang and C. Zheng, "Simulation of filtration process for multi-fiber filter using the Lattice-Boltzmann two-phase flow model," *Journal of Aerosol Science,* pp. 66, 164-178, 2013.

[88] Z. G. Liu and P. K. Wang, "Pressure drop and interception efficiency of multifiber filters," *Aerosol science and technology,* pp. 26(4), 313-325, 1997.

[89] J. H. S. Richard C. Flagan, Fundamentals of Air Pollution Engineering, Dover Publications Inc, 2012.

[90] M. Gad-el-Hak, "The fluid mechanics of microdevices—the Freeman scholar lecture," *Journal of Fluids Engineering,* pp. 121(1), 5-33, 1999.

[91] H. C. Yeh and B. Y. Liu, "Aerosol filtration by fibrous filters—II. Experimental," *Journal of Aerosol Science,* pp. 5(2), 205-217, 1974.

[92] T. Myojo, C. Kanaoka and H. Emi, "Experimental observation of collection efficiency of a dust-loaded fiber," *Journal of aerosol science,* pp. 15(4), 483-489, 1984.

[93] D. Thomas, P. Penicot, P. Contal, D. Leclerc and J. Vendel, "Clogging of fibrous filters by solid aerosol particles experimental and modelling study," *Chemical Engineering Science,* pp. 56(11), 3549-3561, 2001.

[94] C. B. Song, H. S. Park and K. W. Lee, "Experimental study of filter clogging with monodisperse PSL particles," *Powder technology,* pp. 163(3), 152-159., 2006.

[95] G. Kasper, S. Schollmeier and J. Meyer, "Structure and density of deposits formed on filter fibers by inertial particle deposition and bounce," *Journal of Aerosol Science,* pp. 41(12), 1167-1182, 2010.

[96] J. C. Maxwell, "On stresses in rarified gases arising from inequalities of temperature," *Philosophical Transactions of the royal society of London,* pp. 170, 231-256, 1879.

[97] *COMSOL Documentation,* COMSOL, 2015.

[98] R. W. Barber and D. R. Emerson, "The influence of Knudsen number on the hydrodynamic development length within parallel plate micro-channels," *WIT Transactions on Engineering Sciences,* p. 36, 2002.

[99] P. Zhao, P. Cheng and B. J. Tatarchuk, "Loading of fibrous filter media and newly designed filter configurations by salt particles: An experimental study," *AIChE Journal,* pp. 62(10), 3739-3750, 2016.

[100] A. C. Martins, X. Huang, A. Goswami, K. Koh, Y. Meng, V. C. Almeida and T. Asefa, "Fibrous porous carbon electrocatalysts for hydrazine oxidation by using cellulose filter paper as precursor and self-template," *Carbon,* pp. 102, 97-105, 2016.

[101] A. Jackiewicz, S. Jakubiak and L. Gradoń, "Analysis of the behavior of deposits in fibrous filters during non-steady state filtration using X-ray computed tomography," *Separation and Purification Technology,* pp. 156, 12-21, 2015.

[102] W. C. Hinds, Aerosol Technology: Properties, Behavior, and Measurement of Airborne Particles, John Wiley & Sons, 2012.

[103] W. C. Hinds, properties, behavior, and measurement of airborne particles, New York: Wiley-Interscience, 1982, pp. 442 p., 1.

[104] D. A. Japuntich, J. I. T. Stenhouse and B. Y. H. Liu, "Experimental results of solid monodisperse particle clogging of fibrous filters," *ournal of aerosol science,* pp. 25(2), 385-393, 1994.

[105] H. Bockhorn, Soot formation in combustion: mechanisms and models (Vol. 59), Springer Science & Business Media, 2013.

[106] J. G. Slowik, K. Stainken, P. Davidovits, L. R. Williams, J. T. Jayne, C. E. Kolb and J. L. Jimenez, "Particle morphology and density characterization by combined mobility and aerodynamic diameter measurements. Part 2: Application to combustion-generated soot aerosols as a function of fuel equivalence ratio," *Aerosol Science and Technology,* pp. 38(12), 1206-1222, 2004.

[107] R. K. Chakrabarty, H. Moosmüller, M. A. Garro, W. P. Arnott, J. Walker, R. A. Susott and W. M. Hao, "Emissions from the laboratory combustion of wildland fuels: Particle morphology and size," *Journal of Geophysical Research: Atmospheres,* p. 111(D7), 2006.

[108] K. Adachi, S. H. Chung and P. R. Buseck, "Shapes of soot aerosol particles and implications for their effects on climate," *Journal of Geophysical Research: Atmospheres,* p. 115(D15), 2010.

[109] H. Ishimoto, Y. Zaizen, A. Uchiyama, K. Masuda and Y. Mano, "Shape modeling of mineral dust particles for light-scattering calculations using the spatial Poisson–Voronoi tessellation," *Journal of Quantitative Spectroscopy and Radiative Transfer,* pp. 111(16), 2434-2443, 2010.

[110] S. A. Hosseini, "Modeling Particle Filtration adn Caking in Fibrous Filter Media," Virginia Commonwealth University, 2011.

[111] Z. Tan, Air pollution and greenhouse gases : from basic concepts to engineering applications for air emission control, Springer, 2014.

[112] M. D. Allen and O. G. Raabe, "Slip correction measurements of spherical solid aerosol particles in an improved Millikan apparatus," *Aerosol Scientific Technology,* p. 4(3):269–286, 1985.

[113] R. E. Reisman, P. M. Mauriello, G. B. Davis, J. W. Georgitis and J. M. DeMasi, "A double-blind study of the effectiveness of a high-efficiency particulate air (HEPA) filter in the treatment of patients with perennial allergic rhinitis and asthma," *Journal of Allergy and Clinical Immunology,* pp. 85(6), 1050-1057, 1990.

[114] J. L. Sublett, J. Seltzer, R. Burkhead, P. B. Williams, H. J. Wedner, W. Phipatanakul and A. &. I. I. A. Committee, "Air filters and air cleaners: rostrum by the American Academy of Allergy, Asthma & Immunology Indoor Allergen Committee," *Journal of Allergy and Clinical Immunology,* pp. 125(1), 32-38, 2010.

[115] L. H. A. Stein, Gas Cyclones and Swirl Tubes: Principles, Design, and Operation, Berlin, Heidelberg, New York, 2010.

[116] J. Chung and G. M. Hulbert, "A time integration algorithm for structural dynamics with improved numerical dissipation: the generalized-α method," *Journal of applied mechanics,* pp. 60(2), 371-375, 1993.

[117] K. E. Jansen, C. H. Whiting and G. M. Hulbert, "A generalized-α method for integrating the filtered Navier–Stokes equations with a stabilized finite element method," *Computer Methods in Applied Mechanics and Engineering,* pp. 190(3), 305-319, 2000.

[118] K. W. Lee and B. Y. H. Liu, "Experimental study of aerosol filtration by fibrous filters," *Aerosol Science and Technology,* pp. 1(1), 35-46, 1981.

[119] TSI, "Condensation Particle Counter Model 3775," December 2016. [Online]. Available: http://tsi.com/uploadedFiles/_Site_Root/Products/Literature/Spec_Sheets/3775_2980343.pdf.

[120] F. C. McQuiston, J. D. Parker and J. D. Spitler, Heating, Ventilating and Air Conditioning: Analysis and Design, 6th Edition, Wiley, 2004.

[121] ASHRAE, *Psychrometric Chart No.1 (SI)*, American Society of Heating, Refrigerating and Air-Conditioning Engineers, 1981.

[122] J. Visser, Surface and Colloid Science, New York: John Wiley and Sons, 1976.

[123] R. C. Flagan and J. H. Seinfeld, Fundamentals of air pollution engineering, Courier Corporation, 2013.

[124] A. P. Bateman, H. Belassein and S. T. Martin, "Impactor apparatus for the study of particle rebound: Relative humidity and capillary forces," *Aerosol Science and Technology*, pp. 48(1), 42-52, 2014.

[125] M. Chang, S. Kim and C. Sioutas, "Experimental studies on particle impaction and bounce: effects of substrate design and material," *Atmospheric Environment*, pp. 33(15), 2313-2322, 1999.

[126] B. Thoben and A. Siebke, "Influence of different gas diffusion layers on the water management of the PEFC cathode," *Journal of New Materials for Electrochemical Systems*, pp. 7(1), 13-20, 2004.

[127] M. Mathias, J. Roth, J. Fleming, W. Lehnert, W. Vielstich, A. Lamm and H. A. Gasteiger, Handbook of fuel cells, W. Vielstich, HA Gasteiger, A. Lamm (Eds.), 3., 2003.

[128] C. Santoro, A. Agrios, U. Pasaogullari and B. Li, "Effects of gas diffusion layer (GDL) and micro porous layer (MPL) on cathode performance in microbial fuel cells (MFCs)," *International journal of hydrogen energy*, pp. 36(20), 13096-13104, 2011.

[129] A. Z. Weber and J. Newman, "Effects of microporous layers in polymer electrolyte fuel cells," *Journal of the Electrochemical Society*, pp. 152(4), A677-A688, 2005.